Non-Uniform Rational B-Splines and Rational Bézier Triangles for Isogeometric Analysis of Structural Applications

by

Ning Liu

A dissertation submitted in partial fulfillment
of the requirements for the degree of
Doctor of Philosophy
(Civil Engineering)
in the University of Michigan
2018

Doctoral Committee:

Associate Professor Ann E. Jeffers, Chair
Professor Sherif El-Tawil
Professor Krishnakumar R. Garikipati
Associate Professor Dale G. Karr

Ning Liu

ningliu@umich.edu

ORCID iD: 0000-0001-8380-0668

Dedication

This dissertation is dedicated to my parents and my wife. I would not have been able to complete this work without their love, support and inspiration for the past four years.

Acknowledgements

I would like to express my sincere gratitude to my advisor, Dr. Jeffers, for her continuous support of my Ph.D. work as well as my M.S. independent study, for her patience, motivation and immense knowledge. Her guidance helped me in all the time of research and writing of this thesis. I could not have imagined having a better advisor and mentor for my Ph.D. study. Besides my advisor, I would like to thank the rest of my dissertation committee: Dr. El-Tawil, Dr. Garikipati and Dr. Karr, not only for their insightful comments and encouragement, but also for the questions that incent me to broaden my research from various perspectives. My sincere thanks also goes to all my friends at Michigan, my GGB 1267A lab colleagues, and the members of the Jeffers' team (Qianru, Ha, Paul, Jason, and Alyssa). I want to specially thank one of my best friends and the gym crew lead, Bo, due to whom I was able to gain 40 lbs through workout and hotpot parties. A good family support system is crucial in surviving and staying sane in grad school. Although I was segregated from my family in China by the big Pacific pond, I was lucky enough to meet my non-DNA-related brothers here, Paul and Jason. We helped each other through the tough times and shared the best memories. I know for a fact that they will still be there as supportive and caring friends when we are old. Last but not least, I want to thank my parents and my wife, for their lifelong support and encouragement. They give me the courage that I need to get over the difficulties and complete this study. I would not have been able to finish my Ph.D. without my professors, friends and family. I extremely appreciate all their support.

Table of Contents

List of Tables

List of Figures

Abstract

Isogeometric Analysis (IGA) is a major advancement in computational analysis that bridges the gap between a computer-aided design (CAD) model, which is typically constructed using Non-Uniform Rational B-splines (NURBS), and a computational model (e.g., finite element model) that traditionally uses Lagrange polynomials to represent the geometry and solution variables. In IGA, the same shape functions that are used in CAD are employed in the computational model. The direct manipulation of CAD data eliminates approximation errors that emanate from the process of converting the geometry from CAD to Finite Element Analysis (FEA). As a result, IGA allows the exact geometry to be represented at the coarsest level and maintained throughout the entire analysis process. While IGA was initially introduced to streamline the design and analysis process, this dissertation shows that IGA can also provide improved computational results for complex and highly nonlinear problems in structural mechanics.

This dissertation addresses various problems in structural mechanics in the context of IGA, with the use of NURBS and rational Bézier triangles for the description of the parametric and physical spaces. The approaches considered here show that a number of important properties (e.g., higher-order smoothness than standard C^0 discretizations, geometric exactness (i.e., CAD model), reduced number of degrees of freedom, improved accuracy and efficiency, and increased flexibility in discretization) can be achieved, leading to improved numerical solutions.

Specifically, using B-splines and a layer-based discretization, a distributed plasticity isogeometric frame model is formulated to capture the spread of plasticity in frames undergoing large deformations. The modeling approach includes an adaptive analysis where the structure of

interest is initially modeled with coarse mesh and knots are inserted based on the yielding information collected at the quadrature points. It is demonstrated that improvement on efficiency and convergence rates is attained.

With tensor-product NURBS, an isogeometric rotation-free multi-layered plate formulation is developed based on a layerwise deformation theory. The derivation assumes a separate displacement field expansion within each layer, and considers transverse displacement component as C^0-continuous at dissimilar material interfaces, which is enforced via knot repetition. The separate integration of the in-plane direction and through-thickness direction allows us to capture the complete 3D stress states in a 2D setting. The proposed method is used to numerically simulate the behavior of advanced materials such as laminated composites and functionally graded materials, and the results show advantages in efficiency and accuracy.

To increase the flexibility in the discretization of geometrically complex domains, rational Bézier triangles for domain triangulation is studied. They are further coupled with a Delaunay-based feature-preserving discretization algorithm for the static bending and free vibration analysis of Kirchhoff plates. Lagrange multipliers are employed to explicitly impose high-order continuity constraints and the augmented system is solved iteratively without increasing the size of the matrices. The resulting discretization is geometrically exact, admits small geometric features, and constitutes C^1-continuity.

The feature-preserving rational Bézier triangles are further applied to smeared damage modeling of quasi-brittle materials. Due to the ability of Lagrange multipliers to raise global continuity to any desired order, the implicit fourth- (C^1-continuous) and sixth-order (C^2-continuous) gradient damage models are analyzed. The inclusion of higher-order terms in the Taylor expansion of the nonlocal formulation improves solution accuracy. A local refinement algorithm that resolves

marked regions with high resolution while keeping the resulting mesh conforming and well-conditioned is also utilized to improve efficiency. The outcome is a unified modeling framework where the feature-preserving discretization is able to capture the initiation and early-stage propagation of damage, and the local refinement technique can then be applied to adaptively refine the mesh in the direction of damage propagation.

Chapter 1 Introduction

Nonlinear analysis of structural components is crucial in civil and mechanical engineering in determining the load-displacement response of structures under extreme loads. A large amount of research has been conducted over the last few decades to develop structural elements (e.g., beams, frames, and plates) that are capable of handling both material and geometric nonlinearities. In order to accurately capture the deformation path of structures under extreme loads, normally a very large number of elements is required for discretization. The resulting number of degrees of freedom (DOFs) is even larger in the context of standard continuum elements, where the discretization is constrained to C^0 continuity and thus rotational DOFs are often needed to enforce inter-element smoothness. On the one hand, the use of very fine meshes throughout the entire domain is usually unnecessary and increases the computational demand, as structural failures usually occur at localized regions while the rest of the structure remains elastic. However, one cannot only predefine failure regions with high resolution, as these regions may not be known a priori. Therefore, an adaptive analysis is desirable where the analysis initiates with a relatively coarse mesh and automatically refines the region where significant inelastic deformation occurs. This requires an accurate prediction of the local quantity related to nonlinearity (such as yielding).

On the other hand, a typical node in a frame element in 2D consists of three DOFs, i.e., two translational DOFs and one rotational DOF. The number of DOFs per node increases in 3D, where the rotation in different planes needs to be defined as well. This is also the case in plate and shell elements. The total number of DOFs relates directly to the size of the system matrices in analysis. The reason that rotational DOFs are required in standard FEA is due to the C^0-continuity

of the underlying basis functions. In other words, it is possible to eliminate rotational DOFs with the use of basis functions of high-order smoothness.

In another context, the design and analysis process requires the passing of data from computer-aided design (CAD) models to the analysis (i.e., finite element) models. However, it must be noted that the CAD geometry is most often constructed using Non-Uniform Rational B-splines (NURBS), whereas FEA uses polynomials to interpolate the geometry and solution variables. This distinction in the use of shape functions introduces an approximation error when re-constructing geometries in standard FEA, especially in the analysis of geometrically complex structures. It was for this reason that isogeometric analysis (IGA) was put forward by Hughes et al. [1] as the first attempt to closely link CAD to FEA. The main idea of IGA is to utilize the same basis functions that are used in CAD to approximate the solution variables in FEA. As a result, the approach avoids the regeneration of the CAD geometry as well as the meshing process in FEA and therefore has the potential to cut the total analysis time by as much as 80% [1]. The direct manipulation of the CAD data also eliminates the possible approximation errors emanating from the process of converting the geometry from CAD to FEA. As a consequence, the exact geometry can be represented at the coarsest level and maintained throughout the entire analysis process. Besides the geometric exactness, it has been demonstrated that the use of higher-order continuous basis functions improves solution accuracy and efficiency [2–8]. Additionally, IGA is fully compatible with standard FEA codes in that a Bézier extraction operator [9] can be employed to provide an element structure in IGA similar to FEA. The optimal convergence of NURBS was observed using the classic infinite plate with a circular hole problem, as is demonstrated in Appendix A.

Although the use of IGA eliminates the approximation errors in converting the geometries from CAD to FEA and provides high-order continuous basis functions, NURBS-based *h*-refinement deteriorates the efficiency of the method due to its global tensor-product structure. "Local refinement" using NURBS can be achieved by using multiple patches with complicated topological constraints on a common boundary, and thus subsequent patch-level refinement is possible [10]. However, this is cumbersome and refinement still propagates within a patch. Another significant drawback of NURBS is that the corresponding control mesh has to be in a quadrilateral shape, which hinders the flexibility and efficiency in local refinement. Moreover, the majority of the state-of-the-art models use trimming curves, which generally leads to gaps and overlaps in the geometry and further makes NURBS not analysis-suitable. In addition, in NURBS-based geometric design and analysis, modeling complicated objects often requires a significant amount of patches, the interfaces of which are usually C^0-continuous or worse (e.g., non-physical gaps and overlaps that are often referred to as non-watertight geometries). In cases where multiple patches need to be connected, additional refinement is required to produce a conforming interface, which results in an excessive number of control points that do not carry significant geometric information. To regain smoothness across multi-patch interfaces, special treatments (e.g., the bending strip method [11]) have to be performed, which unnecessarily increases the computational complexity.

On the contrary, a number of local refinement techniques have been developed to circumvent the restrictive tensor-product structure of NURBS, including hierarchical B-splines [12], T-splines [13], LR B-splines [14], PHT-splines [15] and domain triangulation. Hierarchical B-splines achieve local refinement by successive *h*-refinement on the basis function level. However, they are still restricted to the four-sided meshgrid, and extraordinary points are also not

allowed. In contrast, the use of T-splines successfully handles extraordinary points and enables the representation of complex geometries as a single watertight object. Local refinement can be realized as well. Moreover, analysis-suitable T-splines [16] are both forward and backward compatible with NURBS, which distinguishes themselves from techniques such as subdivision methods [17]. However, T-spline refinement is not as local as expected because local refinement still propagates to satisfy topological constraints to make the resulting T-mesh analysis-suitable. LR B-splines are, to some extent, dual to T-splines [18] in that local refinement is achieved by inserting knot line segments rather than vertices. Local refinement using PHT-splines is completely local due to the reduced global smoothness. However, the low-order smoothness also hinders its application. On the other hand, spline functions constructed over triangulations significantly improve the flexibility in the discretization of geometrically complex spaces and local refinement can be naturally performed by splitting marked triangles. Such methods include hierarchical box splines [19], Powell-Sabin (PS) triangles [20], Bézier triangles [4,21] and Loop subdivision [22]. Among these methods, PS triangles and Bézier triangles are the most popular due to their capability in discretizing arbitrary topologies and relatively simple implementation. The rational Bézier triangles are adopted in addition to NURBS because they resemble the triangular elements of standard FEM in many ways and therefore a large number of existing tools both in the preprocessing and analysis phases can be immediately applied to the current study.

In this context, the goal of the research described herein is to develop IGA-based methods to improve the accuracy and efficiency in modelling a wide variety of structural applications, including large-deformation structural frames, laminated composites with advanced material components, geometrically complex Kirchhoff plates, and damage propagation in brittle materials. Although the present study covers a wide range of topics, it essentially represents an effort in

addressing various modelling obstacles that are difficult to tackle using standard FEA in civil engineering.

To this end, the first section of this chapter gives an overview of IGA in structural applications and describes the scope of the research. The organization of the thesis is provided in the second section.

1.1 Overview and Scope of the Dissertation

Nonlinear analysis of structural frames is important in civil engineering in determining the deformation path and failure mode of structures under extreme loads. A very limited number of studies has been conducted in the last decade to formulate rotation-free beam/frame elements that consider both geometric and material nonlinearities in the framework of IGA, which includes Elguedj et al. [23] who proposed the $\bar{B}$ and $\bar{F}$ method in the NURBS setting for nearly incompressible problems of both elasticity and plasticity, and Zhang and Khandelwal [24] who adopted a nonlocal damage theory to model plasticity growth in beams. In this context, the proposed research work involves the modelling of large-deformation rotation-free structural frames that is capable of capturing the spread of plasticity in an adaptive manner.

Similar to the IGA beam/frame modeling, the analysis of advanced materials such as laminated composites and functionally graded materials can also be conducted in a rotation-free manner. The IGA of laminated composites has been investigated by a number of researchers [25–29], but most of them are based on replacing a heterogeneous laminated plate with a statically equivalent single layer of which the stiffness is computed as a weighted average of the individual layer stiffness. The underlying theory is often referred to as the equivalent single-layer (ESL) theory. The ESL theory is simple and reduces the actual 3D problem into a 2D one, but it incorrectly results in a discontinuity in transverse stress at dissimilar material interfaces. The

correct calculation of 3D stress states is of significant importance, as the failure modes of laminated composites can be extremely complicated due to the fact that the majority of the dominated failure occurs in the inner layers of the composites. Thus, understanding how the stresses and deformations distribute in the full 3D is crucial in determining why, how and under which conditions structural failure will occur. To this end, the layerwise (LW) theories are adopted in the proposed study. The LW theories assume a separate displacement field expansion within each layer, and consider transverse displacement component as C^0-continuous at layer interfaces, thus resulting in a layerwise continuous transverse strain states. The proposed work also involves modelling of sandwich plates with advanced material core such as functionally graded materials.

Aside from the employment of NURBS for the analysis of structural frames and advanced materials, the proposed research is also comprised of the study of domain triangulation method (specifically, rational Bézier triangles) to analyze the behavior of geometrically complex spaces. As is previously discussed, domain triangulation is extremely flexible in the discretization of complicated geometries. However, the use of rational Bézier triangles in the context of IGA has been very rare. A set of techniques is also employed to assist the analysis of various problems, including Lagrange multipliers to raise global smoothness, a Delaunay-based feature-preserving meshing algorithm to capture small geometric features, and a local refinement technique for efficient discretization. The problems of interest involve the study of static and dynamics responses of geometrically complex Kirchhoff plates and implicit higher-order gradient damage models in geometrically complex domains.

To this end, the scope of the current research focuses on improving the accuracy and efficiency in modelling structures and advanced materials in the framework of IGA. The tasks that are designed to achieve the goal are described as follows:

Task 1 – NURBS for the Analysis of Structural Frames and Laminated Composite Plates:

- Employ NURBS for the discretization of the structural frame and laminated composite plate model;
- Derive rotation-free formulations in the context of IGA;
- In the analysis of structural frames, adopt a layer-based discretization to capture the spread of plasticity and include adaptive analysis to improve solution efficiency;
- In the analysis of laminated composites, use Layerwise theory to predict the full 3D stress state and predict the behavior of advanced composites such as a sandwich plate with functionally graded material core;
- Validate the numerical models by comparing the obtained results with solutions from standard FEA and results from existing literature.

Task 2 – Rational Bézier Triangles for the Solution of Geometrically Complex Kirchhoff Plates and Implicit Higher-order Gradient Damage Models:

- Use rational Bézier triangles to generate geometrically exact discretizations of complicated spaces;
- Adopt a Delaunay-based feature-preserving meshing algorithm that admits local geometric features with high resolution;
- Implement a locally refinement technique that produces well-conditioned conforming meshes;
- Employ Lagrange multipliers to explicitly impose high-order continuity;
- Use the previous work as shown in [30] for cylindrical arc-length control and implement a dissipation-based arc-length control due to the load-shedding behavior of damaged structures;

- Investigate and verify the static and dynamic response of geometrically complex Kirchhoff plates with the developed modeling approach;
- Investigate and verify higher-order gradient damage models constructed by the proposed modeling approach.

1.2 Organization

The organization of the dissertation is as follows:

Chapter 2 is a reprint of the work entitled "Adaptive isogeometric analysis in structural frames using a layer-based discretization to model spread of plasticity" [2] published in Computers & Structures. A distributed plasticity isogeometric frame model utilizing a layer-based discretization is formulated to capture the plasticity growth in large-deformation frames.

Chapter 3 is a reprint of the work entitled "Isogeometric analysis of laminated composite and functionally graded sandwich plates based on a layerwise displacement theory" [3] published in Composite Structures. The behavior of laminated composites and sandwich plates with a functionally graded material core is investigated in the context of IGA and a layerwise displacement theory.

Chapter 4 is a reprint of the work entitled "A geometrically exact isogeometric Kirchhoff plate: Feature-preserving automatic meshing and C^1 rational triangular Bézier spline discretizations" [4] published in International Journal for Numerical Methods in Engineering. The analysis of the Kirchhoff plate is performed using rational Bézier triangles in IGA coupled with a Delaunay-based feature-preserving discretization algorithm.

Chapter 5 is a manuscript entitled "Feature-preserving rational Bézier triangles for isogeometric analysis of higher-order gradient damage models" and is ready to submit for review.

In this chapter, the fourth- and sixth-order implicit gradient damage models are studied in the context of the feature-preserving rational Bézier triangulation.

Chapter 6 summarizes the findings of this dissertation and gives future research directions.

Chapter 2 Adaptive Isogeometric Analysis in Structural Frames using a Layer-based Discretization to Model Spread of Plasticity

A distributed plasticity isogeometric frame model utilizing a layer-based discretization is formulated to capture the plasticity growth in large-deformation frames. In our formulation, B-spline basis functions are employed to define the deformation along the length, while a layer-based through-the-thickness discretization is adopted to capture the gradual plastification of the section. This separation of the thickness integration from the length direction enables the full 2D yielding development to be captured while maintaining a 1D data structure. The member-level geometrically nonlinear effects are also included. By introducing a continuity constraint in between two patches, rigid connection between two members is achieved in a multi-patch analysis setting. The formulation includes an adaptive analysis in which knots are inserted based on yield locations. In comparison to conventional layer-based finite elements, fewer degrees of freedom are needed to achieve the same level of accuracy due to the high-order smoothness of B-splines. Compared to existing isogeometric beam elements, the appealing feature is its capability of adaptively capturing the 2D spread of plasticity while maintaining a 1D data structure. The performance of the proposed model is assessed through several numerical examples involving gradual yielding of beams and frames under small and large deformations.

2.1 Introduction

Nonlinear analysis of structural frames is important in civil engineering for determining the load-displacement response of structures under extreme loads. A significant amount of research has been conducted over the past few decades to formulate beam/frame elements the can handle

material and geometric nonlinearities. Material nonlinearities are typically handled by either lumped plasticity or distributed plasticity (i.e., layer) models [31]. The former is more computationally efficient, whereas the latter captures the spread of plasticity in a more accurate manner. Corotational formulations [32] are commonly employed to handle large displacements. While most of the work has focused on displacement-based formulations, recent studies have explored force-based and mixed formulations for improved accuracy [33–38]. While offering improved accuracy and a reduction in the number of degrees of freedom needed to model a structure, force-based elements require computationally expensive state determination algorithms to back-calculate stresses from nodal displacements. Thus, while software for the analysis of structural frames is well-developed and widely used in practice, existing displacement-based, force-based, and mixed element formulations have considerable limitations.

Isogeometric analysis (IGA) has gained significant attention in recent years as a novel computational method that integrates computer-aided design and analysis. It was first introduced by Hughes et al. [1] and has been applied to the analysis of solids, structures and fluids. IGA utilizes Non-Uniform Rational B-splines (NURBS) to represent the geometry as well as to describe the field variables. Thus, CAD drawings can be directly imported into finite element analyses without converting the geometry. While IGA was introduced to streamline the design process for complicated geometries, it has been shown to offer improvements in analysis for even simple geometries, as is shown in this paper. Readers are advised to refer to the original paper by Hughes et al. for a comprehensive overview of IGA. We provide a very brief review of the fundamental concepts for clarity.

In FEA, Lagrange basis functions are mapped into a single element's domain, and the finite elements are then assembled to arrive at the governing equilibrium equations. In IGA, however,

the B-spline parameter space is defined over the entire patch, which is usually comprised of multiple elements. The parameter space is segmented into several elements by a non-decreasing set of coordinates called a knot vector. When the knots are equally spaced in the parameter space, the knot vector is considered uniform; otherwise it is non-uniform. A B-spline basis function is C^{p-1} continuous at a single knot, and C^{p-m} continuous at a repeated knot, where *p* is the degree of polynomial and *m* is the multiplicity of knots. The B-spline basis functions are computed based on the Cox-de Boor recursion formula [1]. With ξ being the natural coordinate, the basis function for *p*=0 is

$$N_{i,0}(\xi)=\begin{cases}1 & \xi_i \le \xi < \xi_{i+1} \\ 0 & \text{otherwise}\end{cases} \tag{2.1}$$

and for *p*=1,2,3,…,

$$N_{i,p}(\xi)=\frac{\xi-\xi_i}{\xi_{i+p}-\xi_i}N_{i,p-1}(\xi)+\frac{\xi_{i+p+1}-\xi}{\xi_{i+p+1}-\xi_{i+1}}N_{i+1,p-1}(\xi) \tag{2.2}$$

The B-splines that form the basis of IGA have the following properties:

- Partition of unity, i.e., $\sum_{i=1}^{n} N_{i,p}(\xi)=1$
- Linear independence, i.e., $\sum_{i=1}^{n} a_i N_{i,p}(\xi)=0 \Leftrightarrow a_i=0, i=1,2,...,n$
- Non-negativity over the entire domain
- Local support, i.e., the basis function is non-zeros only in the domain $\left[\xi_i, \xi_{i+p+1}\right]$

A B-spline curve of polynomial degree *p* can then be constructed by the linear combination

of control points P_i and its respective basis functions:

$$C(\xi) = \sum_{i=1}^{n} N_{i,p}(\xi) P_i \tag{2.3}$$

An advantage of IGA lies in the fact that all degrees of freedom (DOFs) are displacement-based, meaning that elements are rotation-free. This presents a significant opportunity for reducing the size of stiffness matrices for large structural systems, thereby offering significant savings in computational time. Moreover, recent studies [3,39,40] on IGA have indicated that the use of NURBS basis functions give improved accuracy over conventional finite element analysis (FEA) for certain applications.

Isogeometric analysis of beams has been studied by a number of researchers, and related papers cover shape optimization of beams [41], locking-free Timoshenko beams [42–44] and Kirchhoff-Love space rods [45]. Recent developments include the isogeometric analysis of plane-curved beams [46], which was based on the Timoshenko beam theory, and an isogeometric collocation method for thin beams and plates [47]. An implicit G1 multi-patch Kirchhoff-Love space rod was contributed by Greco and Cuomo [48], in which the displacements of the first and last control points within one patch were decomposed using polar coordinates to obtain an automatic non-singular stiffness matrix. More recently, a shear deformable isogeometric beam using a single-variable formulation was developed [49].

While isogeometric analysis of beams has been shown to yield accurate results, the majority of previous models are in the range of elastic analysis and few have applied IGA to study the inelastic response of beam/frame structures loaded beyond yielding. The use of IGA for material nonlinear problems [23,50–53] has focused on the study of 2D and 3D continuums, which requires a tensor product of NURBS basis functions in multiple directions and therefore an

excessive number of DOFs has to be introduced. Recently, a nonlocal damage theory was applied to study the inelastic behavior of beams [24]. However, this method involves in computing the six-order derivative of the nonlocal integral operator, which is computationally expensive. Additionally, it is not able to predict the full plasticity growth of the section.

Within this context, we propose a layer-based distributed plasticity isogeometric frame model based on the Euler-Bernoulli beam theory. Member-level geometrically nonlinear effects are accounted for through the inclusion of high-order strain terms. The formulation is therefore suitable for moderate deformations and rotations. The novelty and strength of this paper are:

- Instead of using tensor-product splines, the 1D B-spline basis function is used to represent the parametric domain in the length direction. The separation in integrating the layer-based thickness direction from the length direction significantly reduces the size of system matrices.
- Utilizing a layer-based discretization in the through-the-thickness direction not only allows the gradual localized plastification of the section to be captured accurately, but it also serves as a gradient-based a posteriori error estimator for adaptive analysis in the sense that localized yielding results in sharp curvatures which, in turn, are a perfect indication of the need for refinement.
- Yielding information is collected at the integration points in the layer to guide the adaptive refinement process. Lobatto quadrature rule is recommended in lieu of traditional Gaussian quadrature because Lobatto quadrature includes integration points at the ends of elements where plastic hinges are most likely to occur (e.g., connections between beams and columns, boundary condition locations, mid-span of members).

- A G^1 (i.e., geometrically continuous) continuity constraint is implemented in between patches, thereby adding rotational stiffness at beam-column connections. The constraint equation overlaps one control point on each side of the patch interface and only allows for yielding in the neighborhood of connections, rather than in the connections themselves. Therefore, the beam-column connection maintains rigidity throughout the analysis and plastic hinges are only allowed to form in beams and columns. This is rather important from a realistic structural point of view as yielding occurs at beam-column connections in traditional FE beam elements.
- The use of B-spline basis functions yields a rotation-free discretization, which represents great computational saving as compared to FEA.

2.2 Formulation

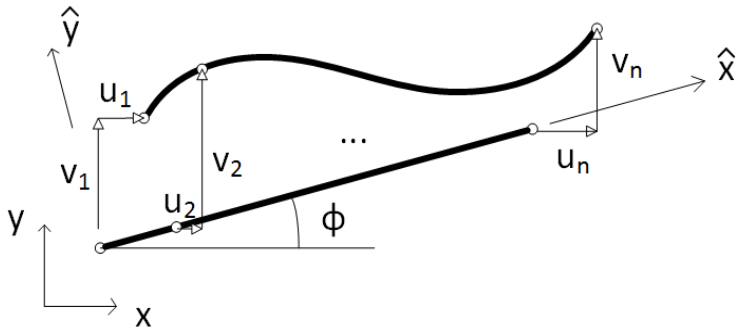

Figure 2-1: Degrees of freedom of a layer-based IGA element

In this section, the governing equations of the distributed plasticity isogeometric frame model are presented. The model is "rotation-free" in the sense that the displaced shape is defined entirely in terms of the horizontal and vertical translations, u_i and v_i, respectively, at the n control points, as illustrated in Fig. 2-1. To enable material-nonlinear analysis, the patch is discretized into m layers [30], as shown in Fig. 2-2. It is assumed that the thickness of each layer is relatively small such that stress and strain are lumped at each layer across the section.

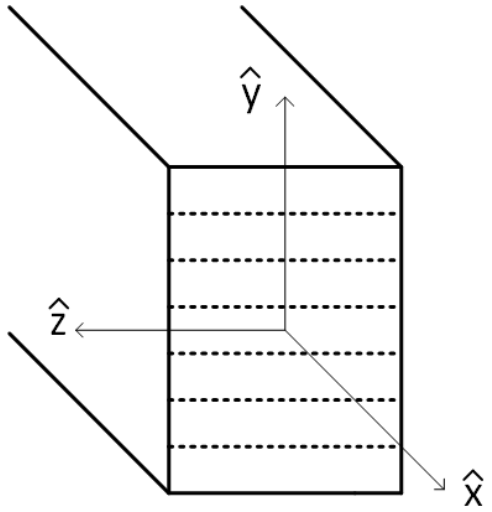

Figure 2-2: Layer discretization of the cross-section

The Euler-Bernoulli hypothesis is employed. The mechanical strain in layer j is composed of axial and bending deformations and is given as

$$\varepsilon_j = \frac{d\hat{u}}{d\hat{x}} - \hat{y}_j \frac{d^2\hat{v}}{d\hat{x}^2} + \frac{1}{2}\left[\left(\frac{d\hat{u}}{d\hat{x}}\right)^2 + \left(\frac{d\hat{v}}{d\hat{x}}\right)^2\right] \tag{2.4}$$

Here, $\hat{u}$ is the axial deformation and $\hat{v}$ is the transverse deformation in local $\hat{x}\hat{y}$ coordinates. Note that the higher-order terms associated with large deformations are included. A natural coordinate ξ is defined in the longitudinal direction to facilitate the numerical integration of the stiffness matrix. Thus, Eq. (2.4) becomes

$$\varepsilon_j = \frac{d\hat{u}}{d\xi}\frac{d\xi}{d\hat{x}} - y_j \frac{d^2\hat{v}}{d\xi^2}\frac{d\xi^2}{d\hat{x}^2} + \frac{1}{2}\left[\left(\frac{d\hat{u}}{d\xi}\frac{d\xi}{d\hat{x}}\right)^2 + \left(\frac{d\hat{v}}{d\xi}\frac{d\xi}{d\hat{x}}\right)^2\right] \tag{2.5}$$

If we define $J = d\hat{x}/d\xi$ as the Jacobian, Eq. (2.5) becomes

$$\varepsilon_j = \frac{1}{J}\frac{d\hat{u}}{d\xi} - \frac{1}{J^2}\hat{y}_j \frac{d^2\hat{v}}{d\xi^2} + \frac{1}{2J^2}\left[\left(\frac{d\hat{u}}{d\xi}\right)^2 + \left(\frac{d\hat{v}}{d\xi}\right)^2\right] \tag{2.6}$$

Displacements $\hat{u}$ and $\hat{v}$ are discretized using NURBS basis functions as

$$\hat{u}(\xi) = \sum_{i=1}^{n} R_{i,p}(\xi) \cdot \hat{u}_i = \mathbf{R}(\xi)\hat{\mathbf{u}} \tag{2.7}$$

$$\hat{v}(\xi) = \sum_{i=1}^{n} R_{i,p}(\xi) \cdot \hat{v}_i = \mathbf{R}(\xi)\hat{\mathbf{v}}$$

where $\hat{u}_i$ and $\hat{v}_i$ are respectively the axial and transverse displacements of the control point *i*, and $R_{i,p}$ is the NURBS basis function corresponding to control point *i* for polynomial of order *p*. Substituting Eq. (2.7) into Eq. (2.6) gives

$$\varepsilon_j = \frac{1}{J}\frac{d}{d\xi}\mathbf{R}(\xi)\hat{\mathbf{u}} - \frac{1}{J^2}\hat{y}_j\frac{d^2}{d\xi^2}\mathbf{R}(\xi)\hat{\mathbf{v}} + \frac{1}{2J^2}\left(\hat{\mathbf{u}}^T\frac{d\mathbf{R}(\xi)}{d\xi}^T\frac{d\mathbf{R}(\xi)}{d\xi}\hat{\mathbf{u}} + \hat{\mathbf{v}}^T\frac{d\mathbf{R}(\xi)}{d\xi}^T\frac{d\mathbf{R}(\xi)}{d\xi}\hat{\mathbf{v}}\right) \tag{2.8}$$

Eq. (2.8) consists of linear and nonlinear terms, which are expressed as follows:

$$\varepsilon_j = \varepsilon_j^l + \varepsilon_j^{nl} \tag{2.9}$$

where

$$\varepsilon_j^l = \frac{1}{J}\frac{d}{d\xi}\mathbf{R}(\xi)\hat{\mathbf{u}} - \frac{1}{J^2}\hat{y}_j\frac{d^2}{d\xi^2}\mathbf{R}(\xi)\hat{\mathbf{v}} \tag{2.10}$$

$$\varepsilon_j^{nl} = \frac{1}{2J^2}\left(\hat{\mathbf{u}}^T\frac{d\mathbf{R}(\xi)}{d\xi}^T\frac{d\mathbf{R}(\xi)}{d\xi}\hat{\mathbf{u}} + \hat{\mathbf{v}}^T\frac{d\mathbf{R}(\xi)}{d\xi}^T\frac{d\mathbf{R}(\xi)}{d\xi}\hat{\mathbf{v}}\right) \tag{2.11}$$

The linear term in Eq. (2.10) can be written in matrix form as

$$\varepsilon_j^l = \mathbf{B}_j\hat{\mathbf{d}} \tag{2.12}$$

where the strain-displacement matrix $\mathbf{B}_j$ for layer *j* and the vector of control point displacements $\hat{\mathbf{d}}$ in local coordinates are given as

$$\mathbf{B}_j = \left[\frac{1}{J}\frac{dR_{1,p}(\xi)}{d\xi} \quad \cdots \quad \frac{1}{J}\frac{dR_{n,p}(\xi)}{d\xi} \quad -\frac{1}{J^2}\hat{y}_j\frac{d^2R_{1,p}(\xi)}{d\xi^2} \quad \cdots \quad -\frac{1}{J^2}\hat{y}_j\frac{d^2R_{n,p}(\xi)}{d\xi^2} \right] \tag{2.13}$$

$$\hat{\mathbf{d}}^T = \left[\hat{u}_1 \quad \cdots \quad \hat{u}_n \quad \hat{v}_1 \quad \cdots \quad \hat{v}_n \right]^T \tag{2.14}$$

The nonlinear term in Eq. (2.11) can be written in matrix form as

$$\varepsilon_j^{NL} = \frac{1}{2}\left(\hat{\mathbf{d}}^T \begin{bmatrix} (\mathbf{R}')^T & \mathbf{0} \\ \mathbf{0} & (\mathbf{R}')^T \end{bmatrix} \begin{bmatrix} \mathbf{R}' & \mathbf{0} \\ \mathbf{0} & \mathbf{R}' \end{bmatrix} \hat{\mathbf{d}} \right) \tag{2.15}$$

where

$$\mathbf{R}' = \left[\frac{1}{J}\frac{dR_{1,p}(\xi)}{d\xi} \quad \cdots \quad \frac{1}{J}\frac{dR_{n,p}(\xi)}{d\xi} \right] \tag{2.16}$$

To arrive at the stiffness matrix, the method of virtual work is employed. The increment in internal virtual work is equated to the increment in external virtual work, i.e.,

$$\Delta\delta W_{\text{int}} = \Delta\delta W_{\text{ext}} \tag{2.17}$$

The internal virtual work is determined by summing the strain energy over the *m* layers, i.e.,

$$\Delta\delta W_{\text{int}} = \int_V \delta\varepsilon \cdot \Delta\sigma dV = \sum_{j=1}^{m} \int_L \delta\varepsilon_j A_j \Delta\sigma_j d\hat{x} = \sum_{j=1}^{m} \left(\int_L \delta\varepsilon_j^l A_j \Delta\sigma_j d\hat{x} + \int_L \Delta\delta\varepsilon_j^{nl} A_j \sigma_j d\hat{x} \right) \tag{2.18}$$

Here, A_j is the cross-sectional area associated with layer *j*, and *L* is the length of the patch. The variation in strain is given as

$$\delta\varepsilon_j^l = \mathbf{B}_j \delta\hat{\mathbf{d}} \quad , \tag{2.19}$$

$$\delta\varepsilon_j^{nl} = \left(\delta\hat{\mathbf{d}}^T \begin{bmatrix} (\mathbf{R}')^T & \mathbf{0} \\ \mathbf{0} & (\mathbf{R}')^T \end{bmatrix} \begin{bmatrix} \mathbf{R}' & \mathbf{0} \\ \mathbf{0} & \mathbf{R}' \end{bmatrix} \hat{\mathbf{d}} \right)$$

In the linear term in Eq. (2.18), the increment in stress is defined as

$$\Delta\sigma_j = E_j \Delta\varepsilon_j = E_j \mathbf{B}_j \Delta\hat{\mathbf{d}} \tag{2.20}$$

Here, E_j is the tangent modulus in layer j, which is determined from the constitutive law for the material. In the nonlinear term, it is recognized that $A_j\sigma_j$ is the internal axial force in the layer, i.e., F_j^{axial}. Substituting these relationships into Eq. (2.18) gives

$$\Delta\delta W_{\text{int}} = \sum_{j=1}^{m}\left[\int_{-1}^{1} \delta\hat{\mathbf{d}}^T \mathbf{B}_j{}^T E_j A_j \mathbf{B}_j \Delta\hat{\mathbf{d}} J d\xi + \int_{-1}^{1}\left(\delta\hat{\mathbf{d}}^T \begin{bmatrix} (\mathbf{R}')^T & \mathbf{0} \\ \mathbf{0} & (\mathbf{R}')^T \end{bmatrix}\begin{bmatrix} \mathbf{R}' & \mathbf{0} \\ \mathbf{0} & \mathbf{R}' \end{bmatrix}\Delta\hat{\mathbf{d}}\right) F_j^{axial} J d\xi\right] \tag{2.21}$$

It follows from Eq. (2.21) that the tangent stiffness matrix in local coordinates is

$$\hat{\mathbf{k}} = \hat{\mathbf{k}}^l + \hat{\mathbf{k}}^g \tag{2.22}$$

where the geometrically linear component of the stiffness matrix is given as

$$\hat{\mathbf{k}}^l = \sum_{j=1}^{m}\int_{-1}^{1} \mathbf{B}_j{}^T E_j A_j \mathbf{B}_j J d\xi \tag{2.23}$$

and the geometrically nonlinear component of the stiffness matrix is

$$\hat{\mathbf{k}}^{nl} = \sum_{j=1}^{m} F_j^{axial}\int_{-1}^{1}\left(\begin{bmatrix} (\mathbf{R}')^T & \mathbf{0} \\ \mathbf{0} & (\mathbf{R}')^T \end{bmatrix}\begin{bmatrix} \mathbf{R}' & \mathbf{0} \\ \mathbf{0} & \mathbf{R}' \end{bmatrix}\right) J d\xi \tag{2.24}$$

Note that inelastic behavior is captured in the geometrically linear stiffness matrix through the evaluation of the tangent modulus E_j based on the constitutive law for the material. With the incremental equations formulated, the modified Newton-Raphson method is adopted to solve the problem iteratively, in which the internal force is derived based on the stresses calculated using Eq. (2.20). The solution of the governing equilibrium equations follows the same procedure as is used in conventional finite element analysis and therefore is not discussed here for brevity.

Since all DOFs are displacement-based, special treatment is required when applying moment as an external load. In Eq. (2.17), the external virtual work is given as

$$\Delta\delta W_{\text{ext}} = \sum_{i=1}^{n}\left(\delta\hat{u}_i\Delta\hat{f}_{x,i} + \delta\hat{v}_i\Delta\hat{f}_{y,i} + \delta\hat{\theta}_i\Delta\hat{m}_{z,i}\right) \tag{2.25}$$

where $\Delta\hat{f}_{x,i}$, $\Delta\hat{f}_{y,i}$ and $\Delta\hat{m}_{z,i}$ are the external loads in the local $\hat{x}$ and $\hat{y}$ direction and moments, respectively. Rotation θ is defined as the derivative of the displacement v with respect to x. From Eq. (2.17),

$$\delta\hat{\theta}_i = \frac{d\delta\hat{v}(x_i)}{dx} = \frac{1}{J}\sum_{k=1}^{n}\frac{dR_{k,p}(\xi_i)}{d\xi}\delta\hat{v}_k \tag{2.26}$$

Eqs. (25) and (26) yield a generalized force vector, given as:

$$\Delta\hat{\mathbf{f}}^T = \left[\Delta\hat{f}_{x,1} \quad \cdots \quad \Delta\hat{f}_{x,n} \quad \left(\Delta\hat{f}_{y,1} + \frac{1}{J}\sum_{i=1}^{n}\frac{dR_{i,p}(\xi_1)}{d\xi}\Delta\hat{m}_{z,i}\right) \quad \cdots \quad \left(\Delta\hat{f}_{y,n} + \frac{1}{J}\sum_{i=1}^{n}\frac{dR_{i,p}(\xi_n)}{d\xi}\Delta\hat{m}_{z,i}\right)\right]^T \tag{2.27}$$

Eq. (2.27) transforms external moments into generalized external forces so that rotational DOFs are not required when applying external moments.

Note that the above variables are expressed in local coordinates, whereas the structural equilibrium equations are more conveniently written in global coordinates. For an element with local $\hat{x}$ axis oriented at angle ϕ from the global x axis, the relationships between displacements, forces, and stiffness matrices in local and global coordinates are given as

$$\hat{\mathbf{d}} = \mathbf{T}\mathbf{d},\ \hat{\mathbf{f}} = \mathbf{T}\mathbf{f},\ \mathbf{k} = \mathbf{T}^T\hat{\mathbf{k}}\mathbf{T} \tag{2.28}$$

where the transformation matrix **T** is given as

$$\mathbf{T} = \begin{bmatrix} \mathbf{C} & \mathbf{S} \\ -\mathbf{S} & \mathbf{C} \end{bmatrix} \tag{2.29}$$

In Eq. (2.29), $\mathbf{C} = \cos\phi \cdot \mathbf{I}$ and $\mathbf{S} = \sin\phi \cdot \mathbf{I}$, where $\mathbf{I}$ is the identity matrix. The transformation is calculated based on the original (i.e., undeformed) configuration of the element and therefore is suitable for moderate displacements only.

2.3 Continuity Constraints for Multi-patch Analysis

To include rigidity in beam-column connections in frame structures, the basis functions employed must be at least C^1 continuous. This is easily attained by using one-patch isogeometric analysis due to the inherent high-order continuity of NURBS basis functions. However, when it comes to multi-patch analysis, connections between two patches are C^0 continuous and therefore additional constraints are needed to enforce slope compatibility. For this reason, we introduce a continuity constraint that equates the rotations at the connecting point of two patches, thus adding rotational stiffness where a rigid connection appears. Owing to the fact that this additional constraint overlaps one control point on each side of the patch interface, yielding at the joint between two patches is not allowed. Therefore, the beam-column connection itself maintains rigidity throughout the analysis and plastic hinges are only allowed to form in beams and columns.

To enforce compatibility in slope, the constraint equation that is employed equates the rotation θ at the ends of two elements. Because the element is rotation-free, the constraint equation needs to be expressed in terms of the translation vector **d**. Recall that the rotation at control point *i* in an element is given as

$$\theta_i = \hat{\theta}_i = \frac{d\hat{v}(x_i)}{dx} = \frac{1}{J}\sum_{k=1}^{n} \frac{dR_{k,p}(\xi_i)}{d\xi}\hat{v}_k \tag{2.30}$$

Eq. (2.30) can be written in the following short hand form:

$$\theta_i = \mathbf{H}_i \hat{\mathbf{d}} = \mathbf{H}_i \mathbf{T} \mathbf{d} \tag{2.31}$$

where

$$\mathbf{H}_i = \left[0 \quad \cdots \quad 0 \quad \frac{1}{J}\frac{dR_{1,p}(\xi_i)}{d\xi} \quad \cdots \quad \frac{1}{J}\frac{dR_{n,p}(\xi_i)}{d\xi} \right] \tag{2.32}$$

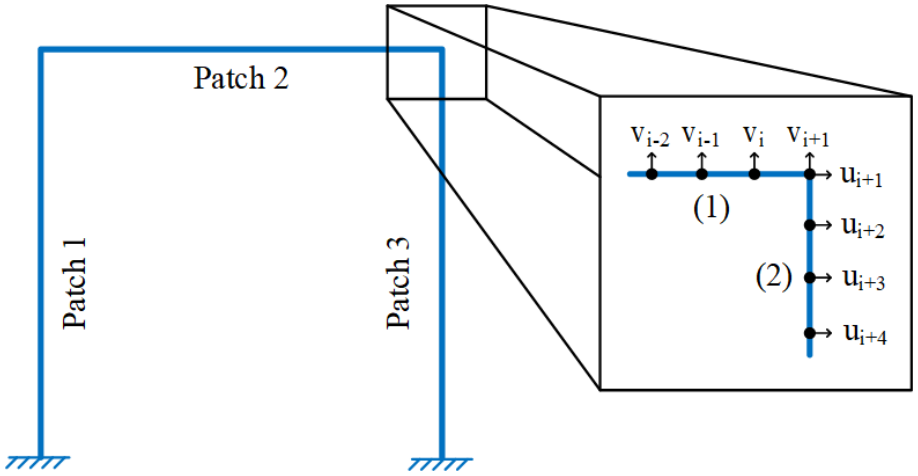

Figure 2-3: Degrees of freedom involved in a constraint representing a rigid beam-to-column connection

For elements (1) and (2) shown in Fig. 2-3, control points *i-2*, *i-1*, *i*, *i+1* and *i+1*, *i+2*, *i+3*, *i+4* are employed to describe their deformation, respectively. The rotation at control point *i+1* calculated within element (1) is equated to the rotation at the same control point calculated based on the deformation of element (2), i.e.,

$$\theta_{i+1}^{(1)} = \theta_{i+1}^{(2)} \tag{2.33}$$

From Eq. (2.31),

$$\mathbf{H}_n^{(1)} \mathbf{T}^{(1)} \mathbf{d}^{(1)} = \mathbf{H}_1^{(2)} \mathbf{T}^{(2)} \mathbf{d}^{(2)} \tag{2.34}$$

For a rigid (or fixed) support at the end of a member, the constraint equation simplifies such that the relative transverse displacement at the end point and first interior point are set to zero.

Using constraints such as those given in Eq. (2.34), degrees of freedom from the structural system are eliminated from the governing equations. Specifically, for structural displacements **D**, we can divide the displacement vector into eliminated (i.e., constrained) degrees of freedom $\mathbf{D_e}$ and free (i.e., unconstrained) degrees of freedom $\mathbf{D_f}$. Constraint equations such as those given in Eq. (2.34) are combined to give the constraint equations for the structural system, which are expressed as

$$\begin{bmatrix}\mathbf{G_e} & \mathbf{G_f}\end{bmatrix}\begin{Bmatrix}\mathbf{D_e}\\ \mathbf{D_f}\end{Bmatrix} = \mathbf{0} \tag{2.35}$$

where $\mathbf{G_e}$ and $\mathbf{G_f}$ are the coefficients derived from Eq. (2.34). An equivalent stiffness matrix $\overline{\mathbf{K}}$ and force vector $\overline{\mathbf{P}}$ are then calculated in terms of the reduced (i.e., unconstrained) degrees of freedom. If the governing equations are partitioned as follows,

$$\begin{Bmatrix}\mathbf{P_e}\\ \mathbf{P_f}\end{Bmatrix} = \begin{bmatrix}\mathbf{K_{ee}} & \mathbf{K_{ef}}\\ \mathbf{K_{fe}} & \mathbf{K_{ff}}\end{bmatrix}\begin{Bmatrix}\mathbf{D_e}\\ \mathbf{D_f}\end{Bmatrix} \tag{2.36}$$

the equivalent stiffness matrix and force vector are [54]

$$\overline{\mathbf{K}} = \left(\mathbf{K_{ff}} + \mathbf{K_{fe}}\boldsymbol{\Gamma} + \boldsymbol{\Gamma}^T\mathbf{K_{ef}} + \boldsymbol{\Gamma}^T\mathbf{K_{ee}}\boldsymbol{\Gamma}\right) \tag{2.37}$$

$$\overline{\mathbf{P}} = \mathbf{P_f} + \boldsymbol{\Gamma}^T\mathbf{P_e} \tag{2.38}$$

where

$$\boldsymbol{\Gamma} = \mathbf{G_e}^{-1}\mathbf{G_f} \tag{2.39}$$

Note that, under the circumstance where three or more members frame into one rigid connection, the two overlapping control points in the rigid connection region cannot be chosen to be eliminated simultaneously in order to avoid the singularity of $\mathbf{G_e}$.

2.4 Yielding-based Adaptive Analysis

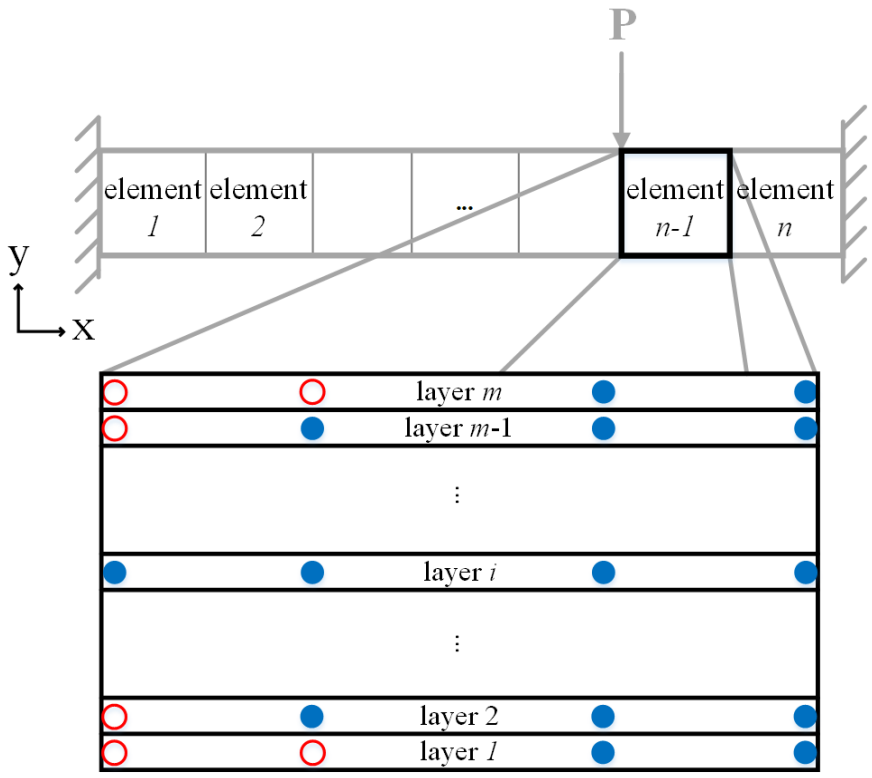

Figure 2-4: Yielding data at quadrature points

In order to reduce the total number of DOFs in the system and realize localized strategic refinement, an adaptive isogeometric analysis using the proposed layer model is studied in this section. The principal idea is to perform knot insertion in the regions of the model where yielding is detected. The location of the knot inserted is based on the plastic deformation data collected at the integration points. As shown in Fig. 2-4, the integration points are plotted at the layer level. The red dots indicate that yielding has occurred at the location of integration points, whereas the blue dots demonstrate that there is no yielding in the associated region. Conceptually, in the adaptive IGA, a knot is inserted near the region of yielding when yielding is detected in the model. Because yielding is tracked at the integration points, the rate of convergence of the adaptive algorithm is dependent on the integration scheme that is utilized. Lobatto quadrature rule is

recommended in lieu of Gaussian quadrature. This is because Lobatto quadrature includes integration points at the ends of the patch. The inclusion of integration points at the ends of the patch makes the model more suitable for the inelastic analysis of structural frames due to the fact that plastic hinges are most likely to occur at the ends of a member (e.g., connections between beams and columns, boundary condition locations, mid-span of members). The insertion of new knots leads to the change of control point locations, which refines the mesh in the physical domain. Subsequently, the recommended Lobatto quadrature rule is applied on the new elements, and then strains and stresses are calculated at the new integration points.

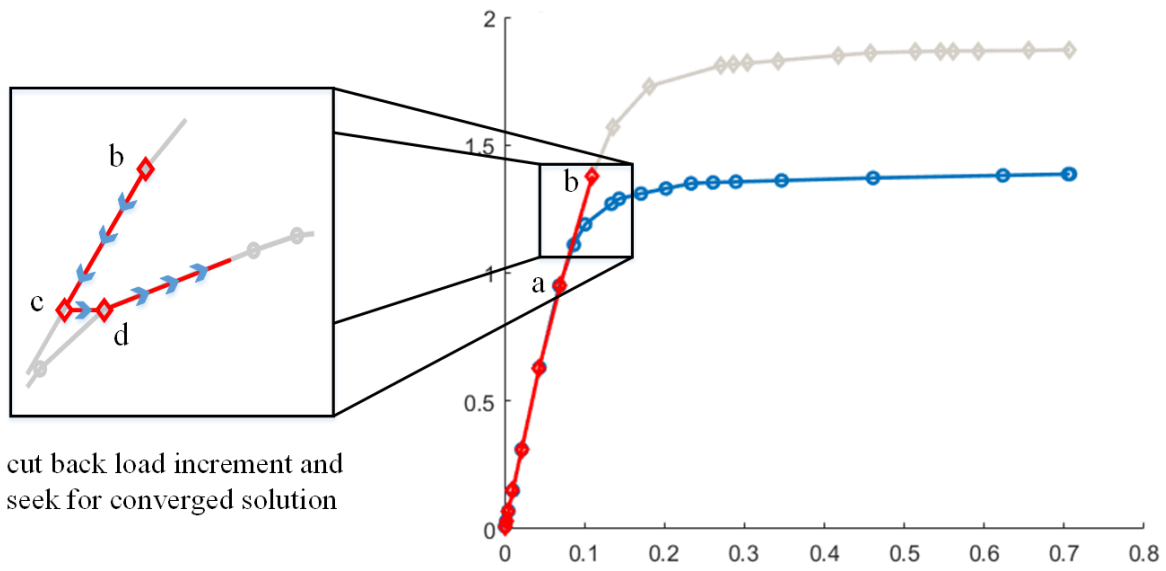

Figure 2-5: Performance of Lobatto quadrature (indicated in blue) vs. Gauss quadrature (in red)

An example is shown in Fig. 2-5 to illustrate the differences between adaptive meshing using Lobatto quadrature versus Gaussian quadrature. Consider a structural member (e.g., a cantilever beam) with load increasing to the ultimate capacity of the member. As shown in Fig. 2-5, the structure behaves elastically until yielding occurs at point *a*. At initial yield (point *a*), only a small portion of the section at the end of the member has yielded. Due to the first Gauss point being

located at some distance from the end of the element, yielding is not detected and the structure is thus modeled as elastic. Using Lobatto quadrature, however, yielding is detected at the onset (point *a* in Fig. 2-5). The model using Gauss quadrature continues to simulate linear elasticity until point *b*, where yielding at the first Gauss point is detected. However, the internal force corresponding to point *b* is likely to be greater than the actual capacity of the structure due to the fact that significant yielding has already occurred, which can be detected by refining the mesh. When the mesh is refined, however, the load increment must be cut back (point *c*) and the program re-runs the iteration, arriving at the converged solution at point *d*. One can see that the refinement using Gauss quadrature will lead to the correct solution as the mesh is refined, but requires significantly more computational effort due to the fact that the Gauss points do not correspond to the locations of yielding in the member.

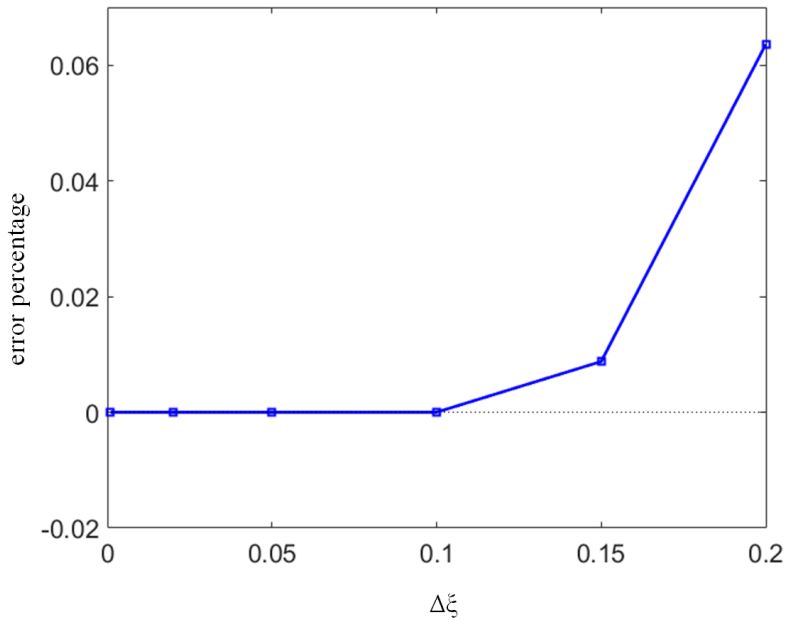

Figure 2-6: Error as a function of knot insertion distance

For the insertion of knots in the adaptive algorithm, it is suggested that a new knot is inserted in the knot vector at a distance $\Delta\xi$ to both sides of the yielded integration point (or to one side

for integration points that lie at the ends of the element). A parametric analysis was performed for a fixed-fixed beam (see the first example in numerical examples section) in order to determine the optimal placement of the inserted knots. Fig. 2-6 shows the percent error for increasing $\Delta\xi$, which is measured against the converged finite element solution. In general, it is recommended that $\Delta\xi$ be chosen as 0.1 to keep errors close to zero. Note that knot insertion is abandoned if there is a knot already existing within the distance of $\Delta\xi$. This is done to avoid unnecessary refinement of the mesh.

With the positions decided for the new knots, the next step is to recalculate the coordinates of the new control points by imposing the geometry to remain unchanged. Note that since the weights are equal for the frame element, the displacements at the new control points are interpolated based on the converged deformation of the old system (i.e., the unrefined IGA model) using the previous B-spline basis functions. In this way, the patch is locally refined at the place of yielding. Fig. 2-7 plots the original B-spline basis function versus the refined one. For a cantilever beam with yielding occurring at the left support, the original knot vector is Ξ =[0 0 0 0.5 1 1 1]. Assume that three new knots are inserted at $\xi = 0.1,0.2,0.3$ due to detected yielding at the left end of the member, which increases the number of basis functions from four to seven (as plotted in Fig. 2-7).

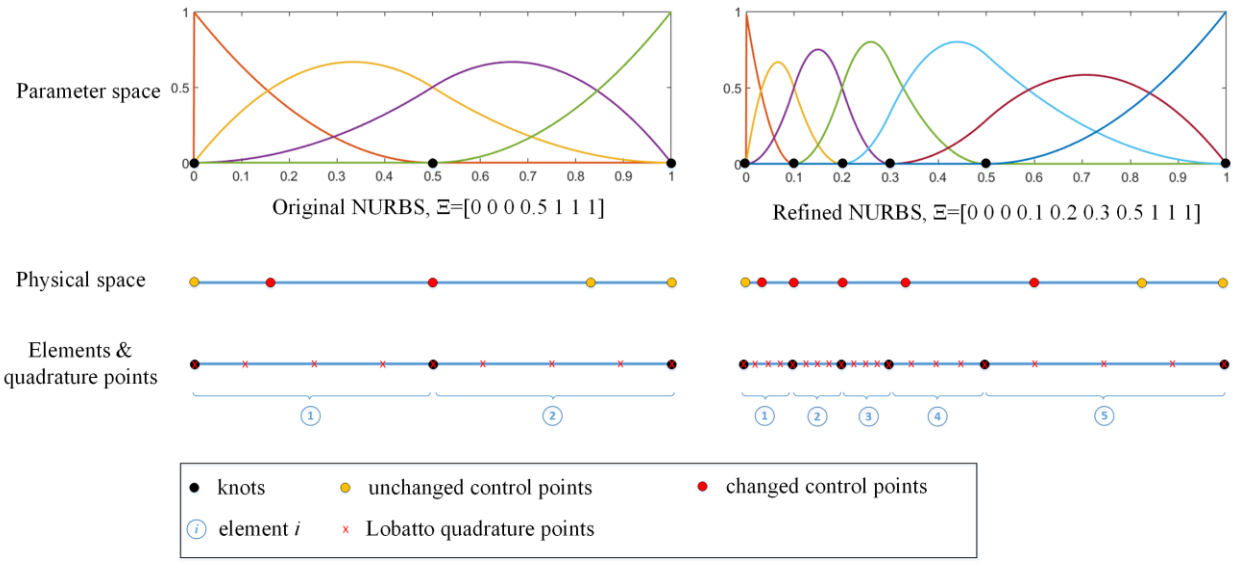

Figure 2-7: Original/Refined space in parameter and physical domain

2.5 Numerical Examples

This section is dedicated to verifying the formulation of the large-deformation, distributed plasticity frame element. The IGA frame model was programmed in Matlab, and the modified Newton-Raphson method is adopted to solve the problem iteratively. In order for the results to be accurate, n Gauss-Lobatto integration points are used for polynomials of degree $2n$-3. For comparison purposes, the B23 element in Abaqus was selected. The B23 element is a 2D displacement-based element that has five integration points through the cross-section. While it is acknowledged that there are several advanced frame element formulations in the literature that give improved performance over the traditional displacement-based elements, the purpose of this study is to show a comparison between IGA and standard FEA. Therefore, we did not attempt to draw comparisons to other advanced finite element models, such as those that are force-based or use mixed methods.

2.5.1 Fixed-Fixed Beam with Point Load

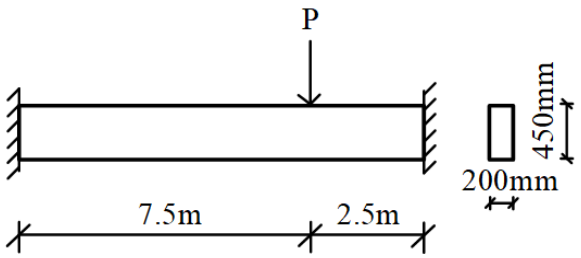

Figure 2-8: Dimensions of the fixed-fixed beam model

In order to assess the proposed formulation under inelastic loading conditions, a fixed-fixed beam subjected to a point load P at $0.75L$ is chosen, as shown in Fig. 2-8. The Young's modulus of the beam is 200 GPa, and the yield strength is 250 MPa. The material is defined as being elastic-perfectly plastic. Geometric details of the beam can be found in Fig. 2-8.

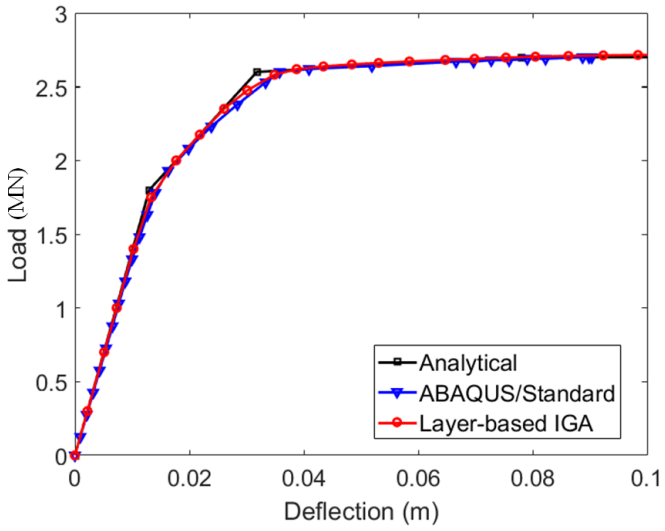

Figure 2-9: Load-deflection curve of the fixed-fixed beam

The system is statically indeterminate to the second degree in regards to the modeling of the beam, and the expected deformation is such that three plastic hinges form before the structure reaches total collapse. An analytical solution based on plastic analysis (i.e., an approximate analysis that assumes the plastic hinges form instantaneously when the moment reaches the plastic

moment capacity of the section) is also obtained to verify the numerical results. Based on the curves in Fig. 2-9, it is observed that the IGA beam with a uniform discretization of 13 control points yields good agreement with the FEM beam modeled using 100 elements. Note that, in this problem, one control point from IGA corresponds to only one translational degree of freedom (i.e., since axial deformation is not considered in this structure). Similarly, one node in FEM corresponds to two degrees of freedom, namely, one translation and one rotation.

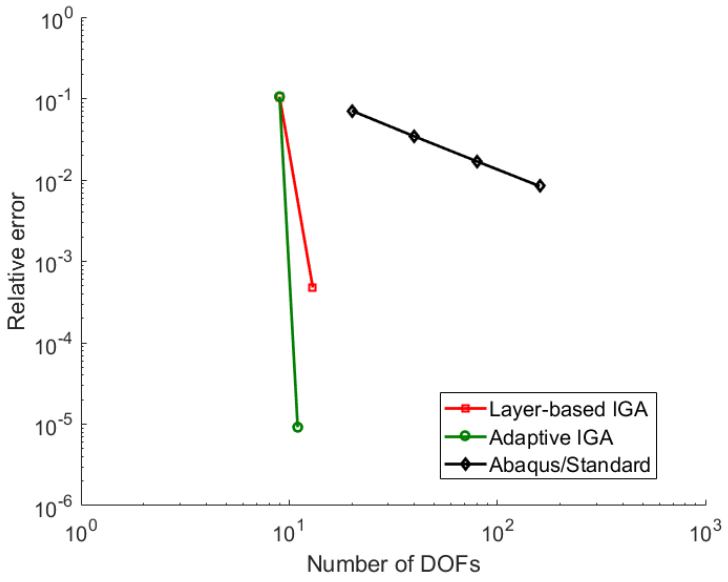

Figure 2-10: Error ratio vs. Number of DOFs curve

The comparison of convergence rates between isogeometric analysis and traditional finite element method is also studied, and results are shown in Fig. 2-10. The relative error ratio ϕ is calculated as follows:

$$\phi = \frac{v_{conv} - v}{v_{conv}} \tag{2.40}$$

where v_{conv} is the converged displacement at the point of loading and v denotes the displacement at the point of loading predicted by the model having a certain number of DOFs.

It is observed that IGA requires considerably fewer degrees of freedom to reach similar level of accuracy in comparison with the conventional finite element method. This is owing to the high-order continuity of NURBS shape functions within one patch in isogeometric analysis so that compatibility is automatically satisfied without the need for rotational degrees of freedom. We also see an even faster convergence using the adaptive IGA, with the error ratio being 0.0009% for 11 DOFs. The non-adaptive IGA (i.e., the IGA with uniform mesh) requires nearly double the number of DOFs to achieve the same level of accuracy, as is also proved by the slopes (i.e., convergence rates) shown in Fig. 2-10. Thus, it is concluded that the strategic insertion of knots in the plastic hinge regions is a significant improvement.

2.5.2 Inelastic Cantilever Subjected to Cyclic Load

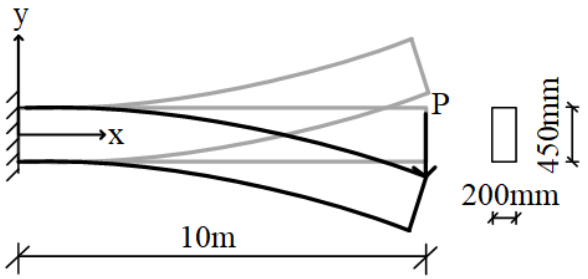

Figure 2-11: Dimensions of the inelastic cantilever model

This section is dedicated to the further investigation of the inelastic behavior of the cantilever beam using isogeometric analysis. A cyclic load is added at the tip of the cantilever, as shown in Fig. 2-11. The Ramberg-Osgood hardening model is employed in the material definition. The yield strength and ultimate strength are 250 MPa and 550 MPa, respectively. The yield stress function is defined [55] as follows:

$$Y(\alpha) = \sigma_y + C \cdot \alpha^m \tag{2.41}$$

where σ_y is the yield strength, α is the equivalent plastic strain, *C* and *m* are material constants.

In this case, C=30 MPa, m=0.45.

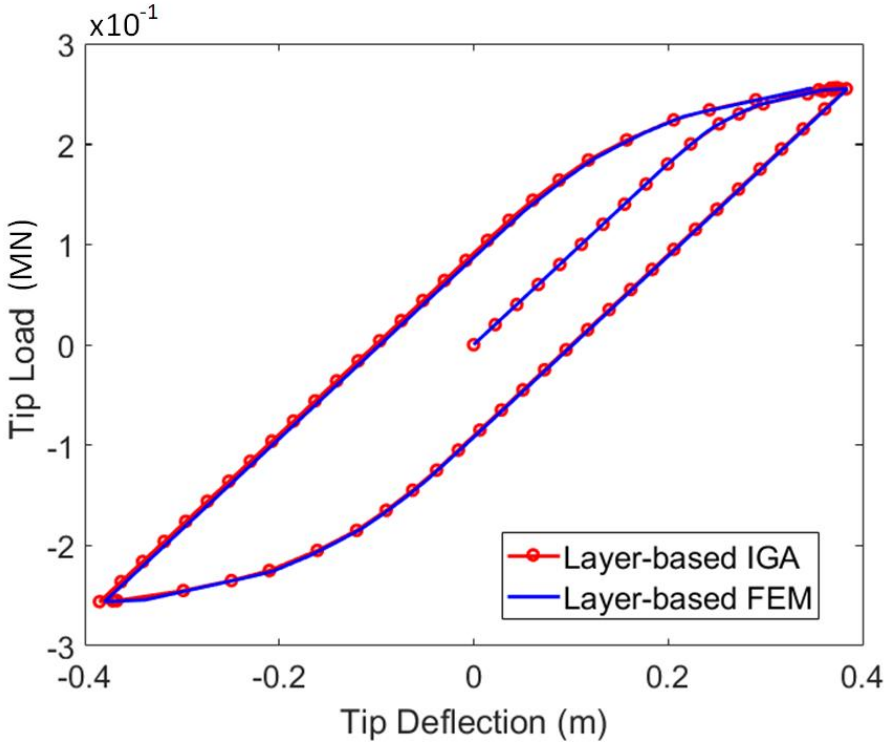

Figure 2-12: Load-deflection curve of the inelastic cantilever

The hysteretic behavior of the cantilever beam is plotted in Fig. 2-12. It is observed that the layer-based IGA captures the spread of plasticity accurately and maintains good hysteretic performance in comparison to the FEM. Note that, in this example, due to the use of the Ramberg-Osgood hardening model (i.e., Eq. (2.41)), the stress-strain relation is rather complicated compared to the previous elastic-perfectly plastic model. Therefore, we conclude that our layer-based IGA frame model is capable of modeling the nonlinear inelastic response under cyclic loading circumstances very well.

2.5.3 Column Buckling

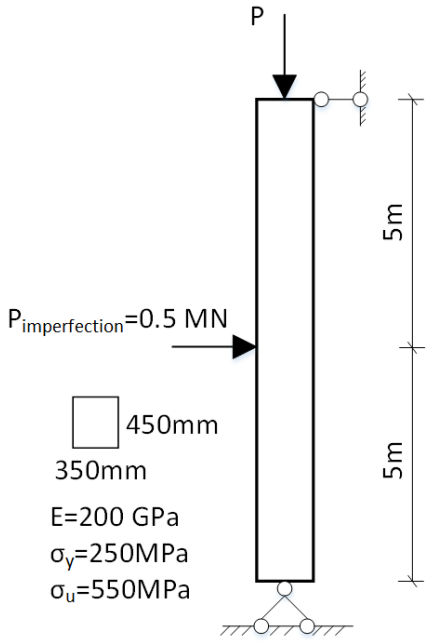

Figure 2-13: Dimensions of the inelastic column model

In this section, the column buckling problem (as illustrated in Fig. 2-13) was investigated to prove the effectiveness of the geometrically nonlinear formulation. An imperfection load was added laterally at the mid-span of the column. Both elastic and inelastic buckling were considered. The Ramberg-Osgood hardening model from the previous example was again adopted for the inelastic analysis. We observe from Fig. 2-14 that the results from layer-based IGA matched very well with solutions from Abaqus/Standard, both in the elastic buckling case and the inelastic buckling case.

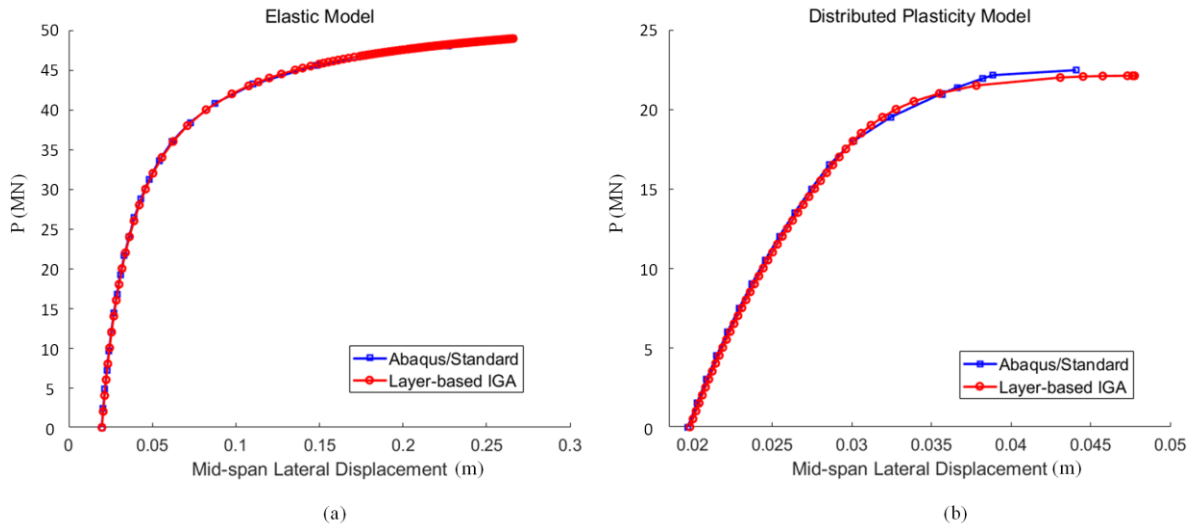

Figure 2-14: (a) Elastic buckling, and (b) inelastic buckling

In this verification case, the convergence rates among the standard FEM, layer-based IGA and adaptive IGA were studied. As illustrated in Fig. 2-15, due to the use of cubic B-spline basis functions, the layer-based IGA with uniform mesh reached a faster convergence rate than Abaqus/Standard while using fewer DOFs, whereas the adaptive IGA converged fastest among the three approaches with the fewest number of DOFs (28 DOFs in adaptive IGA, compared with 80 DOFs in layer-based IGA with uniform mesh and 603 DOFs in Abaqus/Standard). It is indicated here that the adaptive IGA approach is both accurate and efficient.

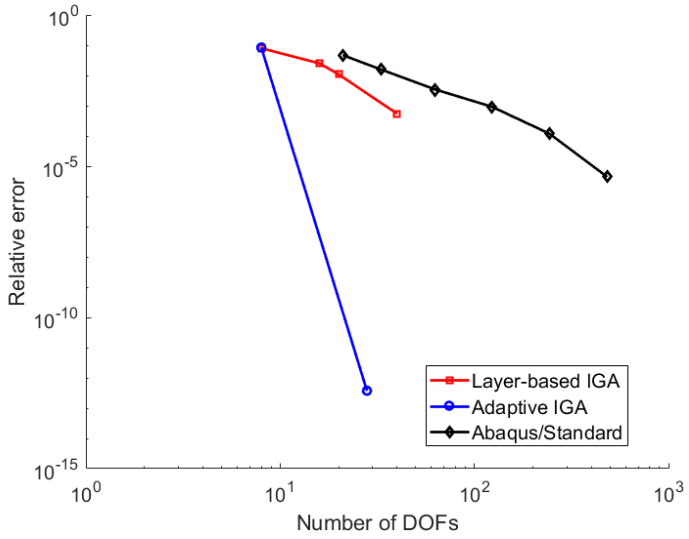

Figure 2-15: Convergence rates in the inelastic column buckling problem

2.5.4 Two-bay Two-story Frame

To demonstrate the performance of the proposed element in multi-patch analysis, a more complicated case is investigated in which rigid connections between members and geometrically nonlinear effects are considered. The beam has a cross-section of $450\text{mm} \times 200\text{mm}$, while the column's section is $450\text{mm} \times 350\text{mm}$. The members are oriented in such a way that their strong axes are used to bear the load. Material properties are the same as the first example. Detailed geometry and loading conditions can be found in Fig. 2-16.

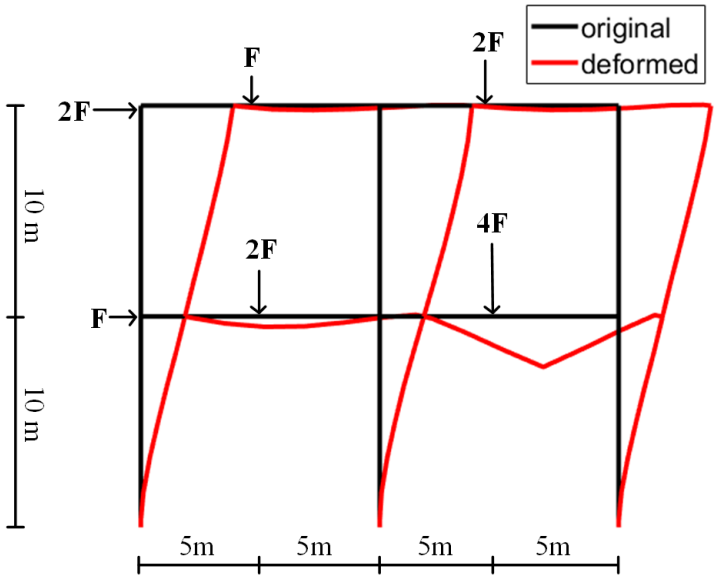

Figure 2-16: Frame geometry and deformed configuration at failure

It is observed from the deformed configuration in Fig. 2-16 that the beam in the first floor forms a mechanism due to the formation of plastic hinges at the mid-span and ends of the beam, while the columns maintain lateral stiffness. This is due to the fact that the beam has a smaller section in comparison to the column, causing a plastic hinge to form in the beam first. Thus, a soft-story mechanism is avoided.

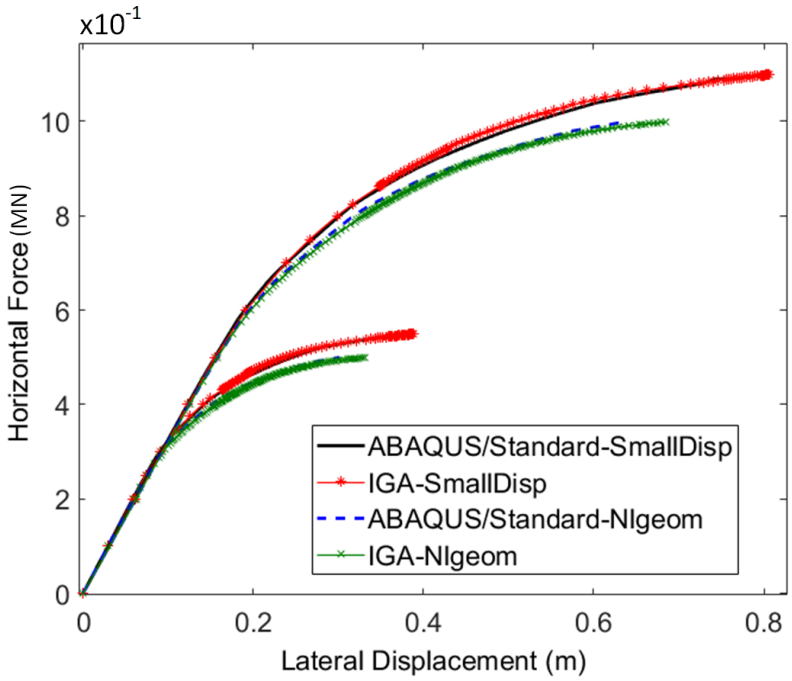

Figure 2-17: Load-lateral displacement curve for the first floor (ultimate load around $5x10^5$N) and second floor (ultimate load around $10x10^5$N)

Results from the IGA are compared with finite element simulations in ABAQUS/Standard. In Fig. 2-17, the horizontal load is plotted against lateral displacements from the ABAQUS/Standard finite element model and the proposed layer-based IGA model, considering both the small-deformation (i.e. geometrically linear, indicated using "SmallDisp") model and the large-deformation (geometrically nonlinear, indicated using "Nlgeom") model. It is observed that the response from multi-patch IGA model matches very well with that from ABAQUS/Standard. Thus, the approach for introducing constraint equations to simulate rigid connections is effective. The results also show a reduced stiffness in the geometrically nonlinear model, compared to the small deformation model due to the member-level geometrically nonlinear effects.

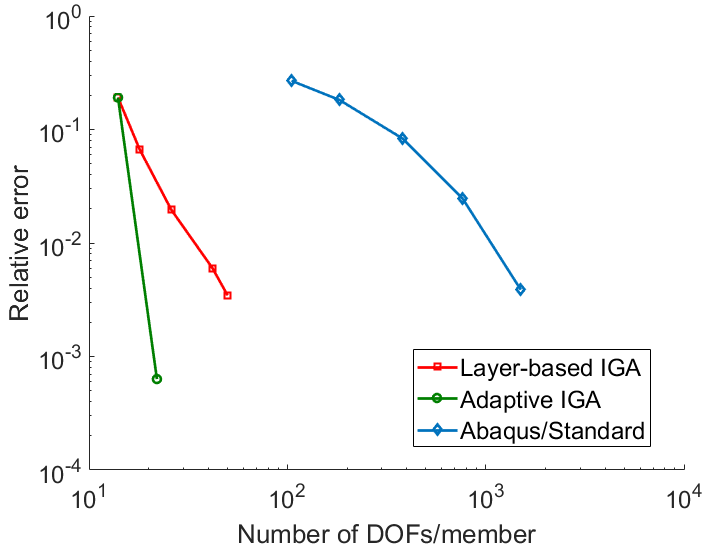

Figure 2-18: Error ratio vs. Number of DOFs

The relative error ratio is calculated using Eqn. (40), and results are plotted in Fig. 2-18. It is again illustrated that the layer-based isogeometric element leads to a faster convergence, compared to conventional finite element methods. It can also be seen that adaptive meshing provides a significant improvement over the non-adaptive IGA.

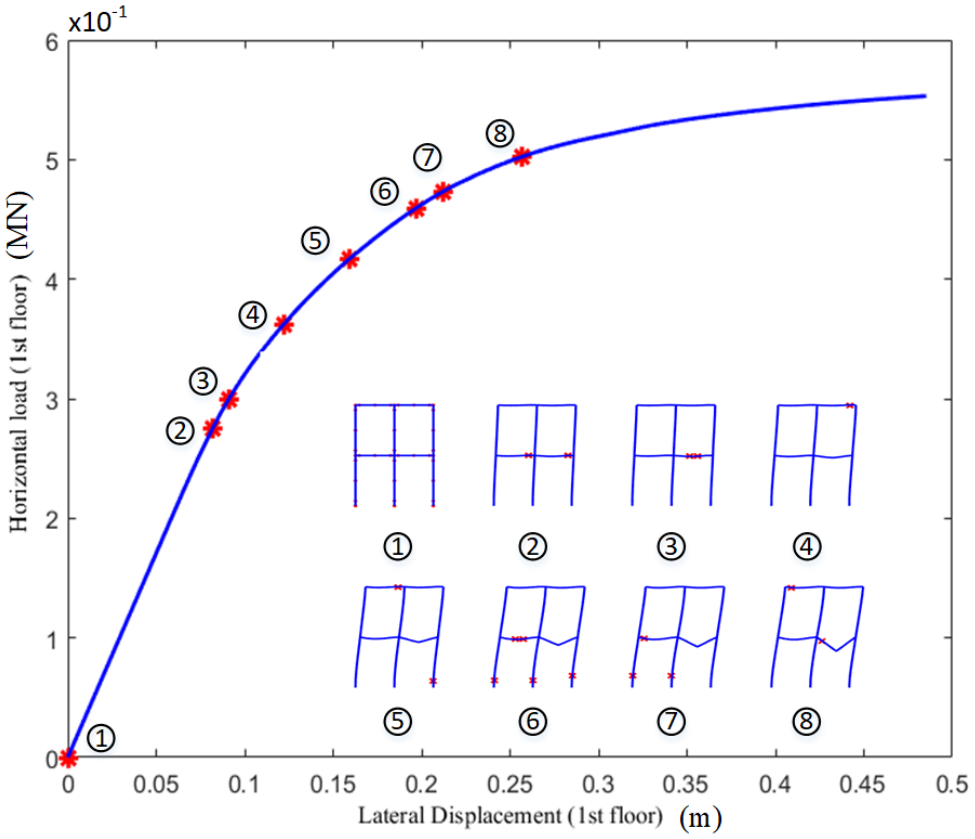

Figure 2-19: Adaptive meshing procedure

To give a better understanding of the adaptive meshing procedure in a more complicated system, Fig. 2-19 illustrates the adaptive knot-insertion process in the frame. Initial knot locations are plotted in the first configuration, while the remaining configurations (i.e., configurations 2 through 8) show the locations where yielding is detected and subsequently where knots are inserted. The model starts with a relatively coarse mesh, as shown in the first configuration. More knots are inserted to refine the mesh as the members yield. Note that the knots near the ends of the member aim to define the boundary conditions/additional constraints and therefore are located sufficiently close to the ends.

2.6 Conclusion

A 2D distributed plasticity isogeometric model utilizing a layer discretization was formulated.

The member-level geometrically nonlinear effects were included through the inclusion of high-order strain terms. The formulation however is presently limited to problems with moderate displacements. The model was extended to multi-patch analysis through the introduction of continuity constraints between two adjacent patches, allowing for the rigid connection of members in a frame. The model closely represents reality as plastic hinges form in the beams or columns rather than at a fictitious joint region, which is rather important from a structural point of view. The formulation was also presented for adaptive analysis. Lobatto quadrature was employed in order to capture the onset of yielding at the ends of the member, and a knot insertion technique was introduced to capture the change in curvature associated with the formation of a plastic hinge. The procedure is completely automatic in that the evolution of structural deformation is fully governed by yielding, which can be accurately captured through knot insertion and thus no user intervention is required. Several verification cases involving the yielding of beams and frames under monotonic and cyclic loading were considered. It was observed that our layer-based IGA model required substantially fewer degrees of freedom to achieve similar levels of accuracy compared to the conventional finite element method. The reduction in degrees of freedom is due to the elimination of the rotational degrees of freedom and the high accuracy associated with the NURBS basis functions. The savings could significantly improve the computational cost of analyzing the inelastic response of large-scale structural systems subjected to extreme loads.

Chapter 3 Isogeometric Analysis of Laminated Composite and Functionally Graded Sandwich Plates Based on a Layerwise Displacement Theory

A multi-layered shell formulation is developed based on a layerwise deformation theory [56] within the framework of isogeometric analysis (IGA). IGA utilizes Non-Uniform Rational B-splines (NURBS) to represent the geometry as well as to describe the field variables [1], thus it offers the great opportunity of directly importing CAD designs into finite element analysis without converting the geometry. In this way, the gap between design and analysis is bridged. The derivation also follows a layerwise theory, which assumes a separate displacement field expansion within each layer, and considers transverse displacement component as C^0-continuous at layer interfaces, thus resulting in a layerwise continuous transverse strain states. Since the in-plane and through-thickness integrations are carried out individually, this approach is capable of capturing the complete three-dimensional stress states in a two-dimensional setting, which improves the computational efficiency. A knot insertion technique is utilized for the discretization in the through-thickness direction, and C^0-continuity is enforced by means of knot repetition at dissimilar material interfaces. The performance of the proposed model is demonstrated using multiple laminated composites and sandwich plates (including functionally graded material core) as examples. Numerical results prove the accuracy of the proposed formulation and show that the isogeometric layerwise shell is superior to its finite element counterpart.

3.1 Introduction

Laminated composites are increasingly used in industries such as civil engineering, automotive engineering, manufacturing and aerospace engineering. This rapid popularization in

application is mainly owing to their characteristically high strength-to-weight ratio. Functionally graded material (FGM) as a special type of composite material is a mixture of two or more distinct materials (usually ceramic on top and metal at the bottom) with the volume fraction varying through one direction. It was first proposed by Bever and Duwez [57] and is well-known to provide high performance and multiple functions. Another appealing feature of FGM is that its material properties vary continuously in the thickness direction, in contrast to the traditional laminated composites where discontinuity exists at layer interfaces. However, the failure modes of laminated composites can be extremely complex, mainly because the majority of the dominated failure occurs in the inner layers of the composites and thus they are not easily detected a priori. Therefore, understanding how stresses and deformations distribute in the inner layers is of vital importance in determining why, how and under what loads structural failure will occur.

In order to understand and characterize the deformation and stress distribution, a number of theories have been developed for the analysis of multi-layered composite plates. The most propagated theoretical work for laminate composite structures is the classical laminate plate theory (CLPT) [56], in which it is assumed the state of stress is in-plane and in a layerwise fashion in addition to Kirchhoff's classical plate theory. This theory, however, is two-dimensional and therefore cannot predict the out-of-plane stress state. In three-dimensional domain, perhaps the most dominant theories in the field of composite laminates are the equivalent-single-layer (ESL) theory and layerwise theories. Among the ESL-based theories, first-order shear deformation theory (FSDT) [58–60] and higher-order shear deformation theory (HSDT) [61–63] are frequently used. The essence of ESL is that it replaces a heterogeneous laminated plate/shell with a statically equivalent single layer whose stiffness is a weighted average of the individual layer stiffness [64]. Although ESL is relatively simple and reduces the actual three-dimensional problem into a two-

dimensional one, it incorrectly assumes that the transverse strain components are continuous across the ply interface between dissimilar materials and thus results in a discontinuity in transverse stress components at the ply interfaces. In contrast to the ESL theories, the layerwise theories assume a separate displacement field expansion in the layer level, and consider transverse displacement component as C^0-continuous at layer interfaces, thus resulting in a layerwise continuous transverse strain states [64–66]. Therefore, layerwise theories provide a better understanding of the complete three-dimensional stress state.

Functionally graded material is a type of inhomogeneous, multi-phase composite material with material properties changing continuously in one direction due to the gradual variation of volume fraction of its constituent materials. A significant amount of research [67–71] has been done recently to better understand the behavior of FGM and FGM-incorporated materials. Jha et al. [72] gave an excellent review of the recent research on functionally graded plates. A generalized shear deformation theory was developed by Zenkour [73], in which a correct representation of the transverse shear term was adopted and therefore no shear correction factor was required. Neves et al. [74] investigated the static, free vibration and buckling behavior of sandwich plates with a functionally graded material core based on a higher-order shear deformation theory and a collocation method with radial basis functions. The thickness stretching effect in FGM was evaluated through removing/keeping the transverse normal term in the kinematics assumption of multiple plate theories [75]. Reddy and Kim [67] presented a nonlinear third-order plate theory for the analysis of FGM. This method was based on a modified couple stress theory that included a material length scale parameter to account for the size effect in FGM.

Within this context, the proposed research aims at applying isogeometric analysis and a layerwise deformation theory to model multi-layered laminated composites and functionally

graded sandwich plates. IGA was first proposed by Hughes et al. [1] and has been widely applied to the field of structural and solid mechanics. It essentially utilizes the same basis function to represent the geometry as well as to describe the field variables so it bridges the gap between computer-aided design (CAD) and analysis. The high-order smoothness associated with NURBS basis functions allows the prediction of highly accurate stress fields, which in turn reduces the required mesh size and results in great savings in computational efforts. Moreover, the knot insertion technique in IGA eases the difficulty in enforcing C^0 continuity at layer interfaces. A number of studies has been done over the past a few years on laminated composite [25–27,76] and FGM sandwich plates [28,29,77–82] in the framework of IGA and showed that IGA offered high accuracy and significant computational savings. However, the majority of them rely on theories that are based on ESL theory (such as FSDT and HSDT) and that involve both displacement and rotational degrees of freedom (DOFs). Few studies have applied displacement-based layerwise theories to study the behavior of laminated composites with significantly different material properties between different layers or with material properties varying drastically through the thickness direction (e.g., FGM). The novelty of the present research beyond existing work lies in the fact that a layerwise theory in which all DOFs are displacement-based (i.e., rotation-free) is implemented in an isogeometric setting and C^0 continuity is enforced at ease by knot repetition. The proposed approach is also successfully applied to study laminated composites embedding a FGM core and gives satisfactory results.

3.2 A Brief Overview of Isogeometric Analysis

The fundamentals of IGA are stated in this section based on Hughes's work [1]. In one dimension, the parametric space is discretized by a knot vector, which is a non-decreasing set of coordinates and is defined as follows:

$$\Xi = \{\xi_1, \xi_2, ..., \xi_{n+p+1}\},\ \xi_i \le \xi_{i+1},\ i=1,...,n+p \tag{3.1}$$

where ξ_i is the i^{th} knot, n is the number of basis functions and p denotes the polynomial order. By repeating the first and last knots p times, the knot vector becomes an open one and the endpoints are interpolatory. The basis function is C^{∞} continuous inside a knot span and is C^{p-m} continuous at a knot location, where m is the multiplicity of the knot.

Given a knot vector, the corresponding B-spline basis functions are defined based on the Cox-de Boor recursion formula. For p=0,

$$N_{i,0}(\xi) = \begin{cases} 1 & \xi_i < \xi < \xi_{i+1} \\ 0 & otherwise \end{cases} \tag{3.2}$$

For p=1, 2, 3, …

$$N_{i,p}(\xi) = \frac{\xi - \xi_i}{\xi_{i+p} - \xi_i} N_{i,p-1}(\xi) + \frac{\xi_{i+p+1} - \xi}{\xi_{i+p+1} - \xi_{i+1}} N_{i+1,p-1}(\xi) \tag{3.3}$$

The B-spline curve is then constructed as,

$$C(\xi) = \sum_{i=1}^{n} N_{i,p}(\xi) P_i \tag{3.4}$$

where P_i is the i^{th} control point.

In two dimensions, the B-spline surface is defined by a tensor product of univariate B-spline basis functions in the following way,

$$S(\xi, \eta) = \sum_{i=1}^{n} N_{i,p}(\xi) M_{j,q}(\xi) P_{i,j} \tag{3.5}$$

where $N_{i,p}(\xi)$ and $M_{j,q}(\xi)$ denote the B-spline basis functions defined by the knot vector $\Xi = \{\xi_1, \xi_2, ..., \xi_{n+p+1}\}$ and $\mathrm{H} = \{\eta_1, \eta_2, ..., \eta_{m+q+1}\}$, respectively.

By projecting a B-spline entity from R^d to R^{d+1} using the weights associated with corresponding control points, the non-uniform rational B-splines (NURBS) are constructed,

$$R_i^p(\xi) = \frac{N_{i,p}(\xi) w_i}{\sum_{j=1}^{n} N_{j,p}(\xi) w_j} \tag{3.6}$$

where the denominator $\sum_{j=1}^{n} N_{j,p}(\xi) w_j$ is the weighting function.

The NURBS surface can then be defined by,

$$S(\xi, \eta) = \sum_{i=1}^{n} \sum_{j=1}^{m} R_{i,j}^{p,q}(\xi, \eta) P_{i,j} \tag{3.7}$$

where $R_{i,j}^{p,q}(\xi, \eta)$ is the multiplication of univariate NURBS, $R_{i,j}^{p,q}(\xi, \eta) = \frac{N_{i,p}(\xi) M_{j,q}(\eta) w_{i,j}}{\sum_{k=1}^{n} \sum_{l=1}^{m} N_{k,p}(\xi) M_{l,q}(\eta) w_{k,l}}$. An example of the cubic NURBS surface is shown in Fig. 3-1. The control points and the control polygon are illustrated in black and in red, respectively. The control points are only interpolatory at the vertices of the surface and are otherwise not interpolatory, as is also indicated by the fact that the control points in general do not lie on the surface.

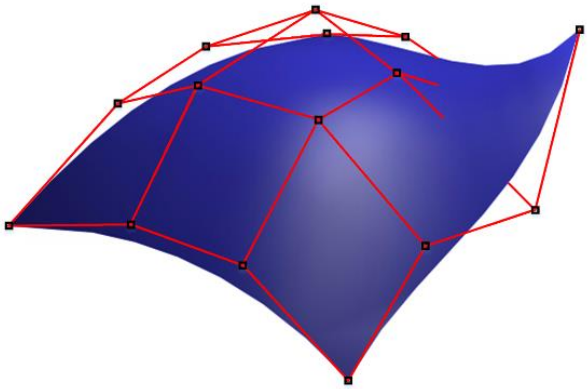

Figure 3-1: NURBS surface and control lattice

3.3 Isogeometric Layerwise Formulation

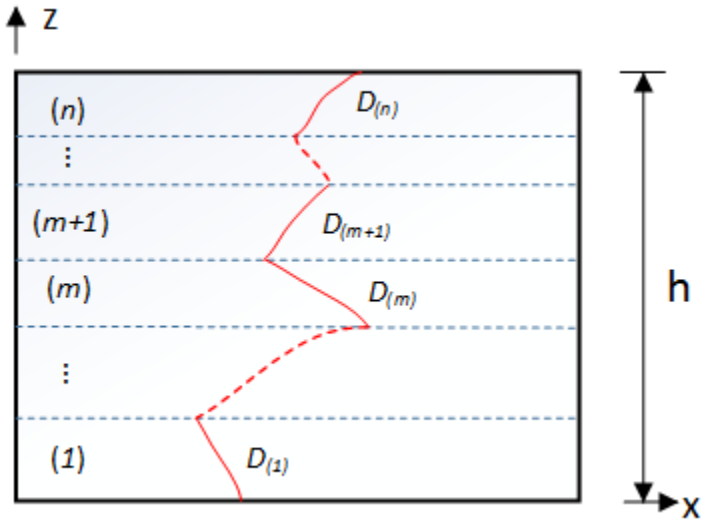

Figure 3-2: Layerwise kinematics

In our work, we adopt Reddy's layerwise displacement theory [56] to formulate the isogeometric layerwise plate for the analysis of laminated composite and sandwich plates with a FGM core. In this theory, separate displacement field expansion from each layers is considered and the transverse displacement component is assumed to be C^0 continuous at layer interfaces (see Fig. 3-2). The in-plane space is discretized by multiplication of univariate NURBS basis function

(see Fig. 3-3), while in the through-thickness direction, a B-spline basis function is utilized and C^0 continuity at the layer interface is enforced through repetition of knots.

3.3.1 Layerwise Kinematics

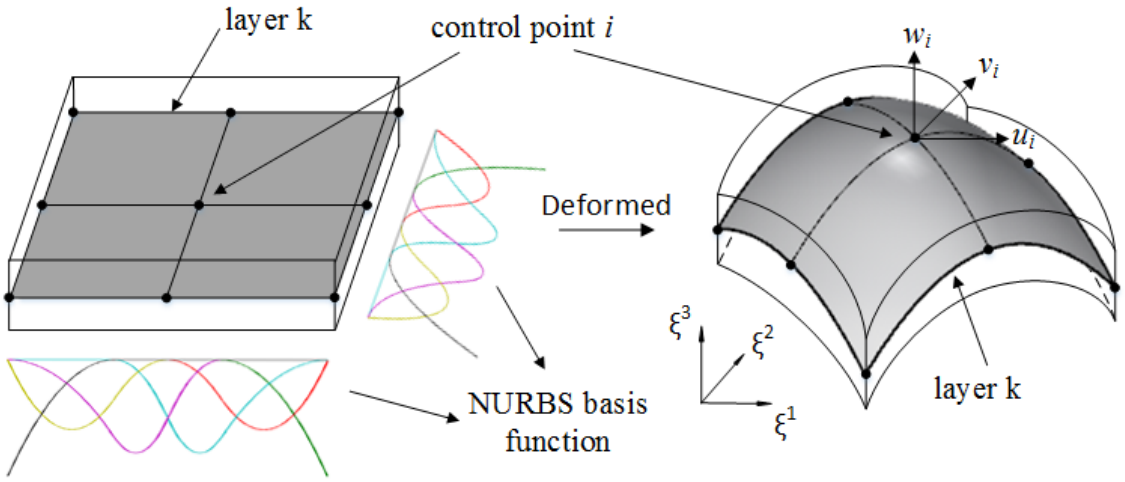

Figure 3-3: In-plane discretization of kth layer and element DOFs illustration

Based on Reddy's layerwise theory, the displacements at any point of the laminated composite can be expanded as:

$$u(x,y,z)=\sum_{i=1}^{Ncp} u_i(x,y)N^i(z)$$

$$v(x,y,z)=\sum_{i=1}^{Ncp} v_i(x,y)N^i(z) \tag{3.8}$$

$$w(x,y,z)=\sum_{i=1}^{Ncp} w_i(x,y)N^i(z)$$

where Ncp denotes the number of control points in the thickness direction, (u_i, v_i, w_i) is the displacements at control point i (also see Fig. 3-3), and $N^i(z)$ is the B-spline basis function for

the discretization of the through-thickness displacements, whereas in Reddy's work, Lagrange polynomial shape function is used.

As in Reddy's formulation, the von Karman strain-displacement relations are adopted to account for geometric nonlinearity,

$$\varepsilon_{xx} = \frac{\partial u}{\partial x} + \frac{1}{2}\frac{\partial^2 w}{\partial x^2},\ \varepsilon_{yy} = \frac{\partial v}{\partial y} + \frac{1}{2}\frac{\partial^2 w}{\partial y^2}$$

$$\varepsilon_{zz} = \frac{\partial w}{\partial z},\ \varepsilon_{yz} = \frac{\partial v}{\partial z} + \frac{\partial w}{\partial y} \tag{3.9}$$

$$\varepsilon_{xz} = \frac{\partial u}{\partial z} + \frac{\partial w}{\partial x},\ \varepsilon_{xy} = \frac{\partial u}{\partial y} + \frac{\partial v}{\partial x} + \frac{\partial w}{\partial x}\frac{\partial w}{\partial y}$$

The stresses in layer *k* can then be derived based on Hooke's law. For an orthotropic layer *k*,

$$\begin{Bmatrix} \sigma_{xx} \\ \sigma_{yy} \\ \sigma_{zz} \\ \sigma_{yz} \\ \sigma_{xz} \\ \sigma_{xy} \end{Bmatrix}^{(k)} = \begin{bmatrix} \overline{Q}_{11} & \overline{Q}_{12} & \overline{Q}_{13} & 0 & 0 & \overline{Q}_{16} \\ \overline{Q}_{12} & \overline{Q}_{22} & \overline{Q}_{23} & 0 & 0 & \overline{Q}_{26} \\ \overline{Q}_{13} & \overline{Q}_{23} & \overline{Q}_{33} & 0 & 0 & \overline{Q}_{36} \\ 0 & 0 & 0 & \overline{Q}_{44} & \overline{Q}_{45} & 0 \\ 0 & 0 & 0 & \overline{Q}_{45} & \overline{Q}_{55} & 0 \\ \overline{Q}_{16} & \overline{Q}_{26} & \overline{Q}_{36} & 0 & 0 & \overline{Q}_{66} \end{bmatrix}^{(k)} \begin{Bmatrix} \varepsilon_{xx} \\ \varepsilon_{yy} \\ \varepsilon_{zz} \\ \varepsilon_{yz} \\ \varepsilon_{xz} \\ \varepsilon_{xy} \end{Bmatrix}^{(k)} \tag{3.10}$$

where $\overline{Q}_{ij}$ denotes the transformed material coefficients from the material coordinates to the global coordinates. For details of the transformation matrix, see [56].

3.3.2 Virtual Work

Following Reddy's formulation, the method of virtual work is invoked to derive the stiffness matrix in the element level. Based on Hamilton's principle, the variation in internal potential energy and external virtual work should be zero, i.e.,

$$\delta\Pi = \delta U + \delta V = 0 \tag{3.11}$$

The variation of the internal potential energy of the laminate can be expressed in terms of stress and strain,

$$\delta U = \int_A \int_z \left(\sigma_{xx}\delta\varepsilon_{xx} + \sigma_{yy}\delta\varepsilon_{yy} + \sigma_{zz}\delta\varepsilon_{zz} + \sigma_{yz}\delta\varepsilon_{yz} + \sigma_{xz}\delta\varepsilon_{xz} + \sigma_{xy}\delta\varepsilon_{xy} \right) dz dA \tag{3.12}$$

Substitution of the strain-displacement equations from Eq. (9) and stress-strain relation from Eq. (10) gives the weak form of the variation of the internal potential energy. By rearranging and separating the u_i, v_i and w_i terms, we obtain the following,

δu_i :

$$\int_A \left(\frac{\partial \delta u_i}{\partial x} \left[A_{11}^{ij} \frac{\partial u_j}{\partial x} + \frac{1}{2} D_{11}^{ijk} \frac{\partial w_j}{\partial x} \frac{\partial w_k}{\partial x} + A_{12}^{ij} \frac{\partial v_j}{\partial y} + \frac{1}{2} D_{12}^{ijk} \frac{\partial w_j}{\partial y} \frac{\partial w_k}{\partial y} + \overline{A}_{13}^{ij} w_j \right] + \frac{\partial \delta u_i}{\partial y} \left[A_{66}^{ij} \left(\frac{\partial u_j}{\partial y} + \frac{\partial v_j}{\partial x} \right) + D_{66}^{ijk} \frac{\partial w_j}{\partial x} \frac{\partial w_k}{\partial y} \right] + \delta u_i \left(\tilde{A}_{55}^{ij} u_j + \overline{A}_{55}^{ji} \frac{\partial w_j}{\partial x} \right) \right) dx dy \tag{3.13a}$$

δv_i :

$$\int_A \left(\frac{\partial \delta v_i}{\partial y} \left[A_{12}^{ij} \frac{\partial u_j}{\partial x} + \frac{1}{2} D_{12}^{ijk} \frac{\partial w_j}{\partial x} \frac{\partial w_k}{\partial x} + A_{22}^{ij} \frac{\partial v_j}{\partial y} + \frac{1}{2} D_{22}^{ijk} \frac{\partial w_j}{\partial y} \frac{\partial w_k}{\partial y} + \overline{A}_{23}^{ij} w_j \right] + \frac{\partial \delta v_i}{\partial x} \left[A_{66}^{ij} \left(\frac{\partial u_j}{\partial y} + \frac{\partial v_j}{\partial x} \right) + D_{66}^{ijk} \frac{\partial w_j}{\partial x} \frac{\partial w_k}{\partial y} \right] + \delta v_i \left(\tilde{A}_{44}^{ij} v_j + \overline{A}_{44}^{ji} \frac{\partial w_j}{\partial y} \right) \right) dx dy \tag{3.13b}$$

δw_i :

$$\int_A \Bigg(\delta w_i \left[\overline{A}_{13}^{ji} \frac{\partial u_j}{\partial x} + \frac{1}{2} \overline{D}_{13}^{jki} \frac{\partial w_j}{\partial x} \frac{\partial w_k}{\partial x} + \overline{A}_{23}^{ji} \frac{\partial v_j}{\partial y} + \frac{1}{2} \overline{D}_{23}^{jki} \frac{\partial w_j}{\partial y} \frac{\partial w_k}{\partial x} + \tilde{A}_{33}^{ij} w_j \right]$$
$$+ \frac{\partial \delta w_i}{\partial x} \left(\overline{A}_{55}^{ij} u_j + A_{55}^{ji} \frac{\partial w_j}{\partial x} \right) + \frac{\partial \delta w_i}{\partial y} \left(\overline{A}_{44}^{ij} v_j + A_{44}^{ji} \frac{\partial w_j}{\partial y} \right)$$
$$+ \frac{\partial \delta w_i}{\partial x} \frac{\partial w_j}{\partial x} \left(D_{11}^{ijk} \frac{\partial u_k}{\partial x} + \frac{1}{2} F_{11}^{ijkl} \frac{\partial w_k}{\partial x} \frac{\partial w_l}{\partial x} + D_{12}^{ijk} \frac{\partial v_k}{\partial y} + \frac{1}{2} F_{12}^{ijkl} \frac{\partial w_k}{\partial y} \frac{\partial w_l}{\partial y} + \overline{D}_{13}^{ijk} w_k \right)$$
$$+ \frac{\partial \delta w_i}{\partial y} \frac{\partial w_j}{\partial y} \left(D_{12}^{ijk} \frac{\partial u_k}{\partial x} + \frac{1}{2} F_{12}^{ijkl} \frac{\partial w_k}{\partial x} \frac{\partial w_l}{\partial x} + D_{22}^{ijk} \frac{\partial v_k}{\partial y} + \frac{1}{2} F_{22}^{ijkl} \frac{\partial w_k}{\partial y} \frac{\partial w_l}{\partial y} + \overline{D}_{23}^{ijk} w_k \right)$$
$$+ \left(\frac{\partial \delta w_i}{\partial x} \frac{\partial w_j}{\partial y} + \frac{\partial \delta w_i}{\partial y} \frac{\partial w_j}{\partial x} \right) \left[D_{66}^{ijk} \left(\frac{\partial u_k}{\partial y} + \frac{\partial v_k}{\partial x} \right) + F_{66}^{ijkl} \frac{\partial w_k}{\partial x} \frac{\partial w_l}{\partial y} \right] \Bigg) dxdy \tag{3.13c}$$

where the through-thickness laminate stiffnesses are integrated separately from the in-plane integration. These stiffnesses are given as follows,

$$A_{mn}^{ij} = \int_{-\frac{h}{2}}^{\frac{h}{2}} \overline{Q}_{mn} N^i N^j dz \,,\ \overline{A}_{mn}^{ij} = \int_{-\frac{h}{2}}^{\frac{h}{2}} \overline{Q}_{mn} N^i \frac{dN^j}{dz} dz$$

$$\tilde{A}_{mn}^{ij} = \int_{-\frac{h}{2}}^{\frac{h}{2}} \overline{Q}_{mn} \frac{dN^i}{dz} \frac{dN^j}{dz} dz \,,\ D_{mn}^{ijk} = \int_{-\frac{h}{2}}^{\frac{h}{2}} \overline{Q}_{mn} N^i N^j N^k dz \tag{3.14}$$

$$\overline{D}_{mn}^{ijk} = \int_{-\frac{h}{2}}^{\frac{h}{2}} \overline{Q}_{mn} N^i N^j \frac{dN^k}{dz} dz \,,\ F_{mn}^{ijkl} = \int_{-\frac{h}{2}}^{\frac{h}{2}} \overline{Q}_{mn} N^i N^j N^k N^l dz$$

The stiffness equations in Eqs. (13)-(14) are identical to those presented by Reddy, with the difference that B-spline basis functions are used in place of the Lagrange polynomial shape functions in the original FE formulation. Nodes are replaced by control points, which usually provide basis functions that have control over multiple elements. Note that since the through-thickness integration and in-plane integration are carried out separately, the layerwise model is

able to capture the full three-dimensional stress state while maintaining a two-dimensional data structure, which leads to significant savings in computational efforts.

3.3.3 Enforcement of C^0 Continuity at Layer Interfaces

Layerwise theories assume the transverse displacement as C^0-continuous at layer interfaces. Recall that a B-spline is C^{p-m} continuous at a knot, where p is the polynomial order and m is the multiplicity of the knot. In this context, C^0-continuity at dissimilar material interfaces can be implemented readily by repeating the knots at the layer interface p-1 times [27] so that the multiplicity of the knot becomes p. This further ensures that the continuity at the current knot is $C^{p-p=0}$. An example of C^0 enforcement is shown in Fig. 3-4. The B-spline is initially linear at (a), and is raised up to order 2 and 3 by p-refinement at (b) and (c), respectively. Through inserting a knot at $\xi_i = 0.5$, the plate is discretized into two through-thickness elements at (d). By subsequently repeating it two times, a layer interface with C^0-continuity is generated in the middle of the ply at (e).

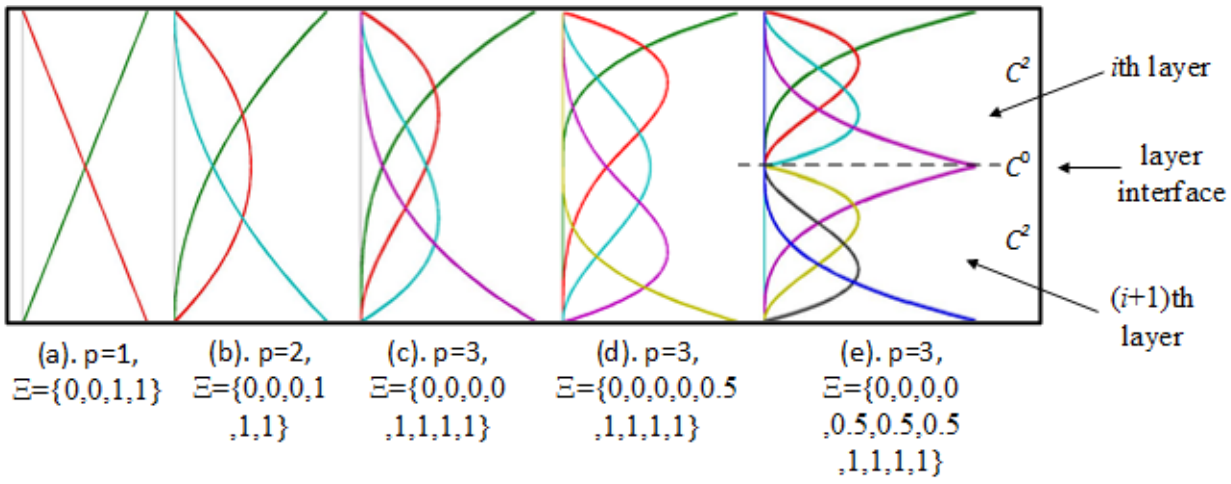

Figure 3-4: C^0 interface continuity enforced by knot insertion

3.4 Numerical Verifications

In this section, multiple examples of laminated composite and sandwich plates including a FGM core are analyzed to demonstrate the performance of the proposed model. For all the cases, p+1 Gauss integration points are used to ensure accuracy.

3.4.1 [0º/90º/0º] Square Plate Subjected to Double Sinusoidal Load

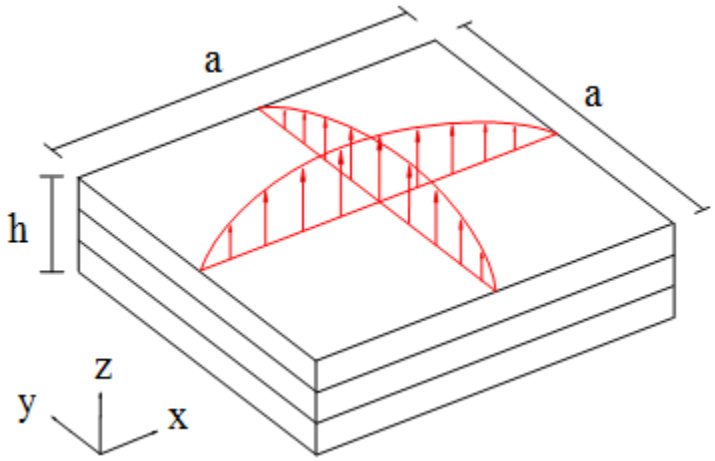

Figure 3-5: Illustration of a square plate under double sinusoidal load

The classical three-layer square plate subjected to double sinusoidal load (see Fig. 3-5) is tested here to assess the proposed model in predicting the complete three-dimensional stress states. A 3D analytical solution [83] is available as reference solution to verify the obtained stress results. A number of researchers [84,85] have also studied this problem based on layerwise finite element methods. The stacking sequence is [0º/90º/0º] and the three layers are of equal thickness. The span-to-thickness ratio is a/h=4. The plate is simply supported at the four edges and is implemented as:

$$\sigma_x = v = w = 0, \text{ at } x = 0, a$$

$$\sigma_y = u = w = 0, \text{ at } y = 0, a$$

The double-sinusoidal pressure is loaded at the top surface of the laminate and is defined as,

$$q = q_0 \sin\left(\frac{\pi x}{a}\right)\sin\left(\frac{\pi y}{b}\right) \tag{3.15}$$

The material properties of the laminate are defined as,

$$E_2 = E_3 = 1.0\times10^6 \text{psi},\ E_1 = 25E_2$$

$$G_{12} = G_{13} = 5.0\times10^5 \text{psi},\ G_{23} = 2.0\times10^5 \text{psi}$$

$$\nu_{12} = \nu_{23} = \nu_{13} = 0.25$$

The non-dimensional stresses [83] are given as follows,

$$\bar{\sigma}_{11} = \frac{\sigma_{11}\left(x_1, x_1, z\right)}{q_0 S^2},\ \bar{\sigma}_{33} = \frac{\sigma_{33}\left(x_1, x_1, z\right)}{q_0}$$

$$\bar{\sigma}_{13} = \frac{\sigma_{13}\left(x_2, x_1, z\right)}{q_0 S},\ \bar{\sigma}_{23} = \frac{\sigma_{23}\left(x_1, x_2, z\right)}{q_0 S} \tag{3.16}$$

$$x_1 = 1.105662\frac{a}{2},\ x_2 = 1.894338\frac{a}{2},\ S = \frac{a}{h}$$

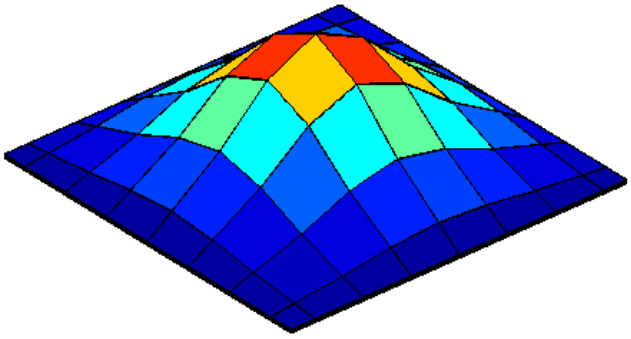

Figure 3-6: Deformed configuration of the square plate under double sinusoidal load

The deformed configuration is plotted in Fig. 3-6. The black lines on the plate indicate the control mesh created from control points, whereas a uniform physical mesh can be created using uniformly spaced knots. The obtained stress results were compared to the 3D analytical solution [83], as illustrated in Fig. 3-7. As we can observe, the proposed model with cubic NURBS basis functions (8x8 in-plane control points) gave an excellent agreement with the exact solution, with barely noticeable discrepancies at layer interfaces. The use of quartic NURBS (9x9 in-plane control points) immediately fixed the non-physical discontinuities at dissimilar material interfaces. Worth mentioning is that, as opposed to the finite element models in the literature that use relatively fine meshes (15x15 points in [61] and 11x11 points in [85]), the mesh we adopted (in-plane discretization: 8x8 control points) is very coarse.

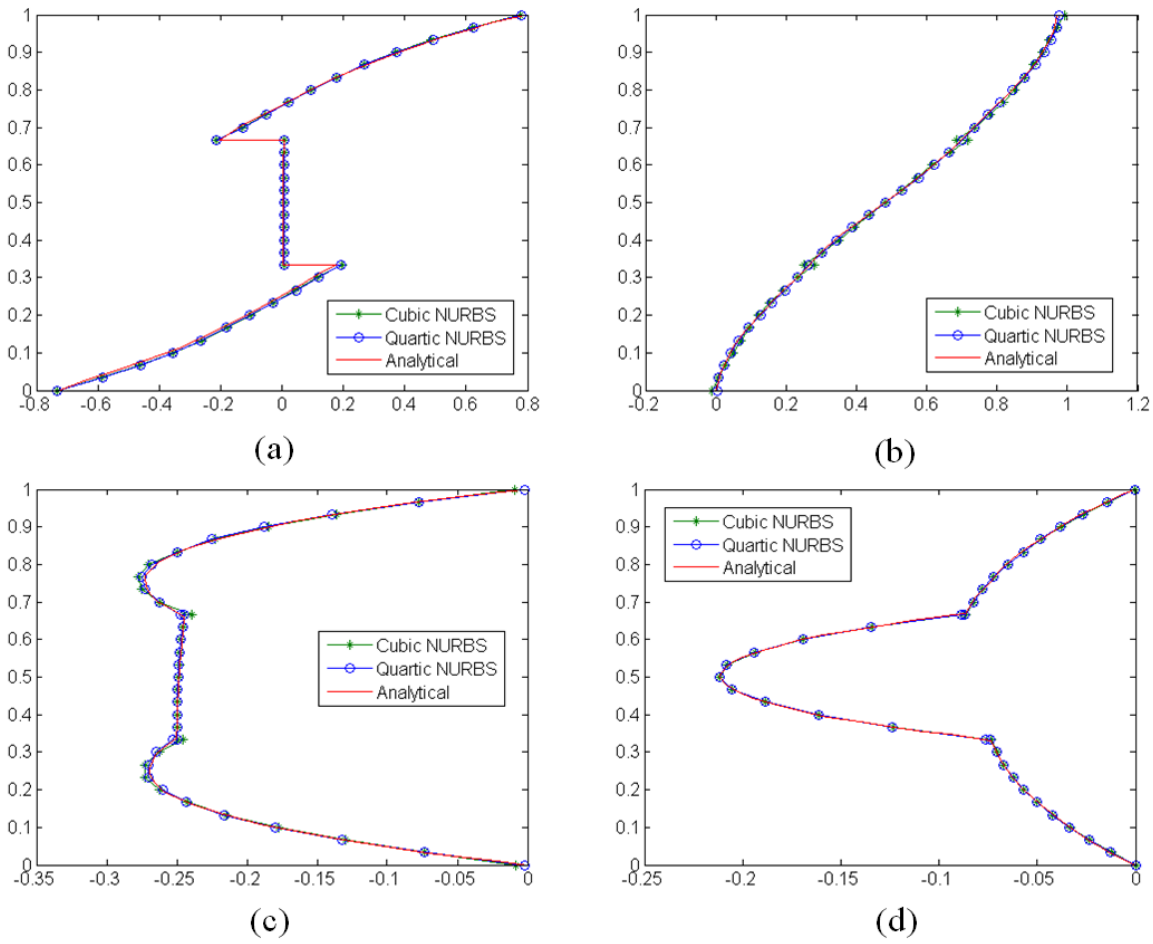

Figure 3-7: Normalized through-thickness stress distribution of the [0º/90º/0º] square plate: (a) $\overline{\sigma}_{11}$, (b) $\overline{\sigma}_{33}$, (c) $\overline{\sigma}_{13}$,(d) $\overline{\sigma}_{23}$.

3.4.2 [0º/core/0º] Sandwich Plate under Uniform Pressure

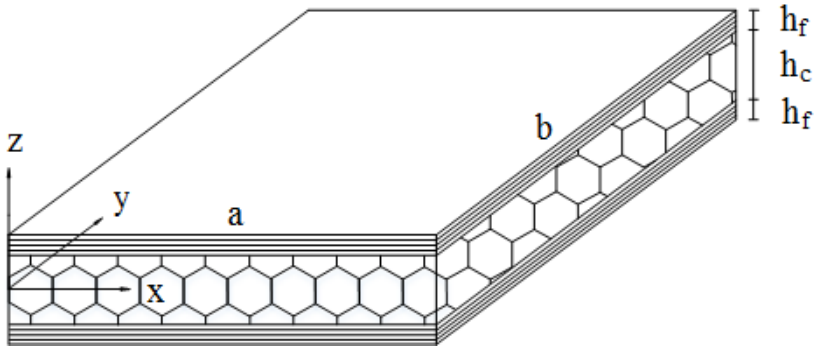

Figure 3-8: Illustration of a sandwich plate

In this example, a three-layer, simply supported, square sandwich plate (as shown in Fig. 3-8) is studied under uniform pressure to test the performance of the isogeometric layerwise formulation in terms of displacement and three-dimensional stress states. Sandwich plate as a special case of laminated composites is investigated by a number of researchers [25,26,86] because the core of the plate is very soft as compared to the outside face sheets. A 3D analytical solution from [87] is used as the reference solution, in which the through-thickness deformation w is assumed to be constant and the surface-wise deformation u and v are independent of the thickness variable z. In the numerical implementation, the $\overline{Q}_{33}$ term in the material matrix is set to be 10^4 so that the through-thickness deformation being a constant is enforced, and the rest of the terms on the third row and column are set to be zero to make u and v deformation independent of z. It is checked that ill-conditioning does not occur, as is also proved by the results obtained later. The uniform transverse pressure p is loaded on the top surface of the plate. The span-to-thickness ratio a/h is 10. The core thickness to plate thickness ratio h_f/h is 0.8.

Due to symmetry, only a quarter of the sandwich plate is modeled. The anisotropic stress-strain relationship of the core is defined as,

$$\overline{Q}_{core} = \begin{bmatrix} 0.999781 & 0.231192 & 0 & 0 & 0 & 0 \\ 0.231192 & 0.524886 & 0 & 0 & 0 & 0 \\ 0 & 0 & 10^4 & 0 & 0 & 0 \\ 0 & 0 & 0 & 0.266810 & 0 & 0 \\ 0 & 0 & 0 & 0 & 0.159914 & 0 \\ 0 & 0 & 0 & 0 & 0 & 0.262931 \end{bmatrix} \tag{3.17}$$

And the material properties of the two face sheets are calculated as,

$$\overline{Q}_{face} = R\overline{Q}_{core} \tag{3.18}$$

where R is a factor that relates the face sheet material property with the core material property. The normalization of the displacement and stresses of the sandwich plate [87] are defined as follows,

$$\bar{w} = \frac{0.999781 w(\frac{a}{2},\frac{a}{2},0)}{hp},\ \bar{\sigma}_x^1 = \frac{\sigma_{xx}^3(\frac{a}{2},\frac{a}{2},\frac{h}{2})}{p}$$

$$\bar{\sigma}_x^2 = \frac{\sigma_{xx}^3(\frac{a}{2},\frac{a}{2},\frac{2h}{5})}{p},\ \bar{\sigma}_x^3 = \frac{\sigma_{xx}^2(\frac{a}{2},\frac{a}{2},\frac{2h}{5})}{p} \tag{3.19}$$

$$\bar{\sigma}_y^1 = \frac{\sigma_{yy}^3(\frac{a}{2},\frac{a}{2},\frac{h}{2})}{p},\ \bar{\sigma}_y^2 = \frac{\sigma_{yy}^3(\frac{a}{2},\frac{a}{2},\frac{2h}{5})}{p},\ \bar{\sigma}_y^3 = \frac{\sigma_{yy}^2(\frac{a}{2},\frac{a}{2},\frac{2h}{5})}{p}$$

$$\bar{\sigma}_{xz} = \frac{\sigma_{xz}(0,\frac{a}{2})}{p},\ \bar{\sigma}_{yz} = \frac{\sigma_{yz}(\frac{a}{2},0)}{p}$$

where the superscript j of $\bar{\sigma}_{ii}^j$ indicates the layer where the stress is evaluated.

Table 3-1: Convergence of the normalized displacement and stresses (R=5)

NURBS	Normalized	Meshes				
		3x3	5x5	17x17	19x19	21x21
Quadratic	$\bar{w}$	258.960	258.944	258.947	258.947	258.947
		(0.004%)	(0.010%)	(0.009%)	(0.009%)	(0.009%)
Cubic		259.235	259.238	259.237	259.237	259.237
		(0.102%)	(0.103%)	(0.103%)	(0.103%)	(0.103%)
Quartic		259.239	259.237	259.234	259.234	259.233
		(0.104%)	(0.103%)	(0.102%)	(0.102%)	(0.102%)
Exact		-	-	-	-	258.97

Quadratic	$\overline{\sigma}_x^1$	60.937	60.514	60.297	60.293	60.290
		(0.968%)	(0.267%)	(0.093%)	(0.099%)	(0.104%)
Cubic		60.338	60.334	60.340	60.340	60.340
		(0.025%)	(0.031%)	(0.022%)	(0.022%)	(0.022%)
Quartic		60.350	60.333	60.339	60.339	60.339
		(0.005%)	(0.033%)	(0.023%)	(0.023%)	(0.023%)
Exact		-	-	-	-	60.353
Quadratic	$\overline{\sigma}_y^1$	38.860	38.619	38.518	38.517	38.516
		(0.959%)	(0.333%)	(0.070%)	(0.068%)	(0.065%)
Cubic		38.537	38.551	38.551	38.550	38.550
		(0.120%)	(0.156%)	(0.156%)	(0.153%)	(0.153%)
Quartic		38.570	38.548	38.550	38.550	38.550
		(0.205%)	(0.148%)	(0.153%)	(0.153%)	(0.153%)
Exact		-	-	-	-	38.491

Firstly, the convergence of the model was studied using the *R*=5 case. The normalized deflection and stresses were shown in Table 3-1. The relative error between the obtained solution and the exact one is shown in the parenthesis. As we can observe, the proposed model was able to provide a very accurate solution in deflection and stresses with a very coarse mesh (mesh case: 3x3). To get as close to the exact solution as possible, several fine meshes were studied and the results were in excellent agreement with the exact solution. Furthermore, various *R* values representing the difference between the face sheets and the core were investigated. The results were compared with solutions obtained from literature and are listed in Table 3-2. Again, the results from our proposed model matched very well with the exact solution regardless of the value for *R*. The use of HSDT in [88] and [61] was able to catch fairly good deflection and stresses with relatively small R, but resulted in relatively large errors when R became large. Similar issue was

reported when Grover et al. [89] presented their application of an inverse hyperbolic shear deformation theory and Mantari et al. [90] used a trigonometric shear deformation theory for the analysis of sandwich plates. Ferreira [91] adopted a layerwise theory to study the sandwich plate and gave very accurate results, but we were able to achieve a better accuracy with the use of NURBS basis functions. Thai et al. [26] used a similar approach that utilized FSDT in each layer and imposed displacement continuity at layer interfaces. This led to solutions of similar accuracy compared to our proposed model, but their model was computationally more expensive since rotational DOFs in the x-z and y-z planes were required in each layer. Therefore, by comparison of our solution with the ones found in the literature, it was concluded that our proposed approach outperformed its finite element counterpart. The through-thickness distribution of the stresses was plotted in Fig. 3-9.

Table 3-2: The normalized displacement and stresses of a square sandwich plate under a uniform load

R	Method	$\overline{w}$	$\overline{\sigma}_x^1$	$\overline{\sigma}_x^2$	$\overline{\sigma}_x^3$	$\overline{\sigma}_y^1$	$\overline{\sigma}_y^2$	$\overline{\sigma}_y^3$
5	Pandya-HSDT [88]	256.130 (1.097%)	62.380 (3.359%)	46.910	9.382	38.930	30.330	6.065
	Ferreira-HSDT [61]	257.110 (0.718%)	60.366 (0.022%)	47.003	9.401	38.456	30.242	6.048
	Ferreira-LW [91]	257.523 (0.559%)	59.968 (0.638%)	46.291	9.258	38.321	29.974	5.995
	Grover-IHSDT [89]	255.644 (1.284%)	60.675 (0.534%)	47.055	9.411	38.522	30.206	6.041
	Mantari-TriSDT [90]	256.706 (0.874%)	60.525 (0.285%)	47.061	9.412	38.452	30.177	6.035
	Thai-LW [26]	258.835 (0.052%)	60.254 (0.164%)	46.510	9.302	38.495	30.109	6.022
	Present-Quadratic	258.947 (0.009%)	60.290 (0.104%)	46.539	9.308	38.516	30.126	6.025
	Present-Cubic	259.237 (0.103%)	60.340 (0.022%)	46.579	9.316	38.550	30.154	6.031
	Present-Quartic	259.233 (0.102%)	60.339 (0.023%)	46.579	9.316	38.550	30.153	6.031

	Exact	258.97	60.353	46.623	9.34	38.491	30.097	6.161
10	Pandya-HSDT [88]	152.330 (4.423%)	64.650 (1.044%)	51.310	5.131	42.830	33.970	3.397
	Ferreira-HSDT [61]	154.658 (2.963%)	65.381 (0.075%)	49.973	4.997	43.240	33.637	3.364
	Ferreira-LW [91]	158.380 (0.627%)	64.846 (0.744%)	48.443	4.844	43.390	33.306	3.924
	Grover-IHSDT [89]	154.550 (3.030%)	65.741 (0.626%)	49.798	4.979	43.400	33.556	3.356
	Mantari-TriSDT [90]	155.498 (2.436%)	65.542 (0.321%)	49.708	4.971	43.385	33.591	3.359
	Thai-LW [26]	159.406 (0.016%)	65.230 (0.156%)	48.733	4.873	43.649	33.501	3.350
	Present-Quadratic	159.472 (0.058%)	65.271 (0.093%)	48.766	4.877	43.673	33.520	3.352
	Present-Cubic	159.555 (0.110%)	65.296 (0.055%)	48.786	4.879	43.690	33.534	3.353
	Present-Quartic	159.552 (0.108%)	65.295 (0.057%)	48.785	4.879	43.690	33.533	3.353
	Exact	159.38	65.332	48.857	4.903	43.566	33.413	3.500
15	Pandya-HSDT [88]	110.430 (9.275%)	66.620 (0.250%)	51.970	3.465	44.920	35.410	2.361
	Ferreira-HSDT [61]	114.644 (5.813%)	66.919 (0.198%)	50.323	3.355	45.623	35.167	2.345
	Ferreira-LW [91]	120.988 (0.601%)	66.291 (0.743%)	47.899	3.193	46.292	34.890	2.326
	Grover-IHSDT [89]	115.820 (4.847%)	67.272 (0.726%)	49.813	3.321	45.967	35.088	2.339
	Mantari-TriSDT [90]	115.919 (4.766%)	67.185 (0.596%)	49.769	3.318	45.910	35.081	2.339
	Thai-LW [26]	121.776 (0.046%)	66.679 (0.162%)	48.167	3.211	46.546	35.080	2.339
	Present-Quadratic	121.823 (0.085%)	66.722 (0.097%)	48.202	3.214	46.571	35.100	2.340
	Present-Cubic	121.860 (0.115%)	66.736 (0.076%)	48.212	3.214	46.581	35.107	2.341
	Present-Quartic	121.857 (0.113%)	66.735 (0.078%)	48.211	3.214	46.580	35.107	2.340
	Exact	121.720	66.787	48.299	3.238	46.424	34.955	2.494

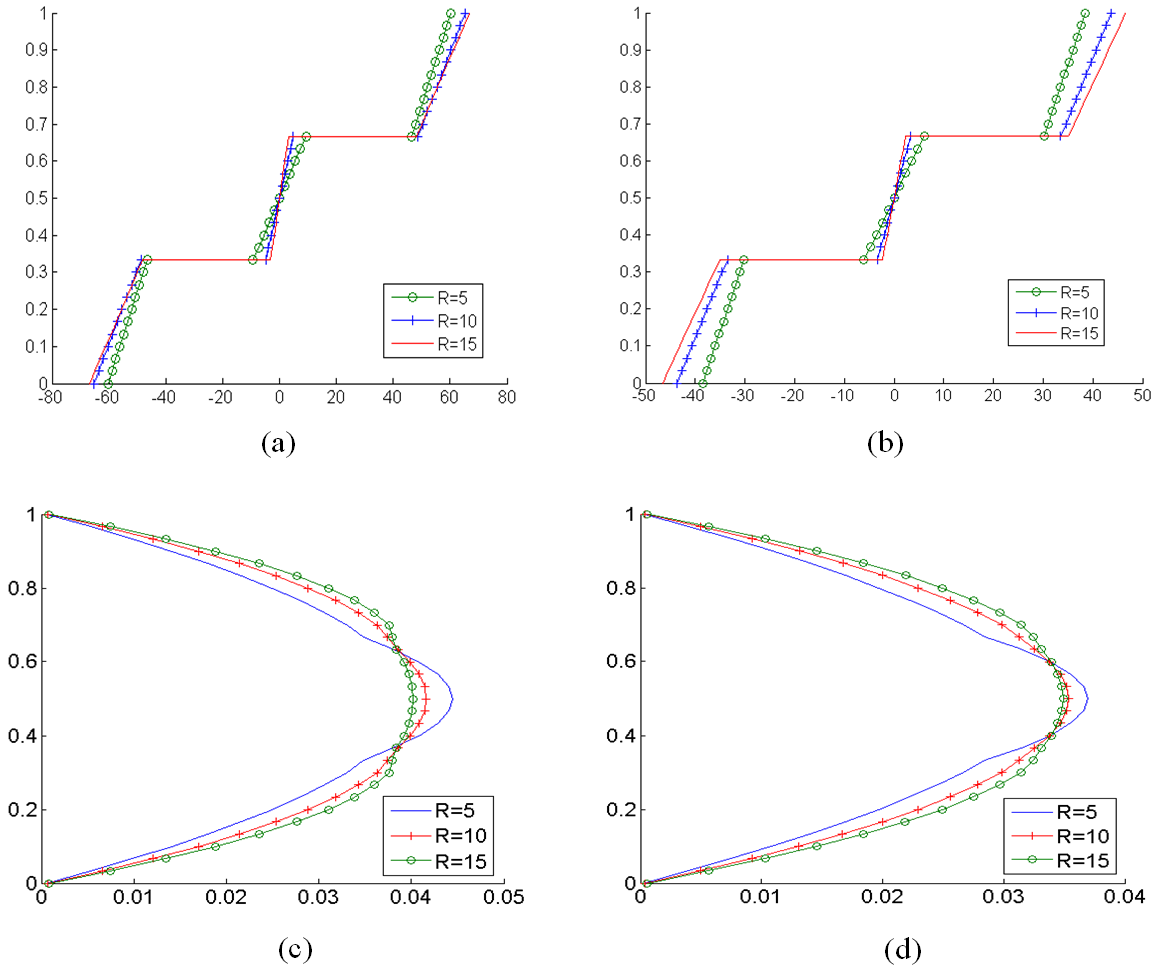

Figure 3-9: Normalized through-thickness stress distribution of the sandwich plate: (a) $\overline{\sigma}_{xx}$,(b) $\overline{\sigma}_{yy}$, (c) $\overline{\sigma}_{xz}$, (d) $\overline{\sigma}_{yz}$.

3.4.3 Sandwich Plate with a FGM Core

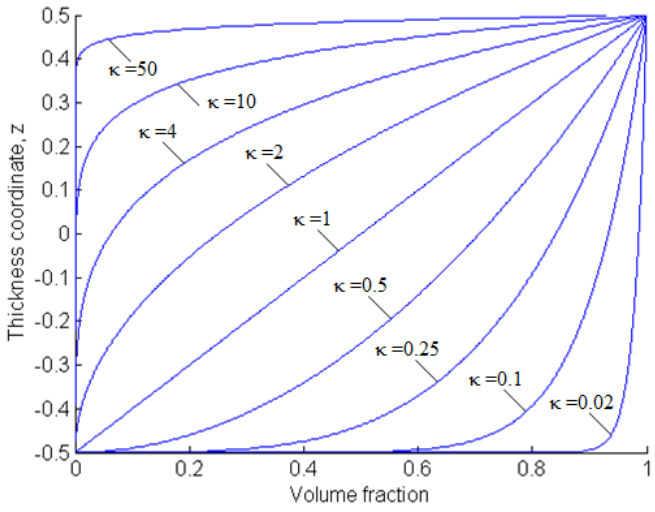

Figure 3-10: Illustration of the volume fraction through the thickness with varying power-law exponent

For the case of a square plate with a FGM core, the material of the core is graded gradually from ceramic on top to metal at the bottom with the volume fraction varying through the thickness direction. The volume fraction of the ceramic used in this paper follows the power-law distribution function [75]:

$$V_c(z)=\left(\frac{2z+h_c}{2h_c}\right)^{\kappa},-\frac{h_c}{2}\le z\le\frac{h_c}{2} \tag{3.20}$$

The effective Young's modulus of a FGM is then computed based on the following:

$$E(z)=E_m+(E_c-E_m)V_c(z) \tag{3.21}$$

where E_m and E_c are the Young's modulus of the metal and ceramic, respectively, h_c is the height of the layer, z is the thickness coordinate, and κ denotes the volume fraction exponent defining the gradation of material properties. Fig. 3-10 illustrates the through-thickness variation

of the volume fraction with different power-law exponents, which shows that the volume fraction changes drastically with very large/small power-law exponents. This paper is focused on the part where $\kappa \geq 1$.

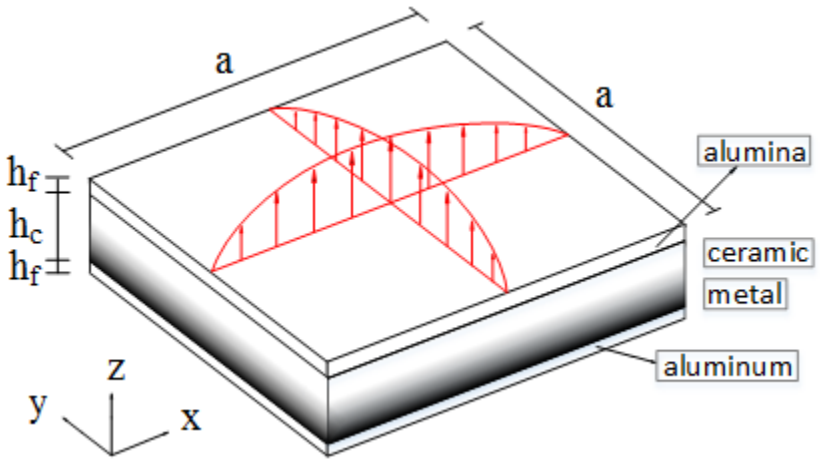

Figure 3-11: Illustration of a sandwich plate with a FGM core

As illustrated in Fig. 3-11, a simply supported, square sandwich plate ($a = 1m$) with a FGM core subjected to double sinusoidal load is taken as an example. Several studies [74,75,92,93] are available to compare in terms of the accuracy of the proposed model. The double sinusoidal pressure follows the Eq. (15). The height of each face sheet is $0.1h$. The top and bottom face sheets are isotropic and are in alumina ($E_c = 380GPa$) and aluminum ($E_m = 70GPa$), respectively. The power-law function that defines the Young's modulus in FGM follows Eq. (20) and Eq. (21). The Poisson's ratio is chosen to be 0.3. We investigate a number of cases in which the span-to-thickness ratio a/h is equal to 4, 10 and 100, and the exponential κ is equal to 1, 4 and 10, respectively.

The displacement and stresses are defined in normalized form [74] as follows,

$$\bar{w} = \frac{10h^3 E_c}{a^4 q_0} w\left(\frac{a}{2}, \frac{a}{2}\right), \quad \bar{\sigma}_{xx} = \frac{h}{a q_0} \sigma_{xx}\left(\frac{a}{2}, \frac{a}{2}\right)$$

$$\bar{\sigma}_{yy} = \frac{h}{aq_0}\sigma_{yy}\left(\frac{a}{2},\frac{a}{2}\right),\ \bar{\sigma}_{zz} = \frac{1}{q_0}\sigma_{zz}\left(\frac{a}{2},\frac{a}{2}\right) \tag{3.22}$$

$$\bar{\sigma}_{xy} = \frac{h}{aq_0}\sigma_{xy}(0,0),\ \bar{\sigma}_{xz} = \frac{h}{aq_0}\sigma_{xz}\left(0,\frac{a}{2}\right),\ \bar{\sigma}_{yz} = \frac{h}{aq_0}\sigma_{yz}\left(\frac{a}{2},0\right)$$

The normalized deflection $\bar{w}$ and transverse stress $\bar{\sigma}_{xz}$ obtained from the proposed model along with results from the literature are listed in Table 3-3. Quartic NURBS basis functions were adopted. In general, a $5\times5\times3$ mesh yielded satisfactory results. In order to get a converged solution, knot insertion was performed in the FGM core, resulting in five through-thickness elements in the core while retaining the one-element discretization in the face sheets. Similar solutions were reported in the literature [74,75,92,93]. Neves et al. [74,92] adopted a quasi-3D HSDT and sinusoidal shear deformation theory to investigate the behavior of the sandwich FGM plate. Carrera et al. [75] used the Carrera's Unified Formulation (CUF) to study the effect of thickness stretching in FGM plate. However, they generally required a very fine mesh of grid, as presented in [74,92] where a 19x19 grid was used to reach convergence. On the contrary, our proposed model adopted an in-plane discretization of 8x8 control points, which was significantly less than the number of nodes used in the literature. We conclude that our solutions are very close to the results in the literature and that the isogeometric layerwise model is efficient in discretizing the in-plane space.

Table 3-3: The normalized displacement and stresses of a square sandwich plate with FGM core ($\varepsilon_{zz} \neq 0$)

κ	$\bar{\sigma}_{xz}(h/6)$			$\bar{w}(0)$		
a/h	4	10	100	4	10	100

1	Brischetto [93]	0.2613	0.2605	0.2603	0.7628	0.6324	0.6072
	Carrera [75]	0.2604	0.2594	0.2593	0.7628	0.6324	0.6072
	Neves [92]	0.2742	0.2788	0.2793	0.7416	0.6305	0.6092
	Neves [74]	0.2745	0.2789	0.2795	0.7417	0.6305	0.6092
	Present (5x5x3)	0.2613	0.2605	0.2538	0.7686	0.6338	0.6073
	Present (5x5x7)	0.2613	0.2604	0.2497	0.7642	0.6327	0.6073
4	Brischetto [93]	0.2429	0.2431	0.2432	1.0934	0.8321	0.7797
	Carrera [75]	0.2400	0.2398	0.2398	1.0930	0.8307	0.7797
	Neves [92]	0.2723	0.2778	0.2785	1.0391	0.8202	0.7784
	Neves [74]	0.2696	0.2747	0.2753	1.0371	0.8199	0.7784
	Present (5x5x3)	0.2429	0.2430	0.2389	1.0988	0.8325	0.7798
	Present (5x5x7)	0.2401	0.2401	0.2354	1.0948	0.8312	0.7797
10	Brischetto [93]	0.2150	0.2174	0.2179	1.2232	0.8753	0.8077
	Carrera [75]	0.1932	0.1944	0.1946	1.2172	0.8740	0.8077
	Neves [92]	0.2016	0.2059	0.2064	1.1780	0.8650	0.8050
	Neves [74]	0.1995	0.2034	0.2039	1.1752	0.8645	0.8050
	Present (5x5x3)	0.2202	0.2228	0.2212	1.2181	0.8772	0.8079
	Present (5x5x7)	0.2246	0.2277	0.2260	1.2244	0.8755	0.8077

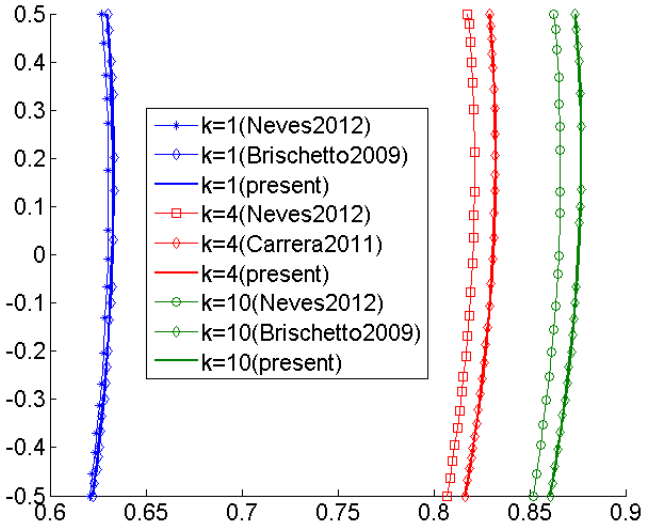

Figure 3-12: Normalized through-thickness displacement at the center of the plate

The through-thickness data of the normalized displacement $\overline{w}$, in-plane stresses $\overline{\sigma}_{xx}$ and $\overline{\sigma}_{xy}$, through-thickness normal stress $\overline{\sigma}_{zz}$ and through-thickness shear stress $\overline{\sigma}_{xz}$ were plotted in Fig. 3-12 to 3-14 along with the results from the literature [74,75,92,93]. As we can see, the solutions of the normalized displacement $\overline{w}$ provided by Brischetto [93] and Carrera [75] matched perfectly with our results, but the solution of Neves [92] lacked accuracy when κ became large. In terms of the stresses, all the solutions seemed to do a good job in predicting the in-plane stresses. However, non-physical jumps in transverse normal stress $\overline{\sigma}_{zz}$ and transverse shear stress $\overline{\sigma}_{xz}$ were observed in Brischetto's results [93]. It is logical to say that the normalized transverse normal stress $\overline{\sigma}_{zz}$ should be zero at the bottom of the sandwich plate and equal to one on top, since the double-sinusoidal load was added at the top surface, which was proved by the solution of Brischetto [93] and our results. However, the transverse normal stress $\overline{\sigma}_{zz}$ by Neves [92] and

Carrera [75] didn't seem to obey this assumption. Therefore, we conclude that our solutions in both displacement and stresses are more accurate.

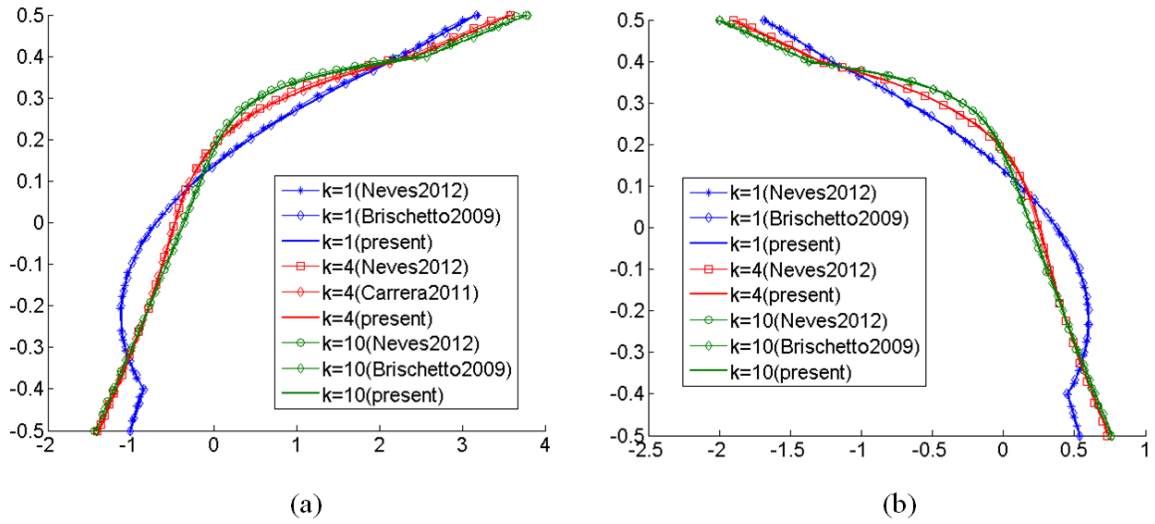

Figure 3-13: Normalized through-thickness stress distribution of the sandwich plate embedding a FGM core: (a) $\overline{\sigma}_{xx}$, (b) $\overline{\sigma}_{xy}$.

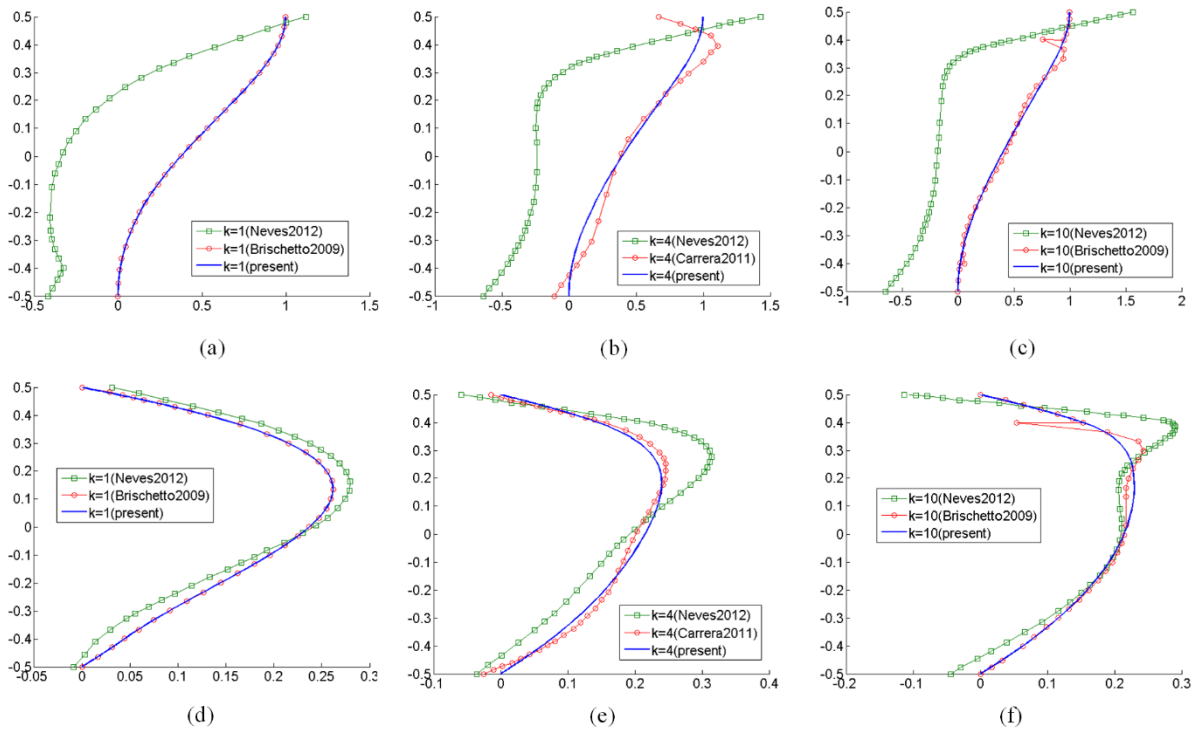

Figure 3-14: Normalized through-thickness stress distribution of the sandwich plate embedding a FGM core: (a)-(c) $\overline{\sigma}_{zz}$, (d)-(f) $\overline{\sigma}_{xz}$.

3.5 Conclusion

An isogeometric layerwise model was developed for the analysis of laminated composite and sandwich plates embedding a FGM core. The proposed model assumed a separate displacement field expansion within each layer and used the knot insertion technique to enforce the C^0-continuity at layer interfaces. Due to the fact that the through-thickness integration were carried out separately from the in-plane surface integration, the proposed model was able to capture the full three-dimensional stress states while maintaining a two-dimensional data structure, which significantly saved computational efforts. Multiple laminated composite and sandwich plate (including a FGM core) examples were tested based on the proposed isogeometric layerwise model. Results were verified against both 3D exact solution and results from the literature and

showed high accuracy of the present method. As compared to the existing finite element models, relative coarse meshes were used in the proposed method to get results of similar level of accuracy owing to the high-order smoothness of NURBS basis functions. Better accuracy in predicting the transverse stresses were also observed using the proposed method. The use of NURBS basis functions also removed the non-physical jumps in transverse stresses in layer interfaces. Therefore, we conclude that the proposed isogeometric layerwise model was superior in predicting the full 3D stress states of laminated composites over existing approaches. Nevertheless, situations that commonly occurs in laminated composites such as delamination are not considered in the current model. Future work includes enabling the proposed formulation to capture the full 3D stress states of delaminated composite laminates.

Chapter 4 A Geometrically Exact Isogeometric Kirchhoff Plate: Feature-preserving Automatic Meshing and C^1 Rational Triangular Bézier Spline Discretization

The analysis of the Kirchhoff plate is performed using rational Bézier triangles in isogeometric analysis (IGA) coupled with a feature-preserving automatic meshing algorithm. IGA employs the same basis function for geometric design as well as for numerical analysis. The proposed approach also features an automatic meshing algorithm that admits localized geometric features (e.g., small geometric details, sharp corners) with high resolution. Moreover, the use of rational triangular Bézier splines for domain triangulation significantly increases the flexibility in discretizing spaces bounded by complicated NURBS curves. To raise the global continuity to C^1 for the solution of the plate bending problem, Lagrange multipliers are leveraged to impose continuity constraints. The proposed approach also manipulates the control points at domain boundaries in such a way that the geometry is exactly described. A number of numerical examples consisting of static bending and free vibration analysis of thin plates bounded by complicated NURBS curves are used to demonstrate the advantage of the proposed approach.

4.1 Introduction

Numerical modeling and analysis of plates of complicated shapes has continuously been a popular research topic because of the widespread applications of plate structures in various fields. Finite element analysis (FEA) of plates can be categorized into thin plate analysis based on the Kirchhoff plate theory and thick plate analysis based on the Reissner-Mindlin plate theory. The main difference between the two prevailing theories lies in the fact that thin plate analysis assumes that the vector normal to the plate mid-surface remains normal to the mid-surface during

deformation and thus does not take into account transverse shear deformations, whereas thick plate analysis does. Due to the fact that Reissner-Mindlin plate elements can be joined with C^0 continuity, the use of very simple basis functions is allowed. On the contrary, in the Kirchhoff plate formulation, because of the presence of second-order derivatives, C^1 continuity is demanded between elements which requires higher order basis functions. For this reason, the C^0 shear deformable Reissner-Mindlin plate element is more propagated in commercial finite element codes. However, most of the plate structures in reality belong to thin and very thin plates, and the use of C^0 basis functions would usually result in various shear locking problems.

Although the numerical analysis of thin plates is already a very mature field, to exactly describe the plate geometry can be rather difficult and sometimes inaccurate, particularly when the structures have curved boundaries or complicated cutouts are involved. The main reason for this lack of accuracy lies in the fact that the model created from standard FEA, which is represented by Lagrange basis functions, is only an approximation of the original computer-aided design (CAD) model, which is described by Non-Uniform Rational B-spines (NURBS). About a decade ago, isogeometric analysis (IGA) was proposed by Hughes et al. [1] as a novel approach to bridge the gap between design and analysis. By employing the same basis functions used in geometric design to approximate field variables in an isoparametric sense, the models created using IGA possess geometric exactness. Other appealing features of IGA include high-order continuity of basis functions, which further leads to more stable numerical conditioning, faster convergence of solutions, and so on. NURBS-based IGA has since been applied to the analysis of thin and thick plates ([3,47,94–98], to name a few).

Nevertheless, NURBS functions, which are the main tool for IGA, exhibit a number of defects. First of all, NURBS *h*-refinement propagates across the entire domain, which compromises the

efficiency of the method. Secondly, the control mesh generated is restricted to a quadrilateral shape and is therefore not flexible in discretizing domains of arbitrary topology. Moreover, the smoothness in multi-patch analysis using NURBS is not satisfactory. The patch interface is either C^0-continuous or simply not closed (i.e., non-physical gaps). To regain control of the smoothness across the patch boundaries, additional efforts such as the imposition of geometric constraints [2] or the bending strip method [11] are necessary, which requires extra computational time. On the other hand, a variety of local refinement techniques have been developed to overcome the problematic tensor-product structure of NURBS, such as hierarchical B-splines [12,99], truncated hierarchical B-splines (THB-splines) [100], T-splines [13], locally refined splines [101] and polynomial splines over hierarchical T-meshes [15]. However, the construction of the aforementioned local refinement splines relies on complicated algorithms and the resulting mesh is still dependent on the four-sided geometry. On the contrary, the use of spline basis functions for domain triangulation increases the flexibility in discretizing complex spaces. One way to realize this is to use certain triangle-splitting algorithms such as the Powell-Sabin splines [20,102,103] and the Clough-Tocher splines [104], depending on particular macro-triangle structures. Higher-order Powell-Sabin splines are also available to triangulate a given space [102,105,106]. However, for a given space for triangulation, the Powell-Sabin triangles are sometimes not unique [107]. Recently, NURBS have been successfully converted to the non-uniform rational Powell-Sabin splines (NURPS) [108]. To exactly recover the boundary NURBS curve of degree p, NURPS of degree p or higher should be used. For the recovery of the interior domain described by NURBS of bi-degree (p1, p2), NURPS of degree p1+p2 or higher should be used. Powell-Sabin B-splines have been applied to study Kirchhoff-Love plate problems [109] and fracture mechanics [110] with satisfactory results.

An alternative is to construct the domain triangulation through the use of rational Bézier triangles [111]. This approach is more general and does not depend on specific triangle-splitting schemes. Since rational basis functions of the Bézier-Bernstein form are used to represent the parametric space, it has the potential to describe the exact geometry as well. In our work, the C^0 rational Bézier triangles are employed for the representation of the triangulated space. Since the Kirchhoff plate formulation involves second-order derivatives of the basis function, at least C^1 continuity is required. For this reason, the global continuity of the triangular Bézier splines is raised to C^1. Note that the approach we adopted can be used to elevate the splines to any desired continuity C^r. Lagrange multipliers are used to impose the Dirichlet boundary conditions and the continuity constraints. Considering that the use of Lagrange multipliers results in an increase of unknowns in the system equations, which hinders efficiency, an iterative approach for the solution of the Lagrange multiplier augmented system is provided as well.

As to the parameterization of the boundary and interior space of the model, we leverage on the recently developed algorithm TriGA [21]. Specifically, a polygonal approximation of the NURBS boundary is first established through *h*-refinement and a dynamic quadtree decomposition algorithm. This procedure allows us to capture sharp geometric features with very good accuracy. With the polygonal approximation of the original NURBS curves computed, a linear domain triangulation can then be constructed by resorting to the meshing package mesh2d [112] that is available online. After that, the linear triangular elements are raised to cubic such that there are sufficient control points for imposing inter-element continuity constraints. The last step is to replace the control points at boundary with those governing the original NURBS curves. This boundary replacement algorithm is also discussed in [107]. Thus, a geometrically exact domain triangulation admitting sharp geometric features can be established.

A Kirchhoff plate formulation is implemented into the algorithm. To verify our modeling approach, a number of plate models bounded by complicated NURBS curves are investigated in the context of static bending and free vibration analysis. Numerical results prove the accuracy and efficiency of the proposed method.

4.2 A Brief Review of NURBS and Rational Bézier Triangles

In this section, we give a brief review on the fundamentals of Bézier curves [113], NURBS [1] and the construction of rational triangular Bézier spline spaces [21].

4.2.1 Bézier and NURBS Curve

In one dimension, a degree-*n* Bernstein polynomial is defined as follows

$$B_i^n(t) = \binom{n}{i} t^i (1-t)^{n-i} \tag{4.1}$$

where $t \in [0,1]$, $\binom{n}{i} = \frac{n!}{i!(n-i)!}$ is the binomial coefficient.

A Bézier curve $S(t)$ is constructed as a linear combination of $n+1$ Bernstein polynomials $B_i^n(t)$ and the corresponding set of control points b_i, which can be expressed as

$$S(t) = \sum_{i=1}^{n+1} B_i^n(t) b_i \tag{4.2}$$

The B-spline basis functions are related to the Bernstein basis through a Bézier extraction operator *C* [114] uniquely defined by a specified knot vector on the parametric space, and is written as

$$N(t) = CB(t) \tag{4.3}$$

Through projection of the B-splines from $\Re^d$ to $\Re^{d+1}$ using the weights associated with the corresponding control points, a degree-*n* NURBS curve is then given as

$$R_i^n(t) = \frac{N_i^n(t) w_i}{\sum_{j=1}^{ncp} N_j^n(t) w_j} \tag{4.4}$$

where ncp denotes the number of control points used to define the curve.

4.2.2 Rational Bézier Triangles

A bivariate Bernstein polynomial can be constructed on a triangular domain as

$$B_{ijk}^n(\mathbf{u}) = \frac{n!}{i!\,j!\,k!} u_1^i u_2^j u_3^k \tag{4.5}$$

where n is the polynomial order, the triplet (i, j, k) represent the ordinate index that sum to n, and $\mathbf{u} = \{u_1, u_2, u_3\}$ denote the barycentric coordinates of a point in the triangle.

The rational form of the above Bernstein basis functions is written as

$$R_{ijk}^n = \frac{B_{ijk}^n(\mathbf{u}) w_{ijk}}{\sum_{r+s+t=n} B_{rst}^n(\mathbf{u}) w_{rst}} \tag{4.6}$$

where w is the weight.

Finally, a rational triangular Bézier space can be defined as a linear combination of the rational Bernstein basis functions $R_{ijk}^n(\mathbf{u})$ and the corresponding control points b_{ijk}

$$T(\mathbf{u}) = \sum_{i+j+k=n} R_{ijk}^n(\mathbf{u}) b_{ijk} \tag{4.7}$$

Fig. 4-1 illustrates the control lattice of linear, quadratic and cubic Bézier triangles on the parametric domain, respectively.

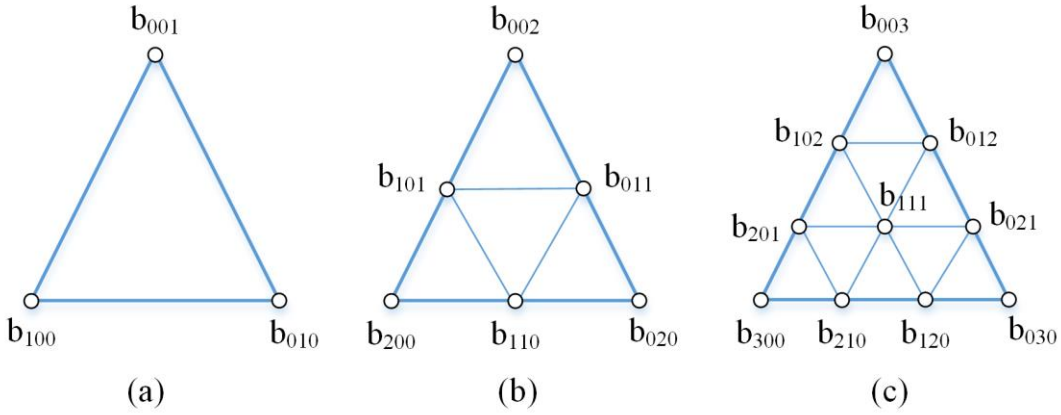

Figure 4-1: Control lattice of a Bézier triangle: (a) linear; (b) quadratic; and (c) cubic

4.3 Delaunay-based Feature-preserving Automatic Mesh Generation

Unstructured mesh generation has been a very popular field over the past a few decades and is by itself a very mature technique. Therefore, we leverage on the wide variety of existing meshing tools, such as mesh2d [112] and TriGA [4,21], for the generation of a Delaunay-based feature-preserving domain triangulation. The utilization of such a feature-preserving meshing algorithm carries significant meanings in smeared damage analysis, as it is very likely that damage initiates at sharp curvatures or geometric imperfections due to stress concentration, and the feature-preserving algorithm is extremely good at resolving small geometric features. The meshing algorithm is briefly discussed here for completeness. Readers can refer to the literature, e.g., [4,21,112], for more details.

The essential idea of the mesh generation algorithm is to construct a high-quality polygon approximation of the original input NURBS curves as the first step. Secondly, the construction of a quadtree decomposition that matches the local geometry feature is performed in order to evaluate the element size distribution required to resolve the geometry. The algorithm optimizes the control point location and mesh topology via an iterative process, where a constrained Delaunay

triangulation with a sequence of Laplacian smoothing is performed in each iteration. After a high-quality triangulation is obtained, the patch is converted to a cubic one and the control points at the domain boundary are replaced by the control points of the original NURBS to exactly recover the boundary. The procedure is illustrated for the domain shown in Fig. 4-2a and is described as follows:

a. Construct an initial polygon approximation (Fig. 4-2b). The input NURBS curves are first subdivided via knot insertion. This process is governed by a measure of the relative difference between the length of the curve for each knot span and the length of the associated polygon formed by connecting the control points. The process iterates until the relative differences for all the knot spans are below a prescribed threshold.

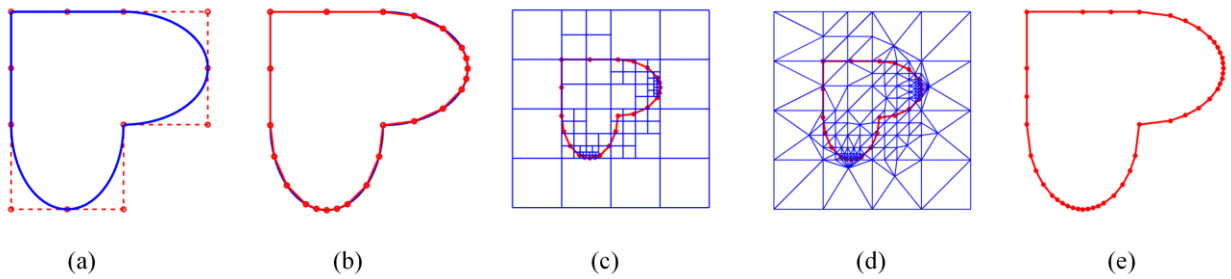

Figure 4-2: Construct a polygon approximation: (a) input NURBS; (b) initial polygon construction; (c) quadtree decomposition; (d) triangulating quadtree; and (e) final polygon approximation.

b. Construct quadtree decomposition and refine polygon approximation (Fig. 4-2c-e). In this step, a quadtree background mesh is constructed and used to further refine the polygon. In particular, the algorithm generates a bounding box that encloses the geometry. The bounding box is then recursively subdivided until the dimension of each box matches the local geometry feature size (Fig. 4-2c). A size function is also evaluated at the quadtree vertices based on the minimum neighboring box dimension at the vertex. Subsequently, the quadtree mesh is triangulated so that we can linearly interpolate the size function at the polygon control points (Fig. 4-2d). Knot insertion is performed if the ratio of the edge length to the size function is above a given threshold.

c. Perform Delaunay-based triangulation with Laplacian smoothing. In this step, the polygon approximation from Step *b* is triangulated based on the quadtree background mesh. The initial nodes are taken as the fixed polygon vertices and the internal nodes from the quadtree mesh. The algorithm optimizes the node location and mesh topology in an iterative manner. Specifically, a constrained Delaunay triangulation is constructed at every iteration. Nodes are then added or removed from the mesh to meet the required element size distribution. In particular, the size functions h_{cent} at the centroid of the triangles are computed through linear interpolation of the size functions at the nodes. The required triangle areas A_h are then estimated as

$$A_h = \frac{1}{2} h_{cen}^2 \tag{4.8}$$

The quality of the triangles are measured in terms of the area-length ratio, with the length being the root-mean-square of the triangle edge lengths. Nodes are added at the centroid of the triangle in cases where large triangles or low-quality triangles are present. On the contrary, nodes are removed if the associated triangle area or edge length is too small. A Laplacian smoothing operation (e.g., a spring-based smoothing) is performed after the node manipulation. The iteration continues until all the triangles are of high quality and meet the element size constraints. This process is briefly illustrated in Fig. 4-3.

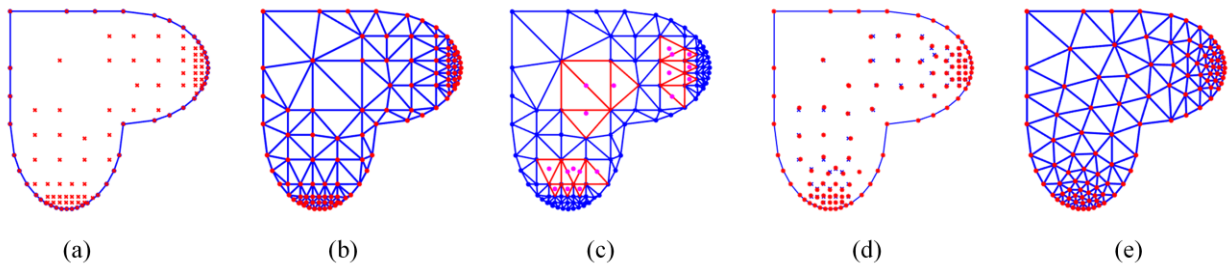

Figure 4-3: Perform Delaunay-based triangulation with Laplacian smoothing: (a) initial nodes; (b) initial constrained Delaunay triangulation; (c) adding new nodes at the centroid of the marked triangles; (d) Laplacian smoothing; and (e) final Delaunay tessellation

d. Elevate polynomial degree and recover boundary. In this step, the polynomial degree is raised to cubic (i.e., standard degree in CAD) through linear interpolation. Moreover, knot insertion on the input NURBS curves is performed until the knots corresponding to the polygon vertices have multiplicity p (p = 3 in the case of cubic NURBS). As of now, there are four control points at each knot span that correspond to the edge nodes of the boundary triangles. We simply replace the control points at the boundary with the control points of the input NURBS curves for exact boundary control. Fig. 4-4 demonstrates the consequences of this step.

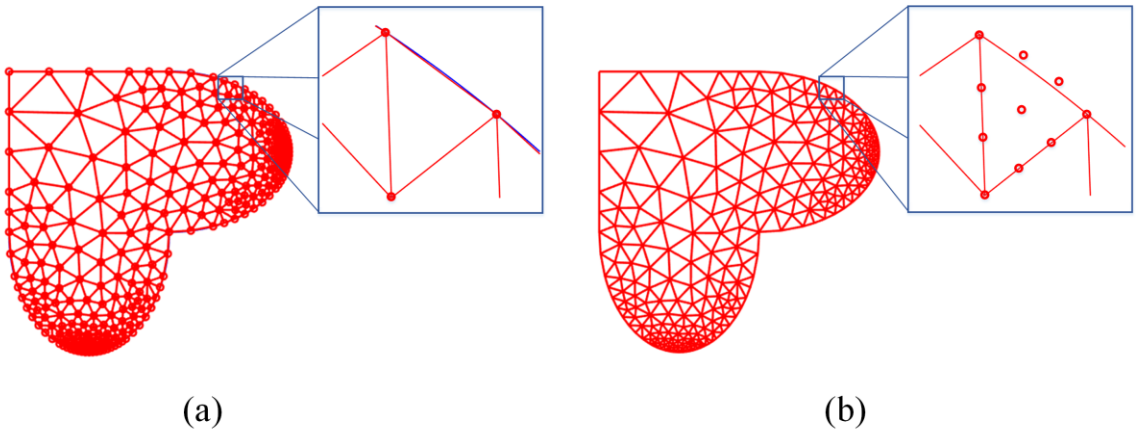

Figure 4-4: Elevate polynomial degree and recover boundary: (a) constrained Delaunay tessellation with approximated boundary; and (b) constrained Delaunay tessellation with exact boundary.

4.4 Enforcing High-order Continuity via Lagrange Multipliers

In this section, the C^r continuity constraints for inter-element continuity are explicitly defined. In order to impose the continuity constraints, a number of approaches can be used: (1) the master-slave method, (2) penalty method, (3) boundary minimum determining set (BMDS) approach, and (4) Lagrange multipliers. The master-slave method is inferior in handling arbitrary constraints. The penalty method requires careful selection of the penalty weight to avoid ill-conditioning. In the BMDS used in [107], solving for the reduced row echelon form is computationally expensive. Moreover, relaxing the constraints on the boundary vertices by restraining the internal free vertices that have influence on the constrained boundary vertices requires user intervention. In addition,

careful selection of the free internal vertices is necessary to avoid inaccurate results. On the other hand, the continuity constraints can be exactly enforced through the use of Lagrange multipliers, but this method increases the size of the problem by the number of constraint equations. In the following, we provide an iterative solution procedure presented in [115] that solves the Lagrange multiplier augmented system without increasing the system size.

In the domain discretized by Bézier triangles, the neighboring triangles are connected with C^0 continuity. However, the formulation of Kirchhoff plate involves second order derivatives of the basis functions, and therefore raising the degree of continuity at the common edges is necessary.

Assuming two adjacent triangles $T(v_1,v_2,v_3)$ and $\tilde{T}(v_4,v_3,v_2)$ that share the edge v_2v_3, they can be joined with C^r differentiability if and only if [111]:

$$\tilde{b}_{\gamma jk} = \sum_{\mu+\nu+\kappa=\gamma} \frac{\gamma!}{\mu!\nu!\kappa!} b_{\mu,k+\nu,j+\kappa} u_1^{\mu} u_2^{\nu} u_3^{\kappa} \tag{4.9}$$

where $0 \le \gamma \le r$, $\gamma + j + k = n$, $\{u_1,u_2,u_3\}$ are the barycentric coordinates of the vertex v_4 relative to T. An example is shown in Fig. 4-5(a) where two cubic triangles are joined with C^1 continuity and Fig. 4-5(b) where the two cubic triangles are joined with C^2 continuity.

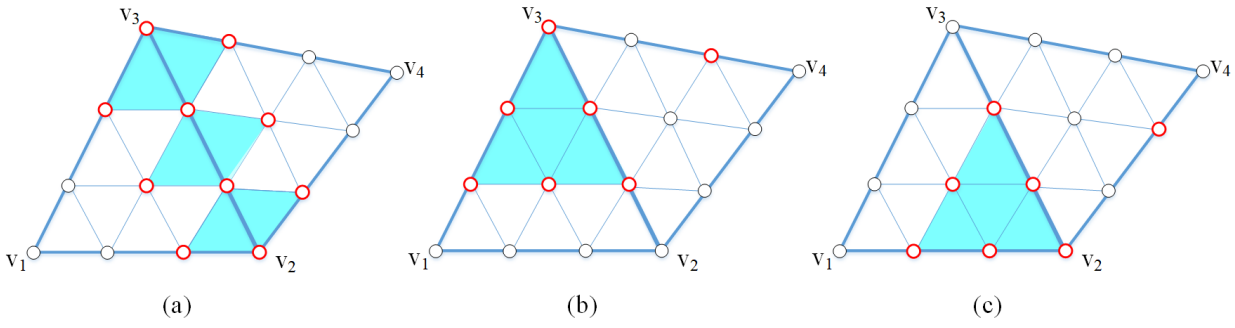

Figure 4-5: Enforcing higher-order continuity with Lagrange multipliers (vertices involved in C^1 and C^2 continuity constraints are highlighted in red: (a) C^1 continuity and (b-c) constrained vertices in addition to (a) for C^2 continuity.

Collecting the continuity constraints computed in Eq. (4.9), we can write them in matrix form as

$$\mathbf{L}\mathbf{d} = \mathbf{G} \tag{4.10}$$

where $\mathbf{L}$ is the matrix containing the coefficients of the constraints, $\mathbf{d}$ is the vector including the ordinate information, and $\mathbf{G}$ is the right-hand side of the continuity constraint equations. $\mathbf{G} = \mathbf{0}$ in the case of enforcing the continuity constraints. We use $\mathbf{G}$ in the derivation to keep the method general. Note that, to avoid the ill-conditioning of the augmented stiffness matrix, in which the $\mathbf{L}$ matrix is not of full rank, a preprocessing step is recommended to sort out the linearly independent rows in $\mathbf{L}$ to use for enforcing higher-order continuity.

The Lagrange multiplier augmented system can be expressed as follows

$$\begin{bmatrix} \mathbf{K} & \mathbf{L}^T \\ \mathbf{L} & \mathbf{0} \end{bmatrix} \begin{bmatrix} \mathbf{d} \\ \boldsymbol{\lambda} \end{bmatrix} = \begin{bmatrix} \mathbf{F} \\ \mathbf{G} \end{bmatrix} \tag{4.11}$$

where $\mathbf{K}$ is the stiffness matrix, $\mathbf{F}$ is the forcing vector, and $\boldsymbol{\lambda}$ denotes the Lagrange multiplier vector.

When a large number of continuity constraints are to be enforced, solving Eq. (4.11) can be very costly. Alternatively, an iterative approach can be used to solve the problem without increasing the matrix size. Consider a variant of Eq. (4.11) where the lower diagonal block of zeros is replaced by a diagonal matrix consisting of small numbers, termed a constraint-scaling diagonal matrix, i.e.

$$\begin{bmatrix} \mathbf{K} & \mathbf{L}^T \\ \mathbf{L} & -\varepsilon\mathbf{I} \end{bmatrix} \begin{bmatrix} \mathbf{d} \\ \boldsymbol{\lambda} \end{bmatrix} = \begin{bmatrix} \mathbf{F} \\ \mathbf{G} - \varepsilon\boldsymbol{\lambda} \end{bmatrix} \tag{4.12}$$

where ε is a small number and $\mathbf{I}$ is the identity matrix.

The above system can be expressed in an iterative form as

$$\mathbf{K}\mathbf{d}^{(i+1)} + \mathbf{L}^T\boldsymbol{\lambda}^{(i+1)} = \mathbf{F} \tag{4.13}$$

$$\mathbf{L}\mathbf{d}^{(i+1)} - \varepsilon\boldsymbol{\lambda}^{(i+1)} = \mathbf{G} - \varepsilon\boldsymbol{\lambda}^{(i)}$$

where i indicates the i^{th} iteration.

Multiplication of $\mathbf{L}^T$ to the second equation in Eq. (4.13) and rearranging terms yields

$$\mathbf{L}^T\boldsymbol{\lambda}^{(i+1)} = w\mathbf{L}^T\mathbf{L}\mathbf{d}^{(i+1)} - w\mathbf{L}^T\mathbf{G} + \mathbf{L}^T\boldsymbol{\lambda}^{(i)} \tag{4.14}$$

where $w = \dfrac{1}{\varepsilon}$ is the weight.

Combining Eq. (4.14) with the first equation in Eq. (4.13) results in the following

$$\left(\mathbf{K} + w\mathbf{L}^T\mathbf{L}\right)\mathbf{d}^{(i+1)} = \mathbf{F} + w\mathbf{L}^T\mathbf{G} - \mathbf{L}^T\boldsymbol{\lambda}^{(i)} \tag{4.15}$$

Taking an initial guess of $\boldsymbol{\lambda}^{(0)} = \mathbf{0}$ yields

$$\mathbf{d}^{(1)} = \left(\mathbf{K} + w\mathbf{L}^T\mathbf{L}\right)^{-1}\left(\mathbf{F} + w\mathbf{L}^T\mathbf{G}\right) \tag{4.16}$$

Recall from the first equation of Eq. (4.13) that $\mathbf{F} = \mathbf{K}\mathbf{d}^{(i)} + \mathbf{L}^T\boldsymbol{\lambda}^{(i)}$. Substituting this into Eq. (4.15) leads to

$$\mathbf{d}^{(i+1)} = \left(\mathbf{K} + w\mathbf{L}^T\mathbf{L}\right)^{-1}\left(\mathbf{K}\mathbf{d}^{(i)} + w\mathbf{L}^T\mathbf{G}\right) \tag{4.17}$$

Eq. (4.16) and Eq. (4.17) can be used to solve the augmented Lagrangian system iteratively. Note that this method essentially combines the penalty method with the Lagrange multiplier method. By solving the problem iteratively, it circumvents the problematic ill-conditioning issue exhibited in the penalty method.

4.5 Governing Equations for the Kirchhoff Plate

4.5.1 Kinematics

Let m_{ij} be the bending moment of a plate and q the external distributed load vector. The equilibrium equation for a Kirchhoff plate can be expressed as

$$m_{ij,ij} = q \tag{4.18}$$

where the comma indicates differentiation and i, j are the indexes ranging from one to two, since the out-of-plane stresses are assumed to be zero.

Multiplying Eq. (4.18) with the variation in transverse displacement δd and integrating over the entire domain Ω yields the following

$$\int_\Omega \delta d_{,ij} m_{ij} d\Omega + \int_{\partial\Omega} \left(\delta d m_{ij,j} n_i - Q\right) ds + \int_{\partial\Omega} \left(-\delta d_{,i} m_{ij} n_j + M_i\right) ds = \int_\Omega \delta d q d\Omega \tag{4.19}$$

where $d_{,ij} = \kappa_{ij}$ is the curvature The second and third terms on the left-hand side are the shear and moment boundary conditions on the boundary $\partial\Omega$, respectively. Neglecting the boundary terms yields the weak form

$$\int_\Omega \delta\kappa_{ij} m_{ij} d\Omega = \int_\Omega \delta d q d\Omega \tag{4.20}$$

In Eq. (4.20), the bending moments m_{ij} can be computed as

$$m_{ij} = -\int_{-t/2}^{t/2} \sigma_{ij} z dz \tag{4.21}$$

where t is the thickness of the plate.

The stress-strain relationship for a homogeneous and isotropic plate is

$$\sigma_{ij} = \begin{bmatrix} \sigma_{11} \\ \sigma_{22} \\ \sigma_{12} \end{bmatrix} = \frac{E}{1-\nu^2} \begin{bmatrix} 1 & \nu & 0 \\ \nu & 1 & 0 \\ 0 & 0 & \frac{1-\nu}{2} \end{bmatrix} \begin{bmatrix} \varepsilon_{11} \\ \varepsilon_{22} \\ 2\varepsilon_{12} \end{bmatrix} \tag{4.22}$$

where E and ν represent the Young's modulus and Poisson's ratio, respectively. Eq. (4.22) can be written in shorthand as $\sigma_{ij} = \mathbf{C}\varepsilon_{ij}$. The strain vector can be rewritten in terms of transverse displacement as

$$\varepsilon_{11} = -z\frac{\partial^2 d}{\partial x^2},\ \varepsilon_{22} = -z\frac{\partial^2 d}{\partial y^2},\ \varepsilon_{12} = -z\frac{\partial^2 d}{\partial x \partial y} \tag{4.23}$$

Substituting Eq. (4.22) and Eq. (4.23) into Eq. (4.21) leads to the moment-curvature relationship

$$\begin{bmatrix} m_{11} \\ m_{22} \\ m_{12} \end{bmatrix} = \frac{Et^3}{12\left(1-\nu^2\right)} \begin{bmatrix} 1 & \nu & 0 \\ \nu & 1 & 0 \\ 0 & 0 & \frac{1-\nu}{2} \end{bmatrix} \begin{bmatrix} \kappa_{11} \\ \kappa_{22} \\ 2\kappa_{12} \end{bmatrix} \tag{4.24}$$

Combining Eq. (4.24) and Eq. (4.20) gives

$$\int_\Omega \delta\kappa_{ij} \mathbf{C} \kappa_{ij} d\Omega = \int_\Omega \delta d q d\Omega \tag{4.25}$$

where $\mathbf{C}$ is the material matrix shown in Eq. (4.24).

4.5.2 Discretized form

The input NURBS geometry is triangulated using the approach discussed in Section 4.3 along with the rational triangular Bézier splines. Recall from Section 4.2 that $\mathbf{R}$ is the rational Bézier

basis function used to represent a triangular patch. The transverse displacement in one patch can then be represented using the following

$$d = \mathbf{R}\mathbf{d} \tag{4.26}$$

Differentiating Eq. (4.26) twice with respect to the physical coordinates results in the expression for the curvature

$$\kappa = \mathbf{B}\mathbf{d} \tag{4.27}$$

where $\mathbf{B} = \left[\frac{\partial^2 \mathbf{R}}{\partial x^2} \quad \frac{\partial^2 \mathbf{R}}{\partial y^2} \quad 2\frac{\partial^2 \mathbf{R}}{\partial x \partial y} \right]^T$.

Substituting Eq. (4.26) and Eq. (4.27) into Eq. (4.25) leads to the final expression of the weak form

$$\int_\Omega \delta \mathbf{d}^T \mathbf{B}^T \mathbf{C}\mathbf{B}\mathbf{d} d\Omega = \int_\Omega \delta \mathbf{d}^T \mathbf{R} q d\Omega \tag{4.28}$$

From the virtual work equation (i.e., Eq. (4.28)), we obtain the stiffness $\mathbf{K}$ and forcing terms $\mathbf{F}$, i.e.,

$$\mathbf{K} = \int_\Omega \mathbf{B}^T \mathbf{C}\mathbf{B} d\Omega \tag{4.29}$$

$$\mathbf{F} = \int_\Omega \mathbf{R} q d\Omega$$

4.5.3 Free Vibration Analysis

For free vibration analysis of the Kirchhoff plate, the weak form of the elastodynamic equilibrium equation is written as follows:

$$\int_{\Omega} \delta\boldsymbol{\varepsilon}^T \mathbf{C}\boldsymbol{\varepsilon} d\Omega + \int_{\Omega} \delta\mathbf{u}^T \rho t \ddot{\mathbf{u}} d\Omega = 0 \tag{4.30}$$

where ρ is the mass density, $\mathbf{u}$ is the displacement tensor and $\ddot{\mathbf{u}}$ represents the acceleration tensor. The displacement tensor is defined as

$$\mathbf{u} = \begin{bmatrix} u & v & d \end{bmatrix}^T = \begin{bmatrix} -z\dfrac{\partial}{\partial x} & -z\dfrac{\partial}{\partial y} & 1 \end{bmatrix}^T d \tag{4.31}$$

and the acceleration tensor is obtained from Eq. (4.31) by differentiating twice in time.

Eq. (4.30) can be concisely expressed in the form

$$\mathbf{K}\mathbf{d} + \mathbf{M}\ddot{\mathbf{d}} = \mathbf{0} \tag{4.32}$$

Based on Eq. (4.26) and integrating over the thickness, the mass matrix takes the form

$$M_{ij} = \int_{\Omega} \rho \left(R_i R_j t + \frac{\partial R_i}{\partial x}\frac{\partial R_j}{\partial x}\frac{t^3}{12} + \frac{\partial R_i}{\partial y}\frac{\partial R_j}{\partial y}\frac{t^3}{12} \right) d\Omega \tag{4.33}$$

The general solution of Eq. (4.32) is

$$\mathbf{d} = \mathbf{d}_{\phi} \sin(\omega t + \theta) \tag{4.34}$$

where ω is the frequency and $\mathbf{d}_{\phi}$ denotes the eigenmode obtained from the following eigenvalue problem

$$\left(\mathbf{K} - \omega^2 \mathbf{M}\right)\mathbf{d} = \mathbf{0} \tag{4.35}$$

The above problem essentially amounts to a generalized constrained eigenvalue problem, the solution of which requires special treatment. To solve Eq. (4.35), a solution procedure presented in [116] is used to compute a constrained stiffness matrix incorporating Lagrange multipliers. The

natural frequencies and eigenmodes governing the vibration are further obtained from the eigenvalue analysis.

4.6 Numerical examples

In this section, four numerical examples of Kirchhoff plates of complicated geometries are demonstrated in the context of static bending and free vibration analysis. For all of the examples shown, a 28-point quadrature rule is used for the integration over the triangle, and a 5-point quadrature rule is employed for the integration over the edges to ensure the accuracy of the solution. The results are compared to analytical solutions, if available, or converged finite element solutions using Abaqus.

4.6.1 Bending of a Simply Supported Circular Plate

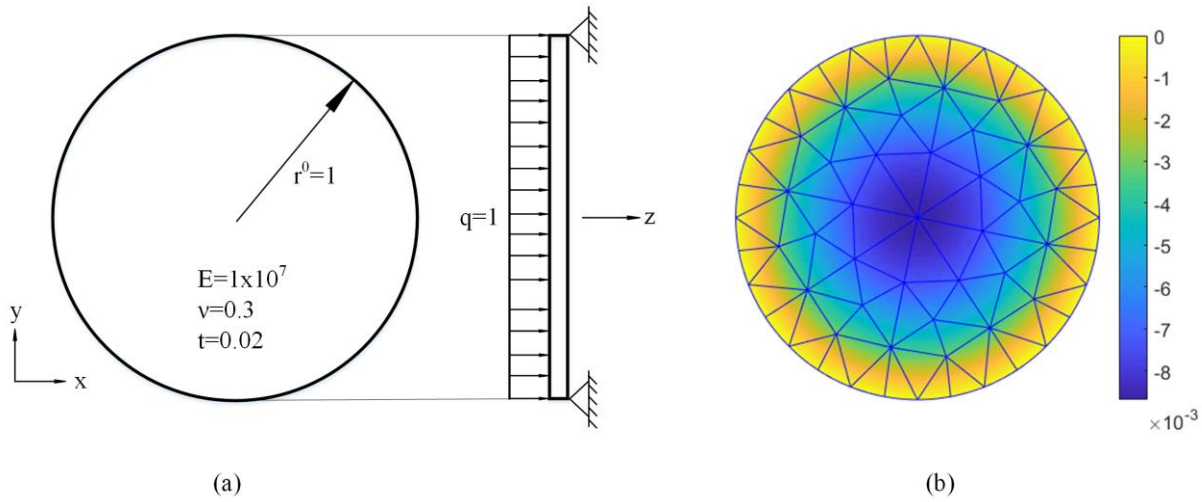

Figure 4-6: (a) Plate geometry and material properties, (b) deflection

To verify the plate formulation, a simply supported circular plate subjected to uniform loading is analyzed. For this example, an exact solution is available in [117] and is reproduced here in Eq. (4.36). The geometry and material properties are illustrated in Fig. 4-6 along with the deformed shape.

$$d(r) = -\frac{qr_0^2(3+\nu)r^2}{32D(1+\nu)} + \frac{qr^4}{64D} + \frac{qr_0^4(5+\nu)}{64D(1+\nu)} \tag{4.36}$$

where r is the radius of the point at query and $D = \frac{Et^3}{12(1-\nu^2)}$.

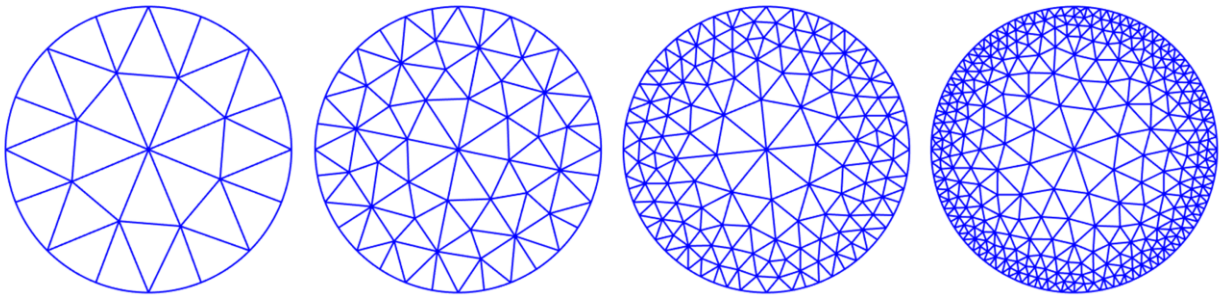

(a) (b) (c) (d)

Figure 4-7: Automatically generated mesh with threshold: (a) $\varphi \le 3\%$, (b) $\varphi \le 1\%$, (c) $\varphi \le 0.5\%$, and (d) $\varphi \le 0.1\%$.

Four meshes with different thresholds φ are illustrated in Fig. 4-7, from which it is easy to see that the boundary mesh becomes finer as the threshold value φ gets smaller. The relative error at the center of the plate and the L^2 relative error norm e_{L^2} are measured against the analytical solution. Results are also compared with uniform meshing using Abaqus linear triangular shell element S3 (see Table 4-1). Note that, Eq. (4.37) was used to calculate the L^2 norm e_{L^2}. In terms of the relative error at the center of the plate, we observe that our solution with $\varphi \le 3\%$ already outperforms the Abaqus model with 604 nodes. The L^2 relative error norm also shows a faster convergence with our proposed model. Worth noting is that the Abaqus S3 element for thin plate analysis employs five degrees of freedom (DOF) per node, whereas our proposed element has only one DOF per node, which further demonstrates a significant saving in computational cost.

$$e_{L^2} = \frac{\sqrt{\int_\Omega \left(d^h - d\right)^2 d\Omega}}{\sqrt{\int_\Omega d^2 d\Omega}} \tag{4.37}$$

Table 4-1: Relative error in deflection using different thresholds

Threshold φ	$\leq 3\%$	$\leq 1\%$	$\leq 0.5\%$	$\leq 0.1\%$	Abaqus				exact solution
#nodes	169	481	1273	3004	37	105	237	604	-
#DOF	169	481	1273	3004	185	525	1185	3020	-
center deflection $\times 10^{-3}$	-8.699	-8.690	-8.694	-8.699	-7.996	-8.430	-8.564	-8.655	-8.695
relative error	0.046%	0.058%	0.005%	0.050%	8.039%	3.048%	1.507%	0.460%	-
e_{L^2}	0.803%	0.181%	0.065%	0.012%	7.724%	2.287%	0.910%	0.311%	-

4.6.2 Bending of a Perforated Circular Plate

In this example, a more complicated geometry is used to demonstrate the ability of the proposed approach in capturing local geometric features. Specifically, a perforated circular plate with simply supported boundary condition is subjected to uniformly distributed load. The dimensions, loading condition, and the simulation results are shown in Fig. 4-8. The material properties are the same as in the first example.

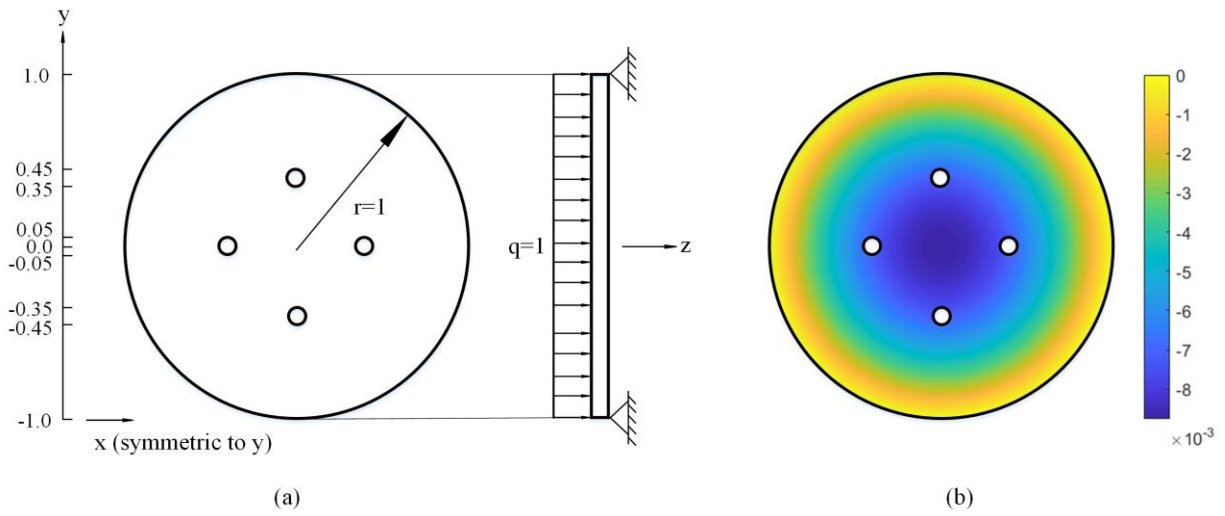

Figure 4-8: (a) Plate geometry and material properties, and (b) deflection

To illustrate the capability of the proposed approach in discretizing space bounded by complicated NURBS curves, four meshes of the perforated plate are shown in Fig. 4-9. As we can see, the holes in the plate are accurately captured. To verify the deformation, our results are compared with the converged solution using the Abaqus linear shell element S3, as listed in Table 4-2. Again, we observe that the results agree very well.

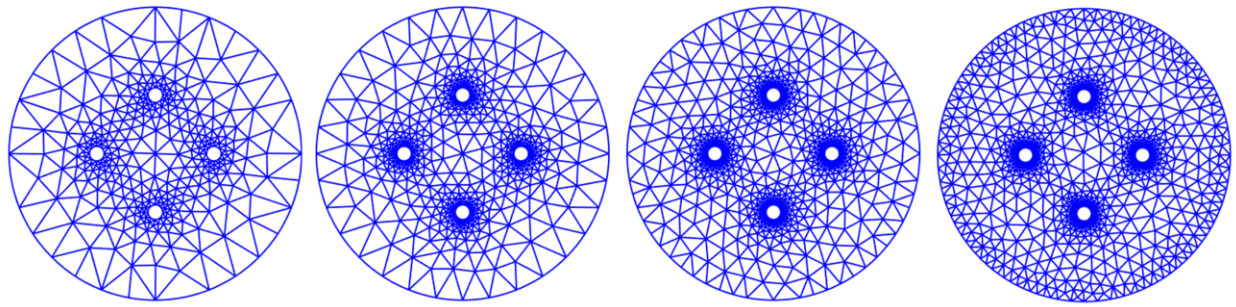

Figure 4-9: Automatically generated mesh with threshold: (a) $\varphi \le 3\%$, (b) $\varphi \le 1\%$, (c) $\varphi \le 0.5\%$, and (d) $\varphi \le 0.1\%$.

Table 4-2: Relative error in deflection using different thresholds

Threshold φ	$\le 3\%$	$\le 1\%$	$\le 0.5\%$	$\le 0.1\%$	Abaqus
#DOF	2949	5154	9219	17109	162600

max deflection	-0.007367	-0.008273	-0.008608	-0.008772	-0.008950
relative error	17.687%	7.564%	3.821%	1.988%	-

Note that the relative error at $\varphi \le 3\%$ is fairly large, but it does not indicate that $\varphi \le 3\%$ is not a good setting for all cases. The threshold φ is merely a control parameter relative to the dimension of the local feature. In other words, $\varphi \le 3\%$ is likely to result in very satisfying result if the radius of the holes in the plate is not very small.

4.6.3 Free Vibration of a Square Plate with an Elliptical Hole

In this section, the undamped free vibration analysis of a simply supported square plate with an elliptical hole of varying radius is investigated. The dimension of the plate is illustrated in Fig. 4-10. The thickness of the plate is $t = 0.05m$. The material properties are: Young's modulus $E = 2\times10^{11}\, N/m^2$, Poisson's ratio $\nu = 0.3$ and mass density $\rho = 8000\, kg/m^3$. The mesh generated with $\varphi \le 1\%$ is shown in Fig. 4-11.

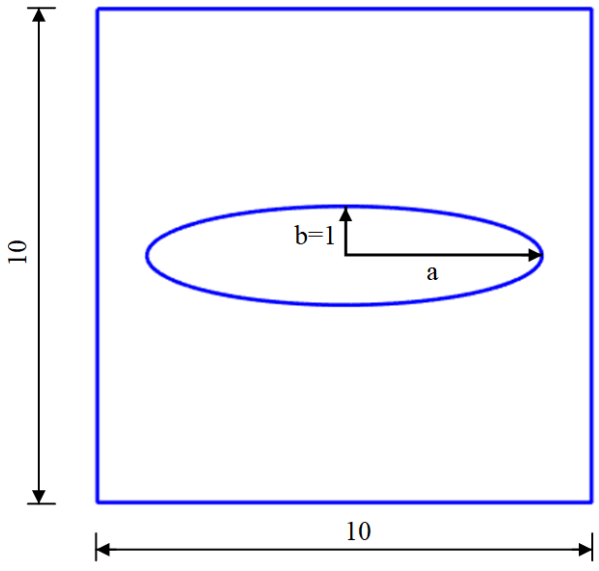

Figure 4-10: Dimension of the plate with an elliptical hole

The dimensionless parameter Ω_{nd} is used to measure the natural frequency and is defined as

$$\Omega_{nd} = \left(\frac{\omega^2 \rho t a^4}{D} \right)^{\frac{1}{4}} \tag{4.38}$$

The solutions are compared with those modeled using the Abaqus linear shell element S4R and are listed in Table 4-3. As we can see, the results are in very good agreement. The first 10 vibration modes are plotted in Fig. 4-12 for illustrative purposes.

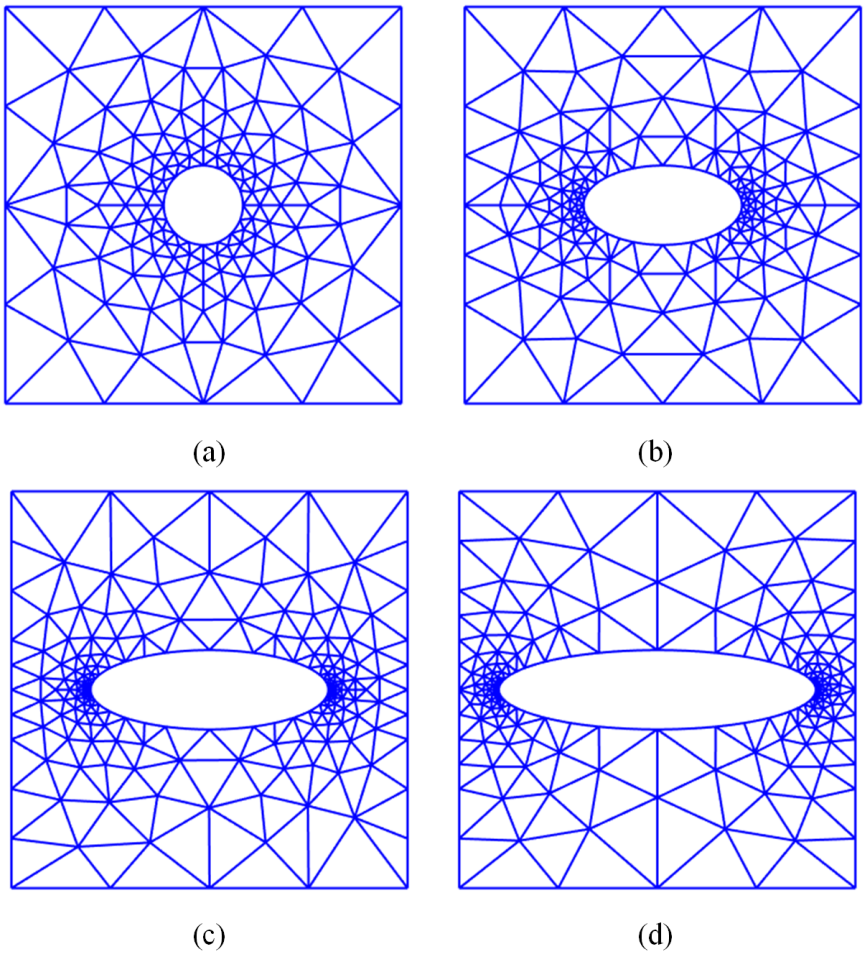

Figure 4-11: Automatically generated meshes for the plate with elliptical hole for $\varphi \leq 1\%$: (a) $a/b = 1$, (b) $a/b = 2$, (c) $a/b = 3$, and (d) $a/b = 4$.

Table 4-3: Natural frequencies of the square plate with an elliptical hole

Mode	$a/b=1$				$a/b=2$			$a/b=3$			$a/b=4$		
	Abaqus	$\varphi \le 3\%$	$\varphi \le 1\%$	$\varphi \le 0.5\%$	Abaqus	$\varphi \le 1\%$	$\varphi \le 0.5\%$	Abaqus	$\varphi \le 1\%$	$\varphi \le 0.5\%$	Abaqus	$\varphi \le 1\%$	$\varphi \le 0.5\%$
#nodes	11734	585	1128	2001	11382	1314	2034	10835	1644	2505	10623	1530	2196
1	4.3876	4.5419	4.4809	4.4423	4.3725	4.5058	4.4587	4.3550	4.5108	4.4755	4.3436	4.5455	4.4970
2	6.9581	7.1086	6.9936	6.9669	6.6411	6.6689	6.6613	6.0098	6.0724	6.0484	5.3019	5.3728	5.3734
3	6.9582	7.1720	6.9937	6.9683	6.9127	6.9162	6.9227	6.9298	6.9783	6.9681	6.9975	7.1451	7.0998
4	8.7803	8.8150	8.8040	8.8067	8.6904	8.6915	8.7006	8.4595	8.4901	8.4783	7.9516	8.0177	8.0112
5	9.7965	9.8998	9.8113	9.8027	9.6815	9.6819	9.6840	9.6498	9.6792	9.6723	9.7759	9.9202	9.8772
6	10.0848	10.4552	10.3084	10.2298	10.3845	10.5686	10.5129	10.4431	10.5391	10.5203	10.3834	10.4428	10.4390
7	11.2292	11.3397	11.2882	11.2987	10.8277	10.9352	10.9038	10.4642	10.5433	10.5284	10.4189	10.4877	10.4871
8	11.2293	11.3483	11.2883	11.2994	11.2325	11.2764	11.2692	11.3071	11.3736	11.3502	10.9105	11.0077	11.0073
9	12.7027	12.9518	12.8121	12.8005	12.0485	12.1568	12.1390	11.5094	11.5863	11.5666	11.5470	11.6823	11.6525
10	12.7032	12.9707	12.8124	12.8012	12.9157	13.0627	13.0437	12.8471	13.0027	12.9357	12.2924	12.4050	12.4054

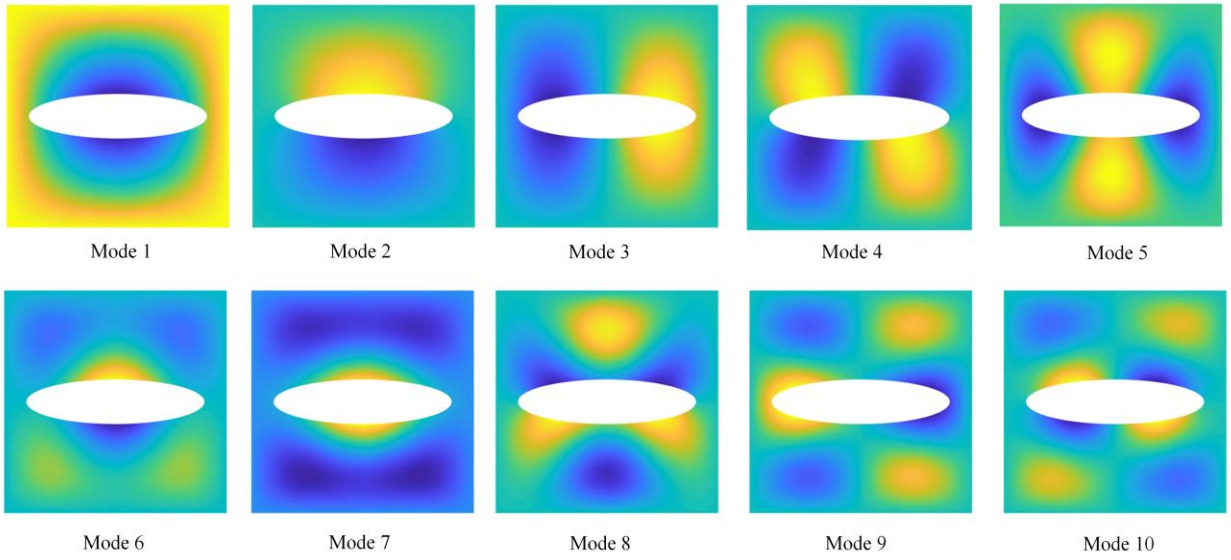

Figure 4-12: The first 10 mode shapes of the plate with an elliptical hole ($a/b = 4$)

4.6.4 Free Vibration of a Square Plate with a Heart-shape Cutout

In the last example, a simply supported square plate with a heart-shape cutout is used to demonstrate the performance of the proposed plate model. The dimension of the plate is shown in Fig. 4-13. The thickness of the plate is $t = 0.05m$. The material properties are the same as the third example. Free vibration analysis is conducted, for which a number of reference solutions are available in the literature [94,118,119]. The dimensionless parameter Ω_{nd} defined in Eq. (4.38) is used to measure the natural frequency.

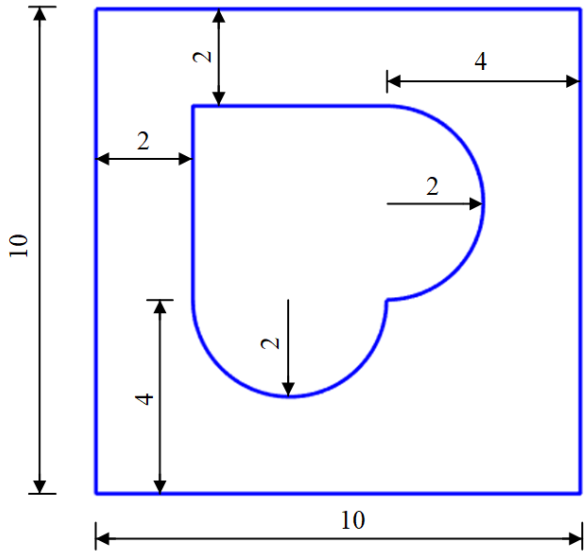

Figure 4-13: Dimension of the plate with a heart-shaped hole

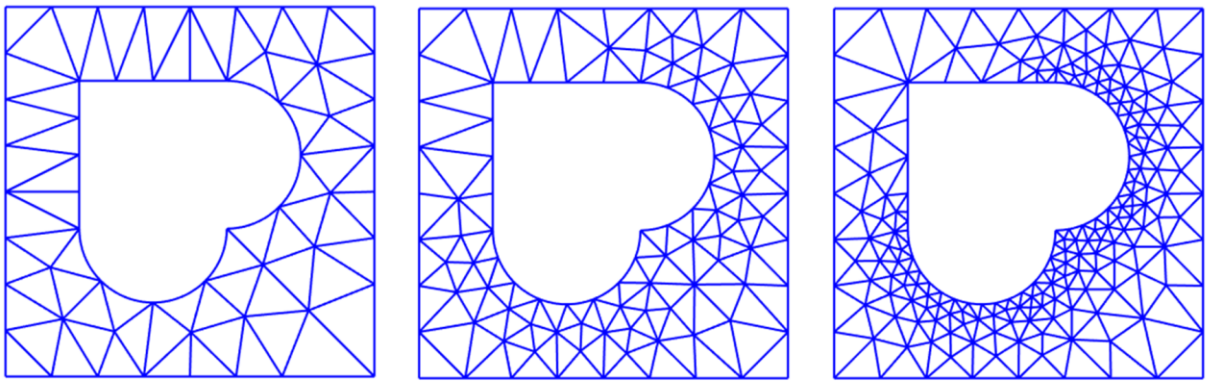

Figure 4-14: Automatically generated meshes for the plate with a heart-shape cutout: (a) $\varphi \le 3\%$, (b) $\varphi \le 1\%$, and (c) $\varphi \le 0.5\%$.

The automatically generated meshes are shown in Fig. 4-14, in which we can observe that the proposed approach is able to handle sharp geometric corners fairly easily. The natural frequencies and mode shapes of the first 10 modes are listed and plotted in Table 4-4 and Fig. 4-15, respectively. As we can see, the free vibration results match very well with those in literature.

Table 4-4: Natural frequencies of the square plate with a heart-shape cutout

Mode	Threshold ϕ			Cubic NURBS [94]	Moving Kriging interpolation [118]	Radial point interpolation [119]
	$\leq 3\%$	$\leq 1\%$	$\leq 0.5\%$			
#nodes	384	777	1671	512	506	-
1	5.3688	5.1618	5.0386	5.193	5.3898	4.919
2	6.6041	6.4982	6.4205	6.579	7.5023	6.398
3	7.1068	6.9956	6.8818	6.597	8.3470	6.775
4	8.7629	8.6670	8.6151	7.819	10.6358	8.613
5	9.3238	9.1539	9.0555	8.812	11.0484	9.016
6	10.9440	10.7818	10.7140	9.420	12.8945	10.738
7	11.1755	11.0085	10.9480	10.742	13.7100	10.930
8	11.9959	11.7631	11.6683	10.776	14.0620	11.601
9	13.4042	12.9533	12.8590	11.919	16.6492	12.903
10	13.6026	13.3453	13.2412	13.200	17.3641	13.283

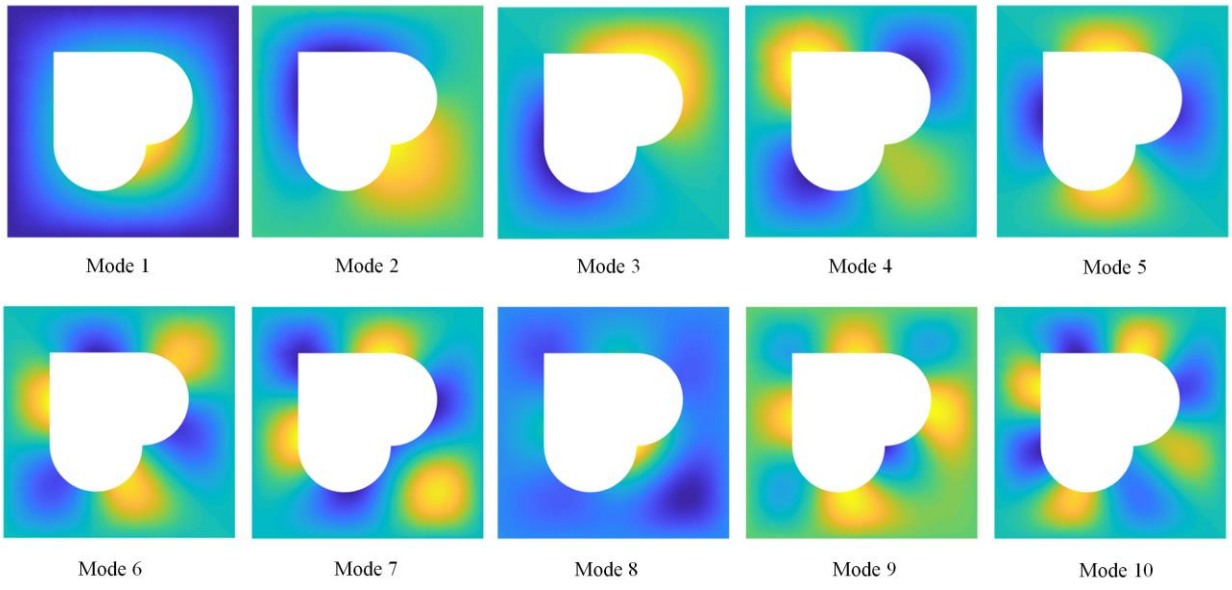

Figure 4-15: The first 10 mode shapes of the plate with a heart-shape cutout

4.7 Concluding Remarks

In this paper, we solved the Kirchhoff plate problem using isogeometric analysis (IGA). The parameter space was represented by rational Bézier triangles, and the analysis was further facilitated by an automatic meshing algorithm that admits local geometric features with high resolution. Due to the use of rational Bézier splines, the proposed model was extremely flexible for representing geometries comprised of complex topologies. In addition, the replacement of control points at domain boundaries yielded a geometrically exact model to be analyzed. By resorting to the Lagrange multipliers, the global continuity of the domain triangulation was elevated to C^1, which is suitable for Kirchhoff plate analysis. Numerical examples comprised of static bending and free vibration analysis of plates bounded by complicated NURBS curves verify the accuracy and efficiency of the proposed modeling approach. In the future, we intend to investigate the performance of the developed plate model for stability analysis.

Chapter 5 Feature-preserving Rational Bézier Triangles for Isogeometric Analysis of Higher-order Gradient Damage Models

The computational approach of modeling smeared damage with quadrilateral elements in isogeometric analysis (e.g., using NURBS or T-splines) has limitations in scenarios where complicated geometries are involved. In particular, the higher-order smoothness that emerges due to the inclusion of higher-order terms in the nonlocal formulation is not often easy to preserve with multiple NURBS patches or unstructured T-splines where reduced continuity is observed at patch interfaces and extraordinary points. This defect can be circumvented by the use of rational Bézier triangles for domain triangulation. In particular, rational Bézier triangles increase the flexibility in the discretization of arbitrary spaces and facilitate the handling of singular points that result from sharp changes in curvature. Moreover, the process of mesh generation can be completely automated and does not require any user intervention. A Delaunay-based feature-preserving discretization coupled with a local refinement technique is implemented to capture small geometric features and locally resolve areas of damage propagation. Additionally, we adopt an implicit higher-order gradient damage model in order to amend the non-physical mesh dependency issue exhibited in continuum damage analysis. For the solution of the fourth- and sixth-order gradient damage models, Lagrange multipliers are leveraged to elevate the global smoothness to any desired order in an explicit manner. The solution algorithm is initialized with the cylindrical arc-length control and switches to a dissipation-based arc-length control for better numerical stability as the damage evolves. Numerical examples with singularities demonstrate improvements in terms

of efficiency and accuracy, as compared to the damage models represented by Powell-Sabin B-splines.

5.1 Introduction

Continuum damage analysis [120] has limitations in approximating diffusive fracture due to the lack of an internal length parameter that propagates damage, thus resulting in a spurious mesh dependency issue. A number of approaches [121–123] have been proposed to eliminate this non-physical phenomenon, among which the nonlocal theory [123,124] and gradient damage models [110,125,126] have been considered the most effective. Nonlocal damage theory incorporates nonlocality by introducing a damage variable and considering it as a function of the nonlocal quantity, which is evaluated as the volume average of the local quantity. In particular, certain isotropic spatial smoothing functions (such as the Gauss weighting function [126]) are often used to take into account the interaction in the vicinity of the point being evaluated. On the other hand, in order to reduce the computational effort, second-order Taylor expansion of the original form can be used as a substitute of the nonlocal integrals, thus leading to a system of second-order partial differential equations (PDEs). This formulation is attractive from a parameterization standpoint as it only requires basis functions of C^0-continuity and therefore is suitable for standard finite element methods (FEM). However, it has been reported that the accuracy of using second-order gradient damage models is limited [127]. Thus, it is important to include higher-order terms in the Taylor approximation of the nonlocal integral, which has prompted the use of higher-order gradient damage models.

A variety of approaches can be adopted to discretize the space of the higher-order gradient damage models, one being the use of mixed formulations [128,129], where an auxiliary field is introduced in addition to the displacement and plastic strain fields such that the requirement for

basis functions of C^1-smoothness can be relaxed. However, this introduces a significant amount of additional degrees of freedom (DOF) and inevitably increases computational complexity. As an alternative, the Element-Free Galerkin (EFG) method [130] can be adopted since the underlying basis functions can be generated to a desired order of smoothness; however, its increased level of complexity and its incompatibility with standard FEM due to the non-element-based formulation impede its popularity. On the other hand, the high-order smoothness of basis functions can be automatically satisfied with the use of Non-Uniform Rational B-splines (NURBS) [2,3,5,7,8] and T-splines [13,131,132] in isogeometric analysis (IGA) [1]. IGA is also intriguing because it uses the same spline basis functions that are used in computer-aided design (CAD), and it is highly compatible with the data structures used in FEM codes [114,133]. It is important to note that a number of researchers have applied IGA to gradient damage analysis [24,110,126,134].

Nevertheless, the high-order smoothness is not always easy to preserve when it comes to the modeling of geometrically complex spaces when multiple NURBS patches or unstructured T-splines are used in the process of mesh generation. Consequently, additional treatments have to be carried out at patch interfaces [2,11] or in the vicinity of extraordinary points [135] to retain smoothness, which hinders their application. In such scenarios, domain triangulation appears to be a more powerful tool for parameterization as it is not topologically constrained to the quadrilateral meshgrid, making it much more flexible in discretizing arbitrary spaces. The use of Powell-Sabin (PS) B-splines in fourth-order gradient damage models has already been studied in [110] and showed promising results. Despite the ability to maintain C^1-smoothness throughout the entire domain of interest, a number of drawbacks are obvious. Firstly, due to the definition of PS triangles where they are required to contain all the associated PS points in order to obtain positive basis functions, the control points (i.e., the vertices of the PS triangles) are positioned in a random

manner. As a result, the users have no control over the location of the control points. This may be very inconvenient in cases where Dirichlet/Neumann boundary conditions have to be specified at a given point. Moreover, the definition of quintic PS triangles for C^2-continuity [102] is complicated, compared to enforcing higher-order continuities on Bézier triangles (which will be discussed later in this paper). In addition, it is not clear how the PS triangles can be extended to three dimensions for tetrahedral mesh generation.

As an alternative to PS triangles, rational Bézier triangles [4] can be used for domain triangulations. In this approach, the positioning of control points is very straightforward and does not depend on specific triangle-constructing rules. Moreover, the process of mesh generation starts from C^0 Bézier triangles, meaning that one can resort to a wide variety of existing meshing tools and automate the entire process. To raise the global continuity to a desired order, common constraint-enforcing techniques such as Lagrange multipliers [4] can be easily applied to impose continuity constraints in an explicit manner. Due to the use of the rational form of the Bézier triangles, exact boundary recovery can also be fulfilled at ease. Owing to these appealing merits, rational Bézier triangles are employed in this study. In order to capture small geometric features accurately and increase the flexibility in discretizing complicated domains, a Delaunay-based feature-preserving domain triangulation approach is also adopted in the current project, which turns out to be beneficial in capturing the initiation and early-stage propagation of damage.

In the study of gradient damage models, a very fine mesh is generally needed in order to capture the damage initiation and propagation. A natural solution is to resolve the space with high resolution uniformly, but this is computationally expensive and inefficient. Thus, we adopt in this study a local refinement strategy called Rivara's method [136] that bisects marked triangles while

keeping the resulting mesh conforming and well-conditioned. This method is used to locally refine regions that damage propagates into.

In this contribution, the implicit second-, fourth- and sixth-order gradient damage models are considered, since the inclusion of higher-order terms has the potential to accurately approximate the nonlocal solution, with minimal additional computational effort. Our solution algorithm initializes with the cylindrical arc-length control [30] and switches to a dissipation-based arc-length control [137] for better numerical stability as the damage evolves. Numerical examples demonstrate the benefits of using higher-order gradient damage models as well as the accuracy and ease of generalization into arbitrary high-order global smoothness in the use of the feature-preserving rational Bézier triangles. As a short summary, the novelty of the work presented in this paper is mainly threefold:

- The only work we can find that applied domain triangulation to study gradient damage models in an isogeometric setting is the work using PS triangles [110]. Besides the limitations of PS triangles discussed above, our approach is able to offer improved accuracy. The efficiency of the solution can be further improved by the use of the featuring-preserving meshing algorithm and the local refinement technique. The reason that feature-preserving meshing needs to be included is because damage is very likely to initiate at sharp curvatures or geometric imperfections due to stress concentration, and the feature-preserving meshing algorithm is extremely good at resolving small geometric features. Of course, the algorithm also provides a more accurate description of the geometry. A local refinement technique is included because usually very fine mesh is required to capture damage propagation, but it is computationally costly to uniformly refine the mesh. Most importantly, Bézier triangles are analogous to the

triangle elements in standard FEM and therefore a large number of existing tools can be directly applied to the discretization, such as the meshing tools in the pre-processing phase and Lagrange multipliers.

- The work of PS triangles is only able to include the fourth-order term in the damage formulation because it is C^1-continuous. The definition for C^2-continuous quintic PS-triangles [102] is completely different and also much more complicated. On the contrary, our method of using Lagrange multipliers to explicitly enforce higher-order continuity is straightforward. Our approach follows the same procedure irrespective of the order of continuity required. Moreover, any desired order of continuity can be obtained.
- The rational form of Bézier triangles is employed and therefore the geometry is exact in domains bounded by high-order NURBS curves (as can be seen in the third numerical example in this paper).

Generally speaking, our solution procedure [139] can be viewed as a unified modeling framework where the initial mesh provided by the feature-preserving meshing algorithm is able to capture damage initiation and early-stage damage growth, and the local refinement technique can be applied to adaptively refine the mesh in the direction of damage propagation, which can be computed from the early-stage damage growth.

5.2 Rivara's Method for Local Refinement

In addition to the automated mesh generation procedure employed in Section 4.3, we also needed a way to locally refine the mesh while keeping the mesh conforming and of high quality so that damage propagation could be modeled accurately and efficiently. In this study, we adopted the Rivara's method of bisecting triangles [136]. The algorithm bisects marked triangles as the

first step and then iteratively bisects non-conforming triangles and connects non-overlapping midpoints until the mesh becomes conforming. A pseudo-code is provided in Fig. 5-1.

Algorithm 1 Rivara's method of bisecting triangles for local refinement

1: **for all** marked triangles $\tau \in \mathbf{\Gamma}$ **do**
2: Bisect τ by the midpoint P of the longest edge.
3: **end do**
4: Find the set of non-conforming triangles $\tau_n \in \mathbf{\Gamma}_n$
5: **while** cardinality of $\mathbf{\Gamma}_n \neq 0$ **do**
6: Bisect τ_n by the midpoint Q of its longest side
7: **if** $P \neq Q$ **then**
8: Join P and Q
9: **end if**
10: Find the set of non-conforming triangles $\mathbf{\Gamma}_n$
11: **end do**

Figure 5-1: A pseudo-code for Rivara's method of bisecting triangles for local refinement

5.3 Higher-order Gradient Damage Formulation

5.3.1 Continuum Formulation

The gradient damage analysis is a coupled problem [126] where a diffusion equation representing the damage propagation needs to be solved in addition to the equilibrium equation. The stress equation can be written as

$$\frac{\partial \sigma_{ij}}{\partial x_i} = 0 \tag{5.1}$$

and is subjected to external Dirichlet boundary conditions $u_i = \bar{u}_i$ on $\partial\Omega_u$ and Neumann boundary conditions $\sigma_{ij} n_j = h_i$ on $\partial\Omega_h$.

In damage analysis, a scalar damage variable $\omega \in [0,1]$ is introduced to represent the damage growth, where $\omega = 0$ represents undamaged material and $\omega = 1$ fully damaged material. In particular, the constitutive model can be expressed as

$$\sigma_{ij} = (1-\omega) C_{ijkl} \varepsilon_{kl} \tag{5.2}$$

with C representing the elasticity tensor, and ε representing the infinitesimal strain tensor, i.e.,

$$\varepsilon_{ij} = \frac{1}{2}\left(\frac{\partial u_i}{\partial x_j} + \frac{\partial u_j}{\partial x_i} \right) \tag{5.3}$$

The damage variable ω can be fully determined by a monotonically increasing history parameter κ and is thus expressed as a function of it, $\omega = \omega(\kappa)$. The evolution of κ is guided by the Kuhn-Tucker conditions:

$$f \le 0, \ \dot{\kappa} \ \ge \ 0, \ \dot{\kappa} f \ = 0 \tag{5.4}$$

where f is the loading function, $f = \overline{\eta} - \kappa$, and $\overline{\eta}$ denotes the nonlocal equivalent strain. In continuum damage analysis, a local equivalent strain η is often used to compute the damage variable, which makes the model unable to diffuse damage out into its neighboring areas and therefore leads to a spurious mesh dependency issue. In contrast, the nonlocal equivalent strain $\overline{\eta}$ can be computed by averaging the local equivalent strain η over a predefined finite volume Ω

$$\overline{\eta}(x) = \frac{\int_{\hat{x} \in \Omega} g(x, \hat{x}) \eta(\hat{x}) d\hat{x}}{\int_{\hat{x} \in \Omega} g(x, \hat{x}) d\hat{x}} \tag{5.5}$$

where $g(x, \hat{x})$ represents the weighting function

$$g(x, \hat{x}) = \exp\left(-\frac{\left\| x - \hat{x} \right\|}{2 l_c^2} \right) \tag{5.6}$$

and l_c is the internal length parameter.

The Taylor expansion of the local equivalent strain η is often adopted to avoid a direct evaluation of the volume integral, specifically

$$\eta(\hat{x}) = \eta|_{\hat{x}=x} + \left.\frac{\partial \eta}{\partial \hat{x}_i}\right|_{\hat{x}=x} (\hat{x}_i - x_i) + \frac{1}{2}\left.\frac{\partial^2 \eta}{\partial \hat{x}_i \partial \hat{x}_j}\right|_{\hat{x}=x} (\hat{x}_i - x_i)(\hat{x}_j - x_j) + \mathrm{O}\left((\hat{x}_i - x_i)^3\right) \tag{5.7}$$

Substituting Eq. (5.7) into Eq. (5.5) and assuming that the integral ranges from negative infinity to infinity lead to an explicit gradient approximation of the nonlocal equivalent strain

$$\overline{\eta}(x) = \eta(x) + \frac{1}{2} l_c^2 \frac{\partial^2 \eta(x)}{\partial x_i^2} + \frac{1}{8} l_c^4 \frac{\partial^4 \eta(x)}{\partial x_i^2 \partial x_j^2} + \frac{1}{48} l_c^6 \frac{\partial^6 \eta(x)}{\partial x_i^2 \partial x_j^2 \partial x_k^2} + \cdots \tag{5.8}$$

Eq. (5.8) requires C^1 continuity for the inclusion of the second-order term and C^2 continuity for the inclusion of the fourth-order term, and is therefore not suitable for standard FEA. Alternatively, one can obtain an implicit gradient formulation by differentiation and multiplication of Eq. (5.8)

$$\eta(x) = \overline{\eta}(x) - \frac{1}{2} l_c^2 \frac{\partial^2 \overline{\eta}(x)}{\partial x_i^2} + \frac{1}{8} l_c^4 \frac{\partial^4 \overline{\eta}(x)}{\partial x_i^2 \partial x_j^2} - \frac{1}{48} l_c^6 \frac{\partial^6 \overline{\eta}(x)}{\partial x_i^2 \partial x_j^2 \partial x_k^2} + \cdots \tag{5.9}$$

As one can see, only C^0 continuity is required for the inclusion of the second-order gradient term. Thus, second-order gradient damage model is suitable in the context of standard FEA, but the accuracy of the numerical solution suffers. In this contribution, we adopt higher-order gradient damage models by the inclusion of the fourth-order and sixth-order terms in Eq. (5.9).

Eq. (5.1) and Eq. (5.9) constitute the govern equations for the higher-order gradient damage problem. The weak form can be derived by multiplying a perturbation term δu_j and $\delta\overline{\eta}$ to Eq. (5.1) and Eq. (5.9), respectively, and integrating by parts over the space of interest Ω

$$\int_{\Omega} \frac{\partial \delta u_i}{\partial x_j} \sigma_{ij} dV = \int_{\partial \Omega_h} \delta u_i h_i dA \tag{5.10}$$

$$\int_{\Omega} \delta\overline{\eta}\,\overline{\eta} + \frac{1}{2} l_c^2 \frac{\partial \delta\overline{\eta}}{\partial x_i} \frac{\partial \overline{\eta}}{\partial x_i} + \frac{1}{8} l_c^4 \frac{\partial^2 \delta\overline{\eta}}{\partial x_i \partial x_j} \frac{\partial^2 \overline{\eta}}{\partial x_i \partial x_j} + \frac{1}{48} l_c^6 \frac{\partial^3 \delta\overline{\eta}}{\partial x_i \partial x_j \partial x_k} \frac{\partial^3 \overline{\eta}}{\partial x_i \partial x_j \partial x_k} dV = \int_{\partial \Omega_h} \delta\overline{\eta}\,\eta dV$$

5.3.2 Discretized Form

Based on the Delaunay-based triangulation from Section 2, the space of interest can be discretized into n elements. For each element, the displacement u, the nonlocal equivalent strain $\overline{\eta}$ and the derivatives can be expressed in terms of the Bézier basis functions R and the deformation of the corresponding control points. In particular,

$$u = \mathbf{R}_u \mathbf{u},\ \varepsilon = \mathbf{B}_u \mathbf{u},\ \overline{\eta} = \mathbf{R}_{\overline{\eta}} \overline{\boldsymbol{\eta}},\ \frac{\partial \overline{\eta}}{\partial x_i} = \mathbf{B}_{\overline{\eta}} \overline{\boldsymbol{\eta}},\ \frac{\partial^2 \overline{\eta}}{\partial x_i \partial x_j} = \mathbf{B}_{\overline{\eta}\overline{\eta}} \overline{\boldsymbol{\eta}},\ \frac{\partial^3 \overline{\eta}}{\partial x_i \partial x_j \partial x_k} = \mathbf{B}_{\overline{\eta}\overline{\eta}\overline{\eta}} \overline{\boldsymbol{\eta}} \tag{5.11}$$

For the terms in Eq. (5.11), the following definitions hold:

$$u = \begin{bmatrix} u_x & u_y \end{bmatrix}^T,\ \varepsilon = \begin{bmatrix} \varepsilon_{xx} & \varepsilon_{yy} & 2\varepsilon_{xy} \end{bmatrix}^T,\ \frac{\partial \overline{\eta}}{\partial x_i} = \begin{bmatrix} \frac{\partial \overline{\eta}}{\partial x} & \frac{\partial \overline{\eta}}{\partial y} \end{bmatrix}^T,$$

$$\frac{\partial^2 \overline{\eta}}{\partial x_i \partial x_j} = \begin{bmatrix} \frac{\partial^2 \overline{\eta}}{\partial x^2} & \frac{\partial^2 \overline{\eta}}{\partial y^2} & \sqrt{2} \frac{\partial^2 \overline{\eta}}{\partial x \partial y} \end{bmatrix}^T,$$

$$\frac{\partial^3 \overline{\eta}}{\partial x_i \partial x_j \partial x_k} = \begin{bmatrix} \frac{\partial^3 \overline{\eta}}{\partial x^3} & \frac{\partial^3 \overline{\eta}}{\partial y^3} & \sqrt{3} \frac{\partial^3 \overline{\eta}}{\partial x^2 \partial y} & \sqrt{3} \frac{\partial^3 \overline{\eta}}{\partial x \partial y^2} \end{bmatrix}^T,$$

$$\mathbf{R}_u = \begin{bmatrix} \mathbf{R} & \mathbf{0} \\ \mathbf{0} & \mathbf{R} \end{bmatrix},\ \mathbf{B}_u = \begin{bmatrix} \frac{\partial \mathbf{R}}{\partial x} & \mathbf{0} & \frac{\partial \mathbf{R}}{\partial y} \\ \mathbf{0} & \frac{\partial \mathbf{R}}{\partial y} & \frac{\partial \mathbf{R}}{\partial x} \end{bmatrix}^T,\ \mathbf{R}_{\overline{\eta}} = \mathbf{R},\ \mathbf{B}_{\overline{\eta}} = \begin{bmatrix} \frac{\partial \mathbf{R}}{\partial x} & \frac{\partial \mathbf{R}}{\partial y} \end{bmatrix}^T, \tag{5.12}$$

$$\mathbf{B}_{\bar{\eta}\bar{\eta}} = \left[\frac{\partial^2 \mathbf{R}}{\partial x^2} \quad \frac{\partial^2 \mathbf{R}}{\partial y^2} \quad \sqrt{2}\frac{\partial^2 \mathbf{R}}{\partial x \partial y} \right]^T, \mathbf{B}_{\bar{\eta}\bar{\eta}\bar{\eta}} = \left[\frac{\partial^3 \mathbf{R}}{\partial x^3} \quad \frac{\partial^3 \mathbf{R}}{\partial y^3} \quad \sqrt{3}\frac{\partial^3 \mathbf{R}}{\partial x^2 \partial y} \quad \sqrt{3}\frac{\partial^3 \mathbf{R}}{\partial x \partial y^2} \right]^T$$

Substitution of the discretized form into Eq. (5.10) results in the weak form

$$\begin{aligned} &\delta \mathbf{u}^T \left(\int_\Omega \mathbf{B}_u^T (1-\omega) \mathbf{C} \mathbf{B}_u dV \mathbf{u} - \int_{\partial \Omega_h} \mathbf{R}_u^T \mathbf{h} dA \right) = 0 \\ &\delta \bar{\boldsymbol{\eta}}^T \left(\int_\Omega \mathbf{R}_{\bar{\eta}} \mathbf{R}_{\bar{\eta}}^{\ T} + \frac{l_c^2}{2} \mathbf{B}_{\bar{\eta}}^T \mathbf{B}_{\bar{\eta}} + \frac{l_c^4}{8} \mathbf{B}_{\bar{\eta}\bar{\eta}}^T \mathbf{B}_{\bar{\eta}\bar{\eta}} + \frac{l_c^6}{48} \mathbf{B}_{\bar{\eta}\bar{\eta}\bar{\eta}}^T \mathbf{B}_{\bar{\eta}\bar{\eta}\bar{\eta}} dV \bar{\boldsymbol{\eta}} - \int_\Omega \mathbf{R}_{\bar{\eta}} \eta dV \right) = 0 \end{aligned} \tag{5.13}$$

Eq. (5.13) is essentially the discretized form of the governing equation for the implicit sixth-order gradient damage model. To solve this, we employ the cylindrical arc-length control [30] to initialize the solution procedure due to the existence of a load-shedding behavior when significant damage occurs. As damage evolves, our solution algorithm switches to a dissipation-based arc-length control [137] for better numerical stability, as the dissipated energy term is always positive once damage happens, which is an obvious conclusion from the second law of thermodynamics.

5.4 Numerical Examples

In this section, a number of numerical examples with different damage laws are demonstrated, including a beam under three-point bending, an L-shaped domain, and an L-shaped domain with a curved inside corner. For all problems, we employ a 28-point quadrature rule for integration over the triangle, and a 5-point quadrature rule for integration over the edges. We also use quintic elements in order to impose higher-order continuity. The solutions are compared with nonlocal solutions and other results from existing literature.

5.4.1 Three-point Bending Beam (TPBB)

In the first example, we consider a three-point bending beam [138] as shown in Fig. 5-2. The beam is simply supported and is subjected to a distributed load at the mid-span. The thickness of the beam is $t = 50mm$. The Young's modulus is $E = 20GPa$ and Poisson's ratio is $\nu = 0.2$. A state of plane strain is assumed.

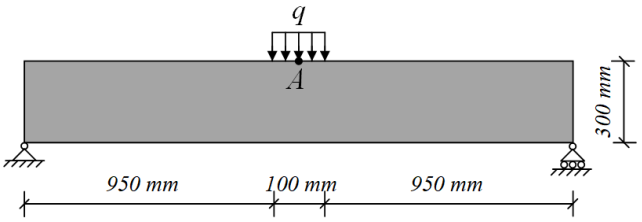

Figure 5-2: The setup of the three-point bending beam

The local equivalent strain is defined as

$$\eta(\varepsilon) = \sqrt{\langle \varepsilon_i \rangle^2} = \sqrt{\langle \varepsilon_1 \rangle^2 + \langle \varepsilon_2 \rangle^2} \tag{5.14}$$

where ε_i denotes the principal strain and $\langle \cdot \rangle$ is the Macaulay bracket, i.e., $\langle x \rangle = \max(x, 0)$. The damage law employed in this example is

$$\omega(\kappa) = \begin{cases} 0 & \kappa \le \kappa_0 \\ 1 - \dfrac{\kappa_0}{\kappa}\left(1 - \alpha + \alpha \exp(\beta(\kappa_0 - \kappa))\right) & \kappa > \kappa_0 \end{cases} \tag{5.15}$$

where $\kappa_0 = 1 \times 10^{-4}$, $\alpha = 0.99$ and $\beta = 500$. The internal length parameter is set to $l_c = 20mm$.

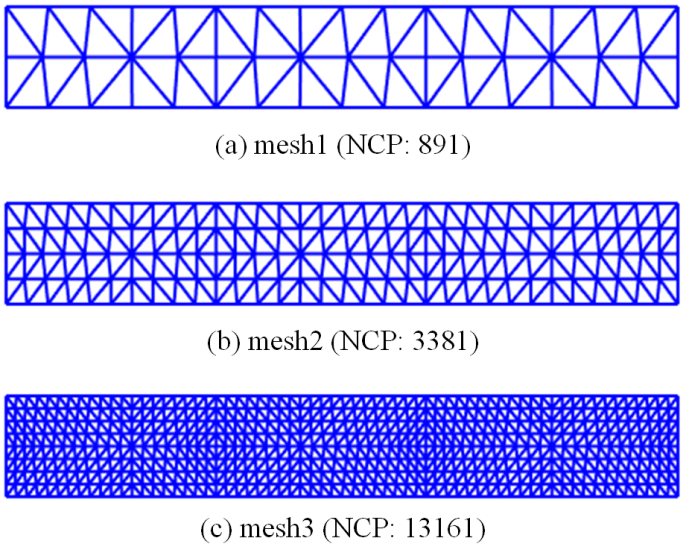

Figure 5-3: Different uniform meshes for TPBB

First, we investigate the behavior of gradient damage model with uniform mesh refinement (see meshes 1, 2, and 3 in Fig. 5-3). We consider three mesh cases, with mesh2 being the 4-split of mesh1 and mesh3 being the 4-split of mesh2. The force-displacement curves of the different-order gradient damage formulations for convergence study are plotted in Fig. 5-4, where a comparison to the nonlocal solution [138] is also provided. In our plots, the force is taken as the resultant force of the distributed load, and the displacement is measured at the point *A* of Fig. 5-2. In Figs. 9a, 9b, and 9c, results are shown respectively for the second-order (O=2), fourth-order (O=4) and sixth-order (O=6) gradient damage models for each mesh. It can be seen that the inclusion of higher-order terms in the gradient formulation leads to a more accurate solution if the mesh is suitably fine (i.e., mesh2 or mesh3). In Fig. 5-4c, it appears that the higher-order damage model requires a more refined mesh, as evidenced by the fact that mesh1 and mesh2 have a larger deviation from mesh3 than in O=2 and O=4. In Fig. 5-5, results for O=2, 4, 6 are shown only for the finest mesh (i.e, mesh3), and it is clear that including the higher-order terms leads to convergence to the published solution.

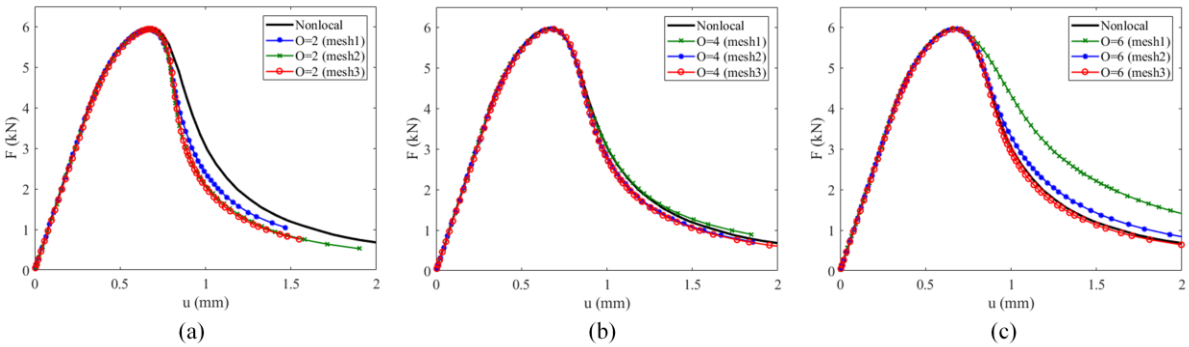

Figure 5-4: Force-displacement curves for the convergence of the (a) second-order (O=2), (b) fourth-order (O=4), and (c) sixth-order (O=6) gradient damage models for the three meshes considered.

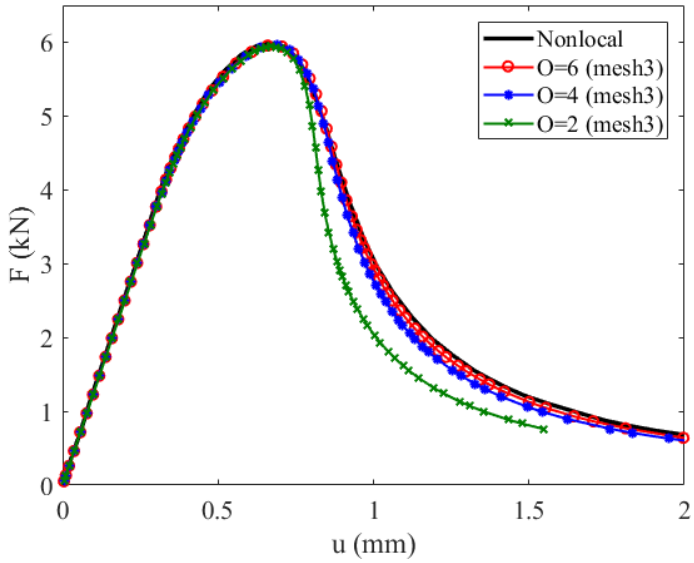

Figure 5-5: Force-displacement curves of the second-, fourth- and sixth-order gradient damage models in the case of mesh3

Based on the analysis, it is clear that a fine mesh is needed to reach convergence, but it is also worth mentioning that it is computationally expensive to uniformly refine the entire domain (e.g., Fig. 5-3). Therefore, Rivara's method was applied to locally refine the region under the distributed load, with the region refined taken as $x \in [750,1250]$. The resulting mesh is illustrated in Fig. 5-6, where the number of control points (NCP) equal to 4511.

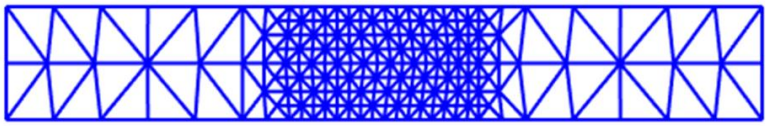

Figure 5-6: Locally refined TPBB (NCP: 4511)

The force-displacement curves obtained with the locally refined mesh (LRM) are provided in Fig. 5-7, along with a comparison to the nonlocal and sixth-order gradient damage solution with a non-uniform NURBS mesh from [138]. We observe an obvious improvement in terms of accuracy with the inclusion of higher-order terms in the gradient enhanced formulation. The inclusion of the sixth-order term in the gradient damage formulation is observed to be effective, as it provides a closer solution to the nonlocal one and the additional computational effort is negligible. We can also see that our solution reaches the same level of accuracy but with the required NCP cut by half. Thus, we conclude that our solution is both accurate and efficient.

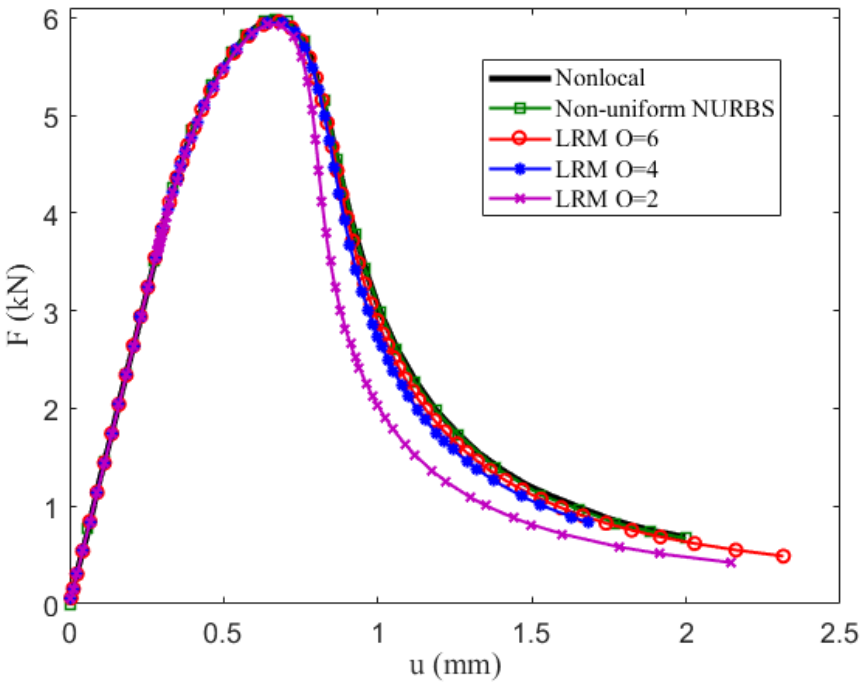

Figure 5-7: Force-displacement curve obtained with the sixth-order gradient damage model and the locally refined mesh (LRM) from Fig. 5-6 (NCP: 4511).

The damage propagation over time is also accurately captured, as shown in Fig. 5-8. Our model is able to capture the damage propagation up to the ultimate failure of the beam, which corresponds to the fourth plot in Fig. 5-8.

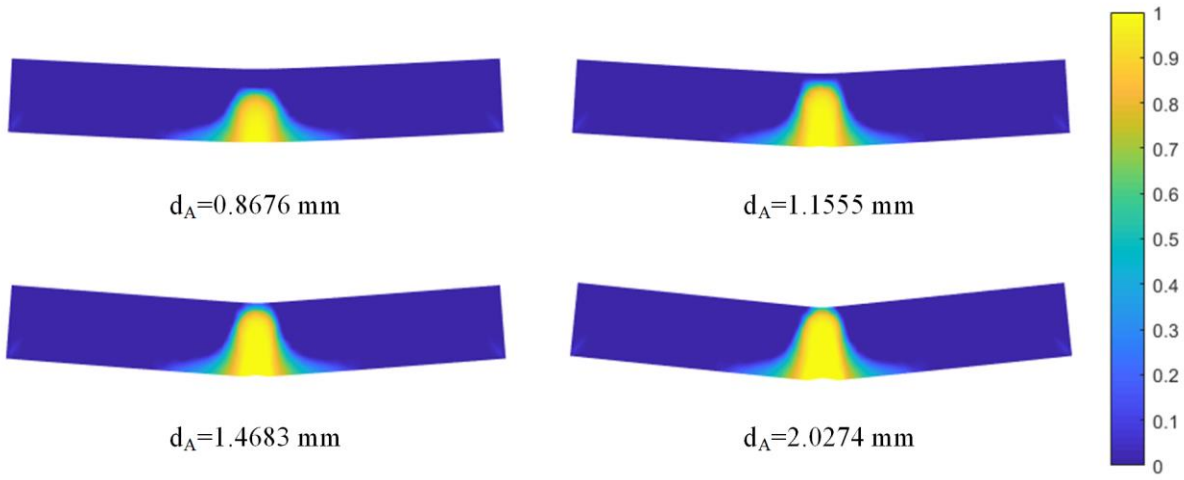

Figure 5-8: Time evolution of the damage propagation in TPBB

5.4.2 L-shaped Domain

As the second numerical example, we consider the classical L-shaped domain problem [110,126]. The setup of the problem is shown in Fig. 5-9. The thickness of the plate is $t = 200mm$. The material is linear elastic, with the Young's modulus $E = 10GPa$ and Poisson's ratio is $\nu = 0.2$. Plane stress condition is assumed.

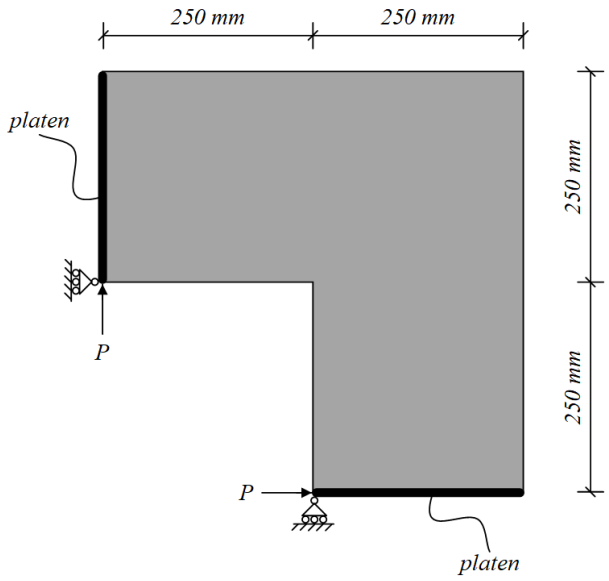

Figure 5-9: The setup of the L-shaped domain

The rotation-free ends (i.e., the two platens) of the plate are enforced through the inclusion of the following linear constraints in the form of Lagrange multipliers:

$$\mathbf{u}_p = \left(1 - \frac{\mathbf{x}_p - \mathbf{x}_a}{\mathbf{x}_b - \mathbf{x}_a}\right)\mathbf{u}_a + \frac{\mathbf{x}_p - \mathbf{x}_a}{\mathbf{x}_b - \mathbf{x}_a}\mathbf{u}_b \tag{5.16}$$

where $\mathbf{u}_a$, $\mathbf{u}_b$ and $\mathbf{u}_p$ are the displacements of the two ends and any material point on the platen, respectively.

The modified von Mises local equivalent strain is employed and defined as

$$\eta(\varepsilon) = \frac{k-1}{2k(1-2\nu)} I_1(\varepsilon) + \frac{1}{2k}\sqrt{\left(\frac{k-1}{1-2\nu} I_1(\varepsilon)\right)^2 + \frac{12k}{(1+\nu)^2} J_2(\varepsilon)} \tag{5.17}$$

where $I_1(\varepsilon)$ is the first invariant of the strain tensor

$$I_1(\varepsilon) = \varepsilon_{ii} \tag{5.18}$$

$J_2(\varepsilon)$ is the second invariant of the deviatoric strain tensor

$$J_2(\varepsilon) = \frac{1}{2}\varepsilon_{ij}\varepsilon_{ij} - \frac{1}{6}(I_1(\varepsilon))^2 \tag{5.19}$$

and k is a parameter that takes into account the variation in strength between compression and tension. In this problem, $k = 10$.

The same damage law given in Eq. (5.15) is used, but with the parameters set to $\kappa_0 = 4 \times 10^{-4}$, $\alpha = 0.98$ and $\beta = 80$. The internal length parameter is set to $l_c = 5\sqrt{2}mm$.

In order to save computational effort, we apply Rivara's method directly to locally refine the region where damage initiates and propagates (i.e., the diagonal area). Fig. 5-10 shows the resulting mesh after applying Rivara's method five times to the region bounded by the two straight lines $y \geq x - 75$ and $y \leq x + 75$, where the inside corner is taken as the origin.

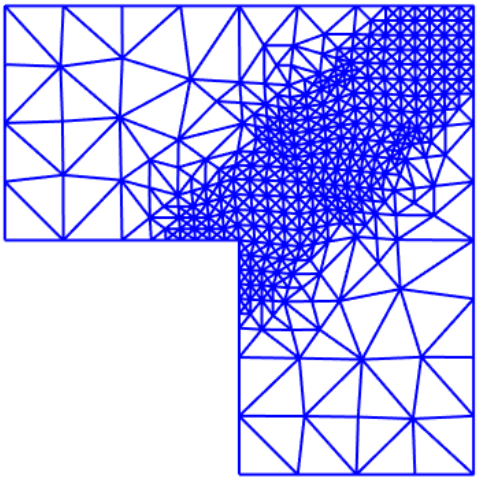

Figure 5-10: The resulting mesh of the L-shaped domain after applying Rivara's method five times (NCP: 12631).

The force-displacement curves are plotted in Fig. 5-11, along with the solutions from literature using T-splines [126] and Powell-Sabin (PS) triangles [110]. The displacement is measured at the point (and in the direction) of the applied load. In this problem, we use the nonlocal solution using T-splines as our reference solution. By comparing our solutions with different order gradient

formulations on the locally refined mesh (LRM), we observe a notable improvement in terms of accuracy with the inclusion of higher-order terms. By comparing to the results of the fourth-order gradient damage formulation, our solution appears to be more accurate than the one obtained using PS triangles. In terms of NCP, the solution using PS triangles employs 26,463 control points, whereas our LRM only has 12,631 control points, which represents significant computational saving. It is also worth noting that it is very easy to include the sixth-order term of the Taylor expansion with our modeling approach, compared to C^2-continuous quintic PS triangles [102] where the definition is completely different from the C^1-continuous quadratic PS triangles.

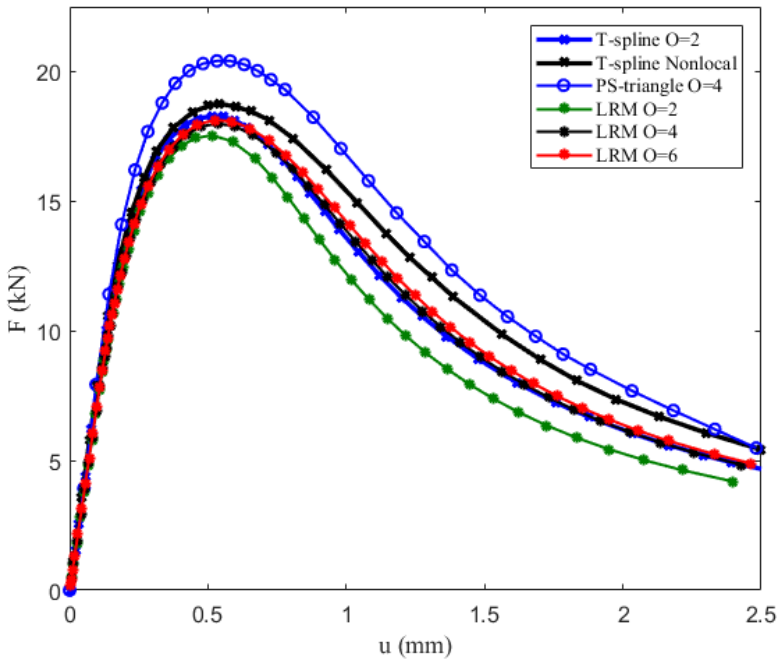

Figure 5-11: The force-displacement curves of the L-shaped domain

To better demonstrate the accuracy of the proposed method, the contour plots for the damage propagation and the maximum principal stress distribution at $u = 1.95mm$ are illustrated in Fig. 5-12.

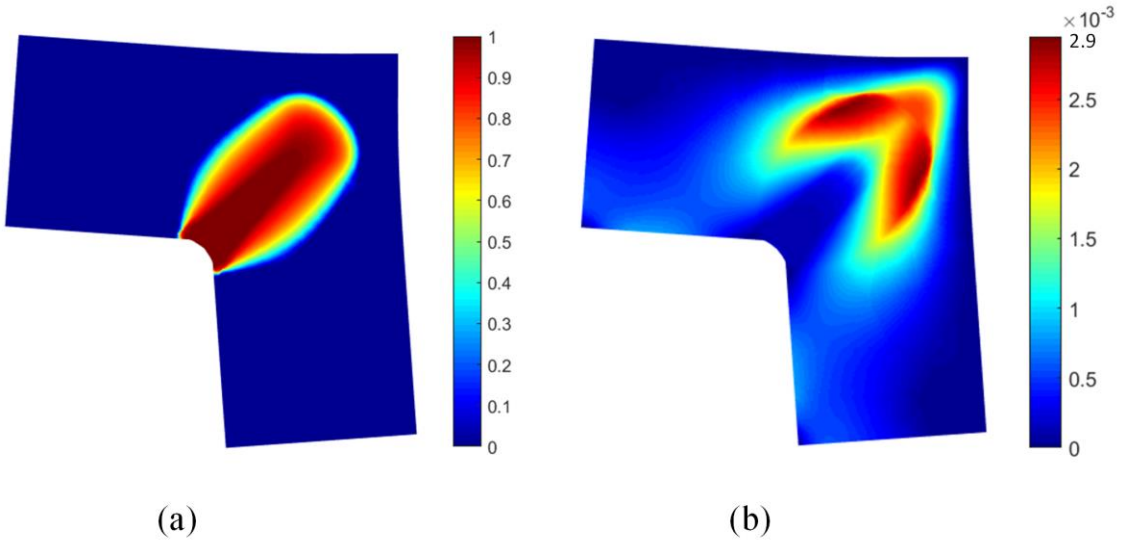

Figure 5-12: Control plot for the L-shaped domain at $u = 1.95mm$ (the deformation is amplified by a factor of 20): (a) damage propagation and (b) maximum principal stress distribution

5.4.3 L-shaped Domain with Curved Inside Corner

For the third example, only a slight change is made to the classical L-shaped domain problem, with the inside corner being curved instead of at a right angle (see Fig. 5-13). The purpose of this example is to investigate the behavior of the Delaunay-based feature-preserving triangulation on capturing damage initiation and the early stage of damage propagation. The material properties and damage law are the same as in the second numerical example. The sixth-order gradient damage formulation is used.

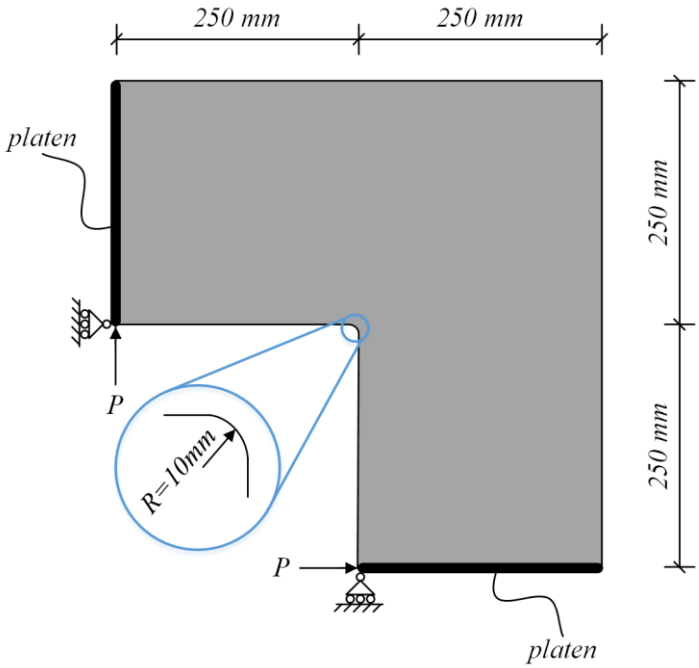

Figure 5-13: The setup of the L-shaped domain with curved inside corner

The resulting mesh from the feature-preserving triangulation algorithm is compared to the initial mesh of the classical L-shaped domain without applying local refinement techniques (see Fig. 5-14). As we can see, the inside corner is resolved with high resolution (Fig. 5-14(b)).

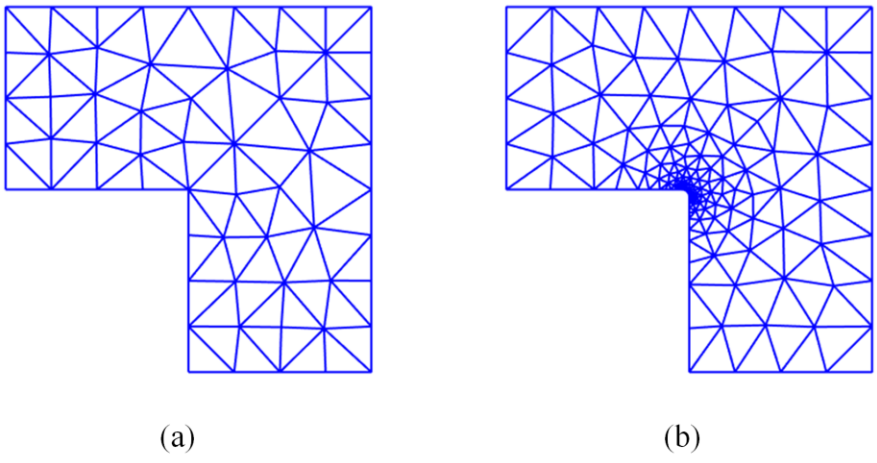

Figure 5-14: The effect of the feature-preserving triangulation: (a) the initial mesh of the classical L-shaped domain, and (b) the feature-preserving triangulation for the L-shaped domain with curved inside corner

The force-displacement curves obtained from the above two mesh cases are plotted in Fig. 5-15. In comparison to the result obtained using the Mesh in Fig. 5-14(a), we observe a more accurate

prediction of the solution for the entire deformation path using the mesh in Fig. 5-14(b), especially in the damage initiation phase as indicated by the onset of yielding. The feature-preserving mesh is capable of providing a very accurate solution up to around $u = 0.4mm$, after which the damage propagates into the relatively coarse mesh region and locally refinement as shown in the second numerical example is needed. In general, the feature-preserving triangulation can be used to predict early-stage damage growth, and adaptive meshing can be adopted to refine the direction of damage propagation.

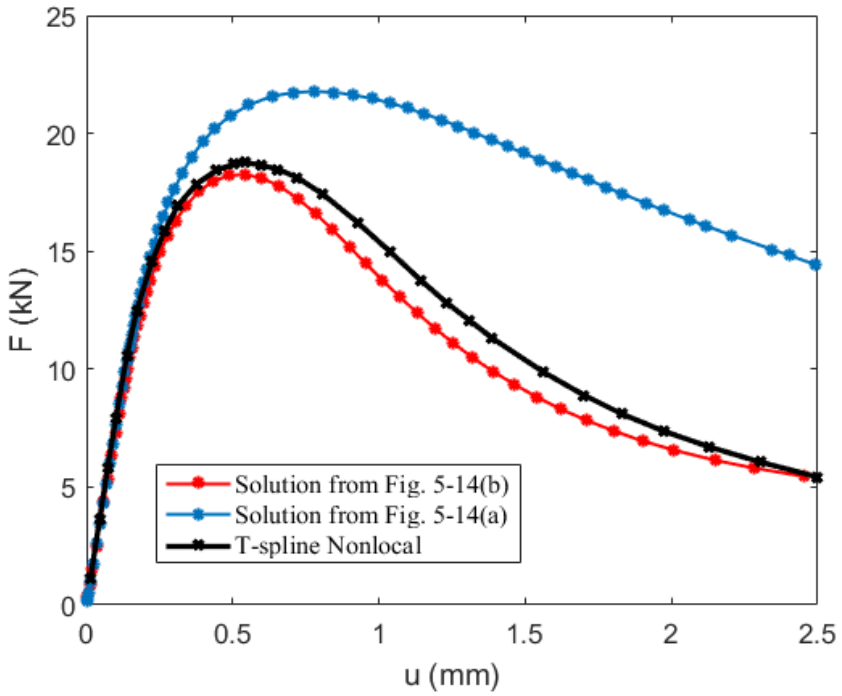

Figure 5-15: The force-displacement curves obtained using the two mesh cases in Fig. 5-14

The contour plots of damage growth at $u = 0.43mm$, $u = 0.90mm$ and $u = 1.25mm$ are also provided in Fig. 5-16 for a better illustration of the ability of the feature-preserving triangulation in capturing the early stage of damage growth.

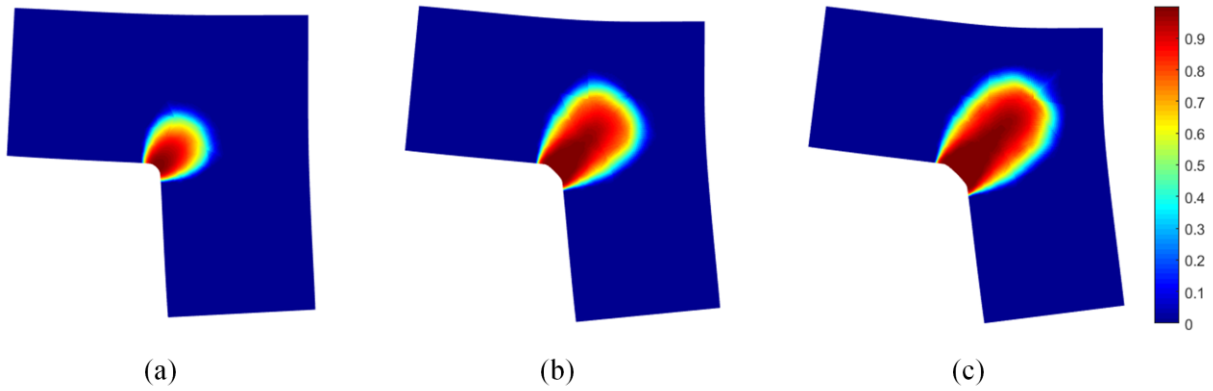

Figure 5-16: The contour plots of damage growth in the L-shaped domain with curved inside corner (deformation is amplified by a factor of 50) at (a) $u = 0.43mm$, (b) $u = 0.90mm$ and (c) $u = 1.25mm$

5.5 Conclusion

The Delaunay-based feature-preserving rational Bézier triangles are a powerful tool in modeling smeared damage, especially in cases where geometrically complicated domains are involved. They not only circumvent the reduced continuity problem at NURBS patch interfaces or at extraordinary points in T-splines, but they also increase the flexibility in discretization. As is indicated in the third numerical example, a general modeling approach can be constructed where the Delaunay-based feature-preserving triangulation can be used to resolve the geometry and predict the damage growth at an early stage. As the damage propagates, a suitable local refinement technique such as the Rivara's method can be employed to further refine the mesh in the direction of damage propagation. Moreover, the use of Lagrange multipliers makes it possible to impose higher-order continuity constraints to the resulting mesh. In terms of the formulation of implicit gradient damage models, the inclusion of higher-order terms leads to a better prediction of the damage path, while the additional computational effort is negligible. The accuracy and efficiency of the proposed modeling approach are verified by a number of numerical examples, where superiority is observed over other domain triangulation methods such as Powell-Sabin triangles.

It must be mentioned that domain triangulation is not undisputedly advantageous over quadrilateral meshing techniques (e.g., T-splines). An obvious drawback of domain triangulation methods is the fact that typically high-order polynomials (e.g., quartic and quintic) have to be used in order to impose higher-order global smoothness. This also holds true for other triangulation methods such as Powell-Sabin splines. In contrast, C^2 continuity can be easily achieved with cubic NURBS/T-splines.

Chapter 6 Conclusion

The computational approaches for addressing various problems in structural engineering and improving the accuracy and efficiency in solutions in the framework of IGA were presented here. The work can be mainly categorized into two parts based on the use of spline basis functions (i.e., NURBS and rational Bézier triangles). A number of merits related to IGA were also achieved including the geometrically exact description of the models, rotation-free formulation, and high-order smoothness.

On the one hand, the use of NURBS was applied to study large-deformation structural frames and advanced material systems such as a sandwich plate with a functionally graded material core. The appropriate rotation-free formulations were derived. In the analysis of large-deformation structural frames, a layer-based discretization was adopted for the prediction of the spread of plasticity and the deformation was captured in an adaptive manner. In the analysis of laminated composites, a layerwise theory was employed that was capable of predicting the full 3D stress states while maintaining a 2D data structure.

On the other hand, rational Bézier triangles were coupled with a Delaunay-based feature-preserving discretization algorithm and a local refinement technique for the analysis of geometrically complex Kirchhoff plates and implicit higher-order gradient damage models. Lagrange multipliers were leveraged to enforce high-order continuity in an explicit fashion. The static and dynamic response of geometrically complex Kirchhoff plates and the performance of implicit higher-order gradient damage models were investigated and satisfactory results were observed.

6.1 NURBS for the Analysis of Structural Frames and Laminated Composite Plates

As shown in Chapter 2, a 2D distributed plasticity IGA frame element was formulated. The derivation employed a layer-based discretization in the through-thickness direction and considered member-level geometrically nonlinear effects through the inclusion of high-order terms in the strain expression. Moreover, the formulation was also extended to multi-patch analysis via the introduction of continuity constraints between two adjacent patches, thus allowing for a rigid connection of members in frame structures. The model closely represents reality as plastic hinges form in the beams or columns rather than at a fictitious joint region, which is rather important from a structural point of view. The formulation was also presented for adaptive analysis. Lobatto quadrature was employed in order to capture the onset of yielding at the ends of the member, and a knot insertion technique was introduced to capture the change in curvature associated with the formation of a plastic hinge. A number of numerical examples including the yielding of beams and frames subjected to monotonic and cyclic loading conditions were used to test the proposed model and significant computational saving was obtained.

In Chapter 3, an IGA layerwise plate model was derived for the analysis of composite laminates and sandwich plates embedding a functionally graded material core. The proposed model assumed a separate displacement field expansion within each layer and used the knot insertion technique to enforce the C^0-continuity at layer interfaces. Due to the fact that the through-thickness integration were carried out separately from the in-plane surface integration, the proposed model was able to capture the full 3D stress states while maintaining a 2D data structure. The modeling of several numerical examples comprised of advanced materials was illustrated with high accuracy.

6.2 Rational Bézier Triangles for the Solution of Geometrically Complex Kirchhoff Plates and Implicit Higher-order Gradient Damage Models

In Chapter 4, the rational Bézier triangle technique was coupled with a Delaunay-based feature-preserving meshing technology to study geometrically complex Kirchhoff plates. The replacement of control points at domain boundaries yielded a geometrically exact description of the model to be analyzed. By resorting to the Lagrange multipliers, the global continuity of the triangulation was raised to C^1, which is suitable for Kirchhoff plate analysis. Numerical examples comprised of static bending and free vibration analysis of plates bounded by high-order NURBS curves verify the accuracy and efficiency of the proposed modeling approach.

Chapter 5 demonstrated the use of the feature-preserving rational Bézier triangles in modeling smeared damage. A general modeling framework was proposed where the Delaunay-based feature-preserving triangulation can be used to resolve the geometry and predict the damage growth at an early stage. As the damage propagates, a suitable local refinement technique such as the Rivara's method can be employed to further refine the mesh in the direction of damage propagation. In the formulation of implicit gradient damage models, the inclusion of higher-order terms led to a better prediction of the damage path, while the additional computational effort was negligible. The accuracy and efficiency of the proposed modeling approach were verified by a number of numerical examples, where superiority was observed over other domain triangulation methods such as Powell-Sabin triangles.

6.3 Limitations and Future Work

The IGA rotation-free frame model presented for capturing the spread of plasticity was developed in Chapter 2 of the dissertation. One limitation of this model is the fact that the formulation is presently limited to problems with moderate displacements. For use in large-

displacement analysis, the frame model would need to be extended to consider system-level geometrically nonlinear effects. A second limitation is that the number of layers (i.e., fibers) in the through-thickness direction was held fixed. To achieve additional computational saving, an adaptive analysis to automatically define the number of layers for each element should be considered. Additionally, the paper only consider a 2D structural response. Additional work would be needed to determine if the formulation, which relies on constraints to impose rotational fixity, would work in 3D.

For the IGA laminated composite plate project, situations that commonly occurs in laminated composite materials such as delamination and crack opening are not addressed in the current model. Therefore, future work should consider enabling the formulation to predict the full 3D states of stress of delaminated composites.

To this point, both of the aforementioned projects were based on the representation using NURBS. The drawbacks of the tensor-product structure of NURBS have already been discussed in Chapter 1. Therefore, future research should also consider the use of more advanced spline functions for analysis.

In the second part of the dissertation where rational Bézier triangles serve as the major tool for discretization, the analysis is limited to two dimensions. Future research directions should include extending the work to three dimensions by using tetrahedral elements in the framework of IGA. As it is difficult to recover exact boundary in 3D, weak enforcement of the bounding surfaces can be considered such as using tetrahedral finite cell method. In addition, a further concern is the fact that the feature-preserving discretization technique that were discussed in Chapter 4 may not be able to resolve regions of damage initiation in all cases (e.g., the classic L-shaped domain problem). Therefore, future work could consider developing more robust discretization techniques

that allow the users to capture the onset of damage accurately and efficiently. Last but not least, the current work only involves the modeling of smeared damage. Future work should also apply the rational Bézier triangle technique to study discrete fracture models, where the author believes that rational Bézier triangles should outperform other triangulation approaches such as PS triangles because of the limitation of PS B-splines as discussed in Chapter 5.

Appendix A

The problem considered for the convergence study here is the classic infinite plate with a circular hole problem, which is modeled using a finite quarter of the plate due to symmetry. The problem setup can be found in Fig. A-1, where the plate is subjected to a constant in-plane tension. A state of plane stress is assumed for this problem.

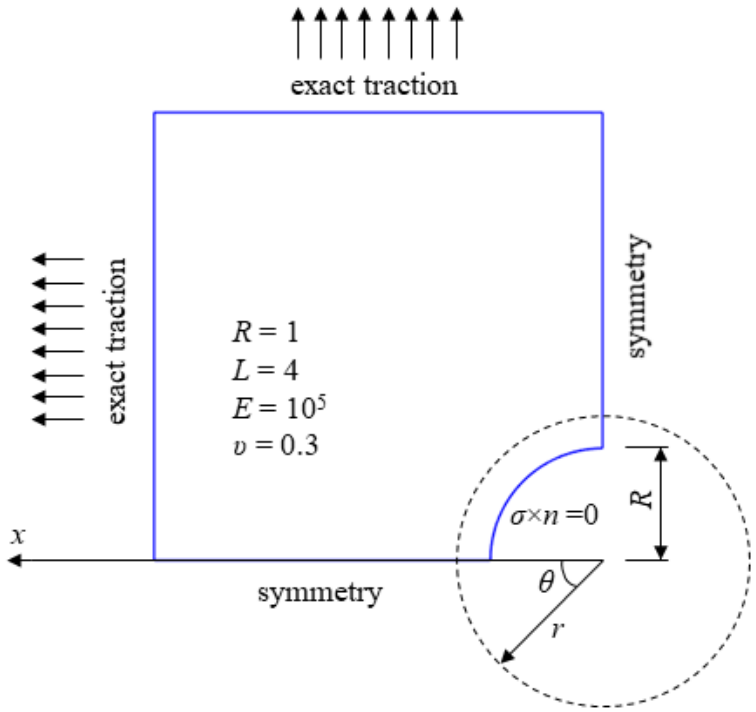

Figure A-1: The infinite plate with a circular hole: problem setup

The exact solution [1] is available for comparison, which is reproduced here for convenience.

$$\sigma_{xx}(r,\theta) = 1 - \frac{R^2}{r^2}\left(\frac{3}{2}\cos 2\theta + \cos 4\theta\right) + \frac{3}{2}\frac{R^4}{r^4}\cos 4\theta$$

$$\sigma_{yy}(r,\theta) = -\frac{R^2}{r^2}\left(\frac{1}{2}\cos 2\theta - \cos 4\theta\right) - \frac{3}{2}\frac{R^4}{r^4}\cos 4\theta \tag{A1}$$

$$\sigma_{xy}(r,\theta) = -\frac{R^2}{r^2}\left(\frac{1}{2}\sin 2\theta + \sin 4\theta\right) + \frac{3}{2}\frac{R^4}{r^4}\sin 4\theta$$

with (r,θ) the polar coordinates whose origin is at the center of the plate.

The plate is discretized with tensor-product NURBS in Fig. A-2, where the exact geometry can be described with only two elements in mesh1 (see Fig. A-2(b)).

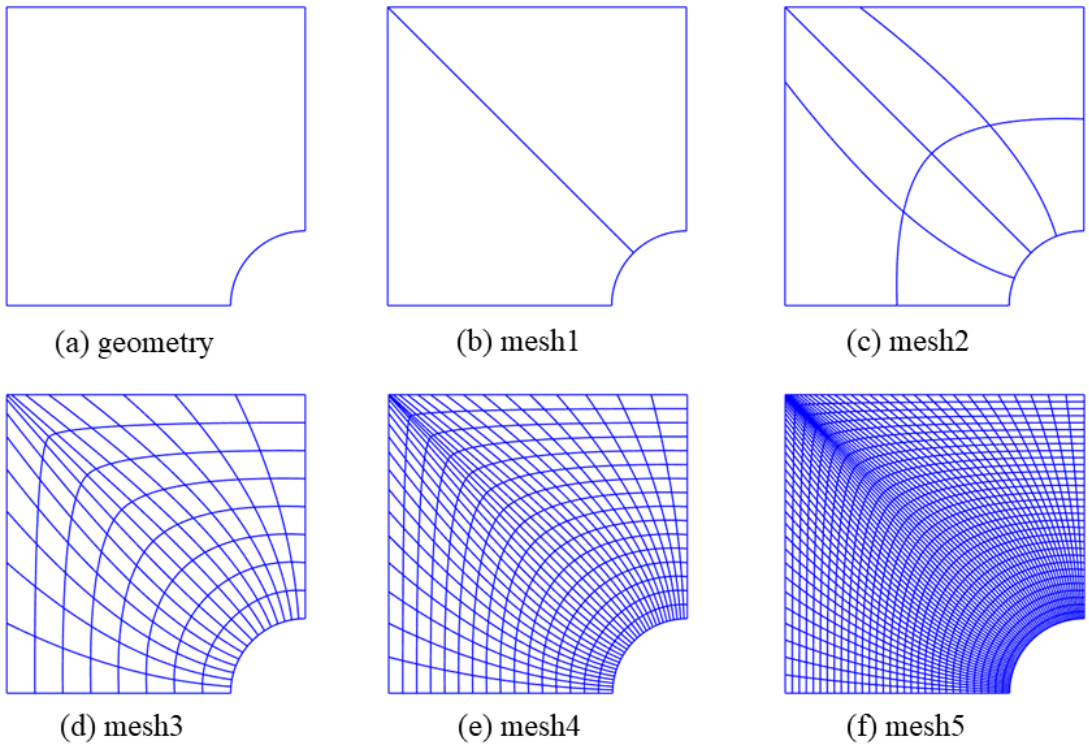

Figure A-2: Different meshes of the plate with a circular hole generated via *h*-refinement

The contour plots of the displacement in x direction and stress σ_{xx} obtained using mesh3, mesh4 and mesh5 and bi-quadratic NURBS are illustrated in Fig. A-3 and Fig. A-4. We observe that the stress concentration at the point $\left(R, \frac{3\pi}{2}\right)$ is predicted very well and a very smooth stress field can be captured as the mesh gets refined.

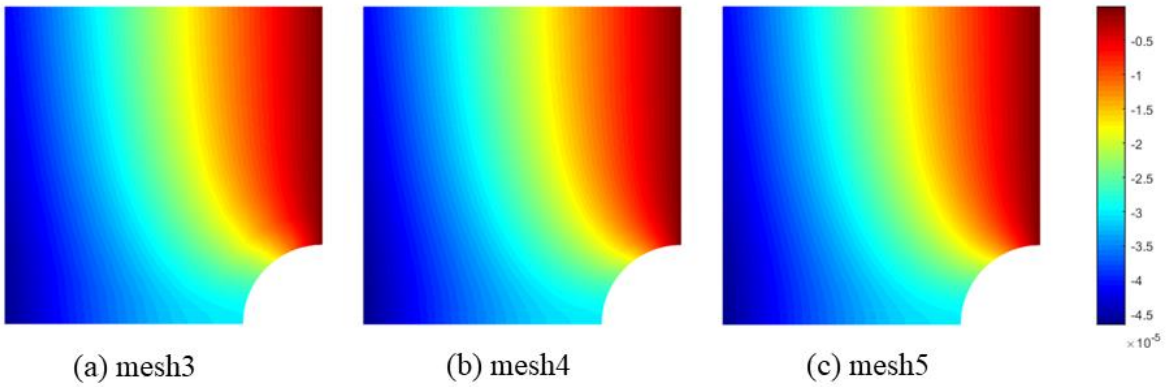

Figure A-3: Contour plots of the displacement in x direction obtained using different meshes

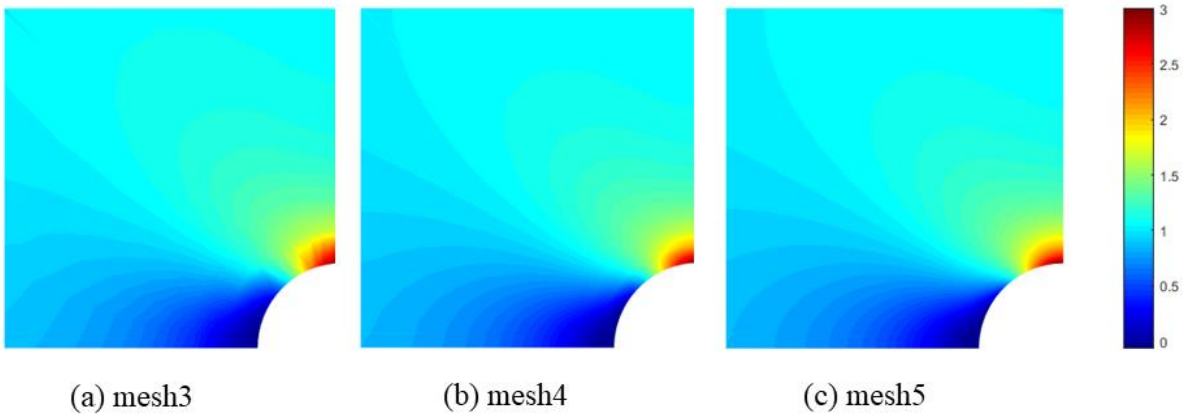

Figure A-4: Contour plots of stress σ_{xx} obtained using different meshes

The convergence study in terms of the energy norm are also plotted in Fig. A-5, where the mesh parameter is approximately computed as the maximum physical distance between two diagonally opposite knots. We observe that optimal convergence is obtained.

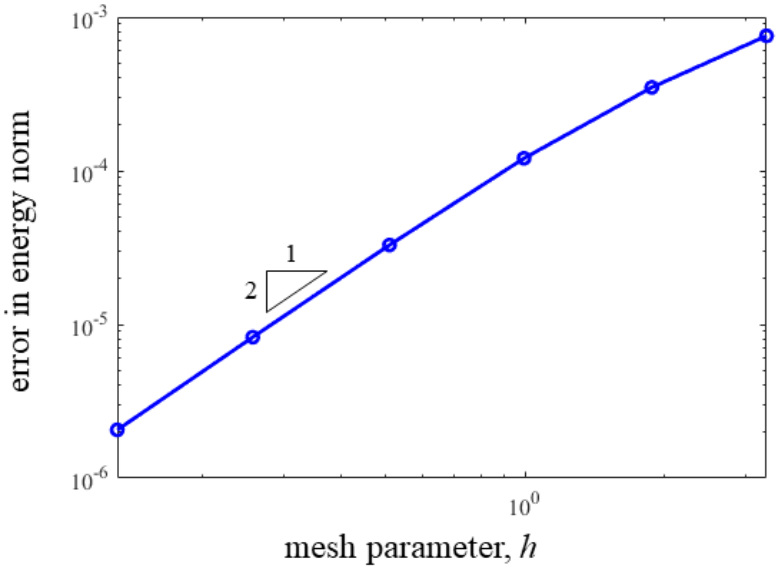

Figure A-5: Convergence of the error in the energy norm of bi-quadratic NURBS discretization

Bibliography

[1] T.J.R. Hughes, J.A. Cottrell, Y. Bazilevs, Isogeometric analysis: CAD, finite elements, NURBS, exact geometry and mesh refinement, Comput. Methods Appl. Mech. Eng. (2005). doi:10.1016/j.cma.2004.10.008.

[2] N. Liu, A.E. Jeffers, Adaptive isogeometric analysis in structural frames using a layer-based discretization to model spread of plasticity, Comput. Struct. (2018). doi:10.1016/j.compstruc.2017.10.016.

[3] N. Liu, A.E. Jeffers, Isogeometric analysis of laminated composite and functionally graded sandwich plates based on a layerwise displacement theory, Compos. Struct. 176 (2017) 143–153. doi:10.1016/j.compstruct.2017.05.037.

[4] N. Liu, A.E. Jeffers, A geometrically exact isogeometric Kirchhoff plate: Feature-preserving automatic meshing and C 1 rational triangular Bézier spline discretizations, Int. J. Numer. Methods Eng. 115 (2018) 395–409. doi:10.1002/nme.5809.

[5] G. Zhang, R. Alberdi, K. Khandelwal, On the locking free isogeometric formulations for 3-D curved Timoshenko beams, Finite Elem. Anal. Des. (2018). doi:10.1016/j.finel.2018.01.007.

[6] R. Alberdi, G. Zhang, K. Khandelwal, A framework for implementation of RVE-based multiscale models in computational homogenization using isogeometric analysis, Int. J. Numer. Methods Eng. 114 (2018) 1018–1051. doi:10.1002/nme.5775.

[7] R. Alberdi, G. Zhang, K. Khandelwal, An isogeometric approach for analysis of phononic crystals and elastic metamaterials with complex geometries, Comput. Mech. (2017). doi:10.1007/s00466-017-1497-x.

[8] G. Zhang, R. Alberdi, K. Khandelwal, Analysis of three-dimensional curved beams using isogeometric approach, Eng. Struct. (2016). doi:10.1016/j.engstruct.2016.03.035.

[9] M.J. Borden, M.A. Scott, J.A. Evans, T.J.R. Hughes, Isogeometric finite element data structures based on Bézier extraction of NURBS, Int. J. Numer. Methods Eng. 87 (2011) 15–47. doi:10.1002/nme.2968.

[10] J.A. Cottrell, T.J.R. Hughes, A. Reali, Studies of refinement and continuity in isogeometric structural analysis, Comput. Methods Appl. Mech. Eng. (2007). doi:10.1016/j.cma.2007.04.007.

[11] J. Kiendl, Y. Bazilevs, M.C. Hsu, R. Wüchner, K.U. Bletzinger, The bending strip method for isogeometric analysis of Kirchhoff-Love shell structures comprised of multiple patches, Comput. Methods Appl. Mech. Eng. (2010). doi:10.1016/j.cma.2010.03.029.

[12] A.-V. Vuong, C. Giannelli, B. Jüttler, B. Simeon, A hierarchical approach to adaptive local refinement in isogeometric analysis, Comput. Methods Appl. Mech. Eng. (2011). doi:10.1016/j.cma.2011.09.004.

[13] Y. Bazilevs, V.M. Calo, J.A. Cottrell, J.A. Evans, T.J.R. Hughes, S. Lipton, M.A. Scott, T.W. Sederberg, Isogeometric analysis using T-splines, Comput. Methods Appl. Mech. Eng. (2010). doi:10.1016/j.cma.2009.02.036.

[14] K.A. Johannessen, T. Kvamsdal, T. Dokken, Isogeometric analysis using LR B-splines,

Comput. Methods Appl. Mech. Eng. (2014). doi:10.1016/j.cma.2013.09.014.
[15] J. Deng, F. Chen, X. Li, C. Hu, W. Tong, Z. Yang, Y. Feng, Polynomial splines over hierarchical T-meshes, Graph. Models. (2008). doi:10.1016/j.gmod.2008.03.001.
[16] M.A. Scott, X. Li, T.W. Sederberg, T.J.R. Hughes, Local refinement of analysis-suitable T-splines, Comput. Methods Appl. Mech. Eng. (2012). doi:10.1016/j.cma.2011.11.022.
[17] X. Wei, Y.J. Zhang, T.J.R. Hughes, M.A. Scott, Extended Truncated Hierarchical Catmull-Clark Subdivision, Comput. Methods Appl. Mech. Eng. (2016). doi:10.1016/j.cma.2015.10.024.
[18] P. Hennig, S. Müller, M. Kästner, Bézier extraction and adaptive refinement of truncated hierarchical NURBS, Comput. Methods Appl. Mech. Eng. (2016). doi:10.1016/j.cma.2016.03.009.
[19] T. Kanduč, C. Giannelli, F. Pelosi, H. Speleers, Adaptive isogeometric analysis with hierarchical box splines, Comput. Methods Appl. Mech. Eng. (2017). doi:10.1016/j.cma.2016.09.046.
[20] H. Speleers, C. Manni, F. Pelosi, M.L. Sampoli, Isogeometric analysis with Powell-Sabin splines for advection-diffusion-reaction problems, Comput. Methods Appl. Mech. Eng. (2012). doi:10.1016/j.cma.2012.02.009.
[21] L. Engvall, J.A. Evans, Isogeometric triangular Bernstein-Bézier discretizations: Automatic mesh generation and geometrically exact finite element analysis, Comput. Methods Appl. Mech. Eng. (2016). doi:10.1016/j.cma.2016.02.012.
[22] Q. Pan, G. Xu, G. Xu, Y. Zhang, Isogeometric analysis based on extended Loop's subdivision, J. Comput. Phys. (2015). doi:10.1016/j.jcp.2015.06.044.
[23] T. Elguedj, Y. Bazilevs, V.M. Calo, T.J.R. Hughes, over(B, -) and over(F, -) projection methods for nearly incompressible linear and non-linear elasticity and plasticity using higher-order NURBS elements, Comput. Methods Appl. Mech. Eng. (2008). doi:10.1016/j.cma.2008.01.012.
[24] G. Zhang, K. Khandelwal, Modeling of nonlocal damage-plasticity in beams using isogeometric analysis, Comput. Struct. (2016). doi:10.1016/j.compstruc.2015.12.006.
[25] C.H. Thai, H. Nguyen-Xuan, N. Nguyen-Thanh, T.H. Le, T. Nguyen-Thoi, T. Rabczuk, Static, free vibration, and buckling analysis of laminated composite Reissner-Mindlin plates using NURBS-based isogeometric approach, Int. J. Numer. Methods Eng. (2012). doi:10.1002/nme.4282.
[26] C.H. Thai, A.J.M. Ferreira, E. Carrera, H. Nguyen-Xuan, Isogeometric analysis of laminated composite and sandwich plates using a layerwise deformation theory, Compos. Struct. (2013). doi:10.1016/j.compstruct.2013.04.002.
[27] Y. Guo, A.P. Nagy, Z. Gürdal, A layerwise theory for laminated composites in the framework of isogeometric analysis, Compos. Struct. (2014). doi:10.1016/j.compstruct.2013.08.016.
[28] L. V. Tran, A.J.M. Ferreira, H. Nguyen-Xuan, Isogeometric analysis of functionally graded plates using higher-order shear deformation theory, Compos. Part B Eng. (2013). doi:10.1016/j.compositesb.2013.02.045.
[29] S.A. Farzam-Rad, B. Hassani, A. Karamodin, Isogeometric analysis of functionally graded plates using a new quasi-3D shear deformation theory based on physical neutral surface, Compos. Part B Eng. (2017). doi:10.1016/j.compositesb.2016.09.029.
[30] N. Liu, P. Plucinsky, A.E. Jeffers, Combining Load-Controlled and Displacement-Controlled Algorithms to Model Thermal-Mechanical Snap-Through Instabilities in

Structures, J. Eng. Mech. (2017). doi:10.1061/(ASCE)EM.1943-7889.0001263.
[31] J. Coleman, E. Spacone, Localization Issues in Force-Based Frame Elements, J. Struct. Eng. (2001). doi:10.1061/(ASCE)0733-9445(2001)127:11(1257).
[32] M.A. Crisfield, A consistent co-rotational formulation for non-linear, three-dimensional, beam-elements, Comput. Methods Appl. Mech. Eng. (1990). doi:10.1016/0045-7825(90)90106-V.
[33] E. Spacone, V. Ciampi, F.C. Filippout, Mixed Formulation Of Nonlinear Finite Element, Comput. Struct. (1996). doi:10.1016/0045-7949(95)00103-N.
[34] M. Petrangeli, V. Ciamp, Equilibrium based iterative solutions for the non-linear beam problem, Int. J. Numer. Methods Eng. (1997). doi:10.1002/(SICI)1097-0207(19970215)40:3<423::AID-NME72>3.0.CO;2-H.
[35] A. Neuenhofer, F.C. Filippou, Evaluation of Nonlinear Frame Finite-Element Models, J. Struct. Eng. (1997). doi:10.1061/(ASCE)0733-9445(1997)123:7(958).
[36] P.K.V. V Nukala, D.W. White, A mixed finite element for three-dimensional nonlinear analysis of steel frames, Comput. Methods Appl. Mech. Eng. (2004). doi:10.1016/j.cma.2004.01.029.
[37] D. Addessi, V. Ciampi, A regularized force-based beam element with a damage-plastic section constitutive law, Int. J. Numer. Methods Eng. (2007). doi:10.1002/nme.1911.
[38] B.N. Alemdar, D.W. White, Displacement, Flexibility, and Mixed Beam–Column Finite Element Formulations for Distributed Plasticity Analysis, J. Struct. Eng. (2005). doi:10.1061/(ASCE)0733-9445(2005)131:12(1811).
[39] L. Beirão da Veiga, A. Buffa, J. Rivas, G. Sangalli, Some estimates for h-p-k-refinement in Isogeometric Analysis, Numer. Math. (2011). doi:10.1007/s00211-010-0338-z.
[40] J.A. Cottrell, A. Reali, Y. Bazilevs, T.J.R. Hughes, Isogeometric analysis of structural vibrations, Comput. Methods Appl. Mech. Eng. (2006). doi:10.1016/j.cma.2005.09.027.
[41] A.P. Nagy, M.M. Abdalla, Z. Gürdal, Isogeometric sizing and shape optimisation of beam structures, Comput. Methods Appl. Mech. Eng. (2010). doi:10.1016/j.cma.2009.12.010.
[42] L. Beirão da Veiga, C. Lovadina, A. Reali, Avoiding shear locking for the Timoshenko beam problem via isogeometric collocation methods, Comput. Methods Appl. Mech. Eng. (2012). doi:10.1016/j.cma.2012.05.020.
[43] F. Auricchio, L. Beirão da Veiga, J. Kiendl, C. Lovadina, A. Reali, Locking-free isogeometric collocation methods for spatial Timoshenko rods, Comput. Methods Appl. Mech. Eng. (2013). doi:10.1016/j.cma.2013.03.009.
[44] R. Bouclier, T. Elguedj, A. Combescure, Locking free isogeometric formulations of curved thick beams, Comput. Methods Appl. Mech. Eng. (2012). doi:10.1016/j.cma.2012.06.008.
[45] L. Greco, M. Cuomo, B-Spline interpolation of Kirchhoff-Love space rods, Comput. Methods Appl. Mech. Eng. (2013). doi:10.1016/j.cma.2012.11.017.
[46] A. Cazzani, M. Malagù, E. Turco, Isogeometric analysis of plane-curved beams, Math. Mech. Solids. (2014). doi:10.1177/1081286514531265.
[47] A. Reali, H. Gomez, An isogeometric collocation approach for Bernoulli-Euler beams and Kirchhoff plates, Comput. Methods Appl. Mech. Eng. 284 (2015) 623–636. doi:10.1016/j.cma.2014.10.027.
[48] L. Greco, M. Cuomo, An implicitG1multi patch B-spline interpolation for Kirchhoff-Love space rod, Comput. Methods Appl. Mech. Eng. (2014). doi:10.1016/j.cma.2013.09.018.
[49] J. Kiendl, F. Auricchio, T.J.R. Hughes, A. Reali, Single-variable formulations and

isogeometric discretizations for shear deformable beams, Comput. Methods Appl. Mech. Eng. (2015). doi:10.1016/j.cma.2014.11.011.
[50] T. Elguedj, T.J.R. Hughes, Isogeometric analysis of nearly incompressible large strain plasticity, Comput. Methods Appl. Mech. Eng. (2014). doi:10.1016/j.cma.2013.09.024.
[51] J.F. Caseiro, R.A.F. Valente, A. Reali, J. Kiendl, F. Auricchio, R.J. Alves de Sousa, Assumed natural strain NURBS-based solid-shell element for the analysis of large deformation elasto-plastic thin-shell structures, Comput. Methods Appl. Mech. Eng. (2015). doi:10.1016/j.cma.2014.10.037.
[52] D.J. Benson, Y. Bazilevs, M.C. Hsu, T.J. Hughes, A large deformation, rotation-free, isogeometric shell, Comput. Methods Appl. Mech. Eng. (2011). doi:10.1016/j.cma.2010.12.003.
[53] R. Bouclier, T. Elguedj, A. Combescure, Development of a mixed displacement-stress formulation for the analysis of elastoplastic structures under small strains: Application to a locking-free, NURBS-based solid-shell element, Comput. Methods Appl. Mech. Eng. (2015). doi:10.1016/j.cma.2015.07.012.
[54] W. McGuire, R. Gallagher, R. Ziemian, Matrix Structural Analysis, 2nd Edition, Fac. Books. (2000).
[55] M. Kojic, K.-J. Bathe, Inelastic analysis of solids and structures, Springer Science & Business Media, 2006.
[56] J.N. Reddy, Mechanics of laminated composite plates and shells: theory and analysis, 2003. doi:10.1007/978-1-4471-0095-9.
[57] M.B. Bever, P.E. Duwez, Gradients in composite materials, Mater. Sci. Eng. (1972). doi:10.1016/0025-5416(72)90059-6.
[58] M. Eisenberger, H. Abramovich, O. Shulepov, Dynamic stiffness analysis of laminated beams using a first order shear deformation theory, Compos. Struct. 31 (1995) 265–271. doi:10.1016/0263-8223(95)00091-7.
[59] P. Zhu, Z.X. Lei, K.M. Liew, Static and free vibration analyses of carbon nanotube-reinforced composite plates using finite element method with first order shear deformation plate theory, Compos. Struct. (2012). doi:10.1016/j.compstruct.2011.11.010.
[60] T.K. Nguyen, K. Sab, G. Bonnet, First-order shear deformation plate models for functionally graded materials, Compos. Struct. (2008). doi:10.1016/j.compstruct.2007.03.004.
[61] A.J.M. Ferreira, C.M.C. Roque, P.A.L.S. Martins, Analysis of composite plates using higher-order shear deformation theory and a finite point formulation based on the multiquadric radial basis function method, Compos. Part B Eng. (2003). doi:10.1016/S1359-8368(03)00083-0.
[62] J.N. Reddy, C.F. Liu, A higher-order shear deformation theory of laminated elastic shells, Int. J. Eng. Sci. (1985). doi:10.1016/0020-7225(85)90051-5.
[63] J.L. Mantari, A.S. Oktem, C. Guedes Soares, Static and dynamic analysis of laminated composite and sandwich plates and shells by using a new higher-order shear deformation theory, Compos. Struct. (2011). doi:10.1016/j.compstruct.2011.07.020.
[64] J.N. Reddy, An evaluation of equivalent-single-layer and layerwise theories of composite laminates, Compos. Struct. (1993). doi:10.1016/0263-8223(93)90147-I.
[65] M. Braun, M. Bischoff, E. Ramm, Nonlinear shell formulations for complete three-dimensional constitutive laws including composites and laminates, Comput. Mech. (1994). doi:10.1007/BF00350285.

[66] E. Carrera, Theories and finite elements for multilayered, anisotropic, composite plates and shells, Arch. Comput. Methods Eng. (2002). doi:10.1007/BF02736649.
[67] J.N. Reddy, J. Kim, A nonlinear modified couple stress-based third-order theory of functionally graded plates, Compos. Struct. (2012). doi:10.1016/j.compstruct.2011.10.006.
[68] L.W. Zhang, P. Zhu, K.M. Liew, Thermal buckling of functionally graded plates using a local Kriging meshless method, Compos. Struct. (2014). doi:10.1016/j.compstruct.2013.09.043.
[69] P. Zhu, L.W. Zhang, K.M. Liew, Geometrically nonlinear thermomechanical analysis of moderately thick functionally graded plates using a local Petrov-Galerkin approach with moving Kriging interpolation, Compos. Struct. (2014). doi:10.1016/j.compstruct.2013.08.001.
[70] A.M.A. Neves, A.J.M. Ferreira, E. Carrera, M. Cinefra, C.M.C. Roque, R.M.N. Jorge, C.M.M. Soares, A quasi-3D hyperbolic shear deformation theory for the static and free vibration analysis of functionally graded plates, Compos. Struct. (2012). doi:10.1016/j.compstruct.2011.12.005.
[71] L.W. Zhang, Z.X. Lei, K.M. Liew, Free vibration analysis of functionally graded carbon nanotube-reinforced composite triangular plates using the FSDT and element-free IMLS-Ritz method, Compos. Struct. (2015). doi:10.1016/j.compstruct.2014.10.009.
[72] D.K. Jha, T. Kant, R.K. Singh, A critical review of recent research on functionally graded plates, Compos. Struct. (2013). doi:10.1016/j.compstruct.2012.09.001.
[73] A.M. Zenkour, Generalized shear deformation theory for bending analysis of functionally graded plates, Appl. Math. Model. (2006). doi:10.1016/j.apm.2005.03.009.
[74] A.M.A. Neves, A.J.M. Ferreira, E. Carrera, M. Cinefra, C.M.C. Roque, R.M.N. Jorge, C.M.M. Soares, Static, free vibration and buckling analysis of isotropic and sandwich functionally graded plates using a quasi-3D higher-order shear deformation theory and a meshless technique, Compos. Part B Eng. (2013). doi:10.1016/j.compositesb.2012.01.089.
[75] E. Carrera, S. Brischetto, M. Cinefra, M. Soave, Effects of thickness stretching in functionally graded plates and shells, Compos. Part B Eng. (2011). doi:10.1016/j.compositesb.2010.10.005.
[76] Y. Guo, M. Ruess, Z. Gürdal, A contact extended isogeometric layerwise approach for the buckling analysis of delaminated composites, Compos. Struct. (2014). doi:10.1016/j.compstruct.2014.05.006.
[77] H. Nguyen-Xuan, L. V. Tran, C.H. Thai, S. Kulasegaram, S.P.A. Bordas, Isogeometric analysis of functionally graded plates using a refined plate theory, Compos. Part B Eng. (2014). doi:10.1016/j.compositesb.2014.04.001.
[78] L. V. Tran, C.H. Thai, H. Nguyen-Xuan, An isogeometric finite element formulation for thermal buckling analysis of functionally graded plates, Finite Elem. Anal. Des. (2013). doi:10.1016/j.finel.2013.05.003.
[79] S. Yin, J.S. Hale, T. Yu, T.Q. Bui, S.P.A. Bordas, Isogeometric locking-free plate element: A simple first order shear deformation theory for functionally graded plates, Compos. Struct. (2014). doi:10.1016/j.compstruct.2014.07.028.
[80] N. Valizadeh, S. Natarajan, O.A. Gonzalez-Estrada, T. Rabczuk, T.Q. Bui, S.P.A. Bordas, NURBS-based finite element analysis of functionally graded plates: Static bending, vibration, buckling and flutter, Compos. Struct. (2013). doi:10.1016/j.compstruct.2012.11.008.
[81] T. Yu, T.Q. Bui, S. Yin, D.H. Doan, C.T. Wu, T. Van Do, S. Tanaka, On the thermal

buckling analysis of functionally graded plates with internal defects using extended isogeometric analysis, Compos. Struct. (2016). doi:10.1016/j.compstruct.2015.11.002.
[82] C.H. Thai, A.M. Zenkour, M. Abdel Wahab, H. Nguyen-Xuan, A simple four-unknown shear and normal deformations theory for functionally graded isotropic and sandwich plates based on isogeometric analysis, Compos. Struct. (2016). doi:10.1016/j.compstruct.2015.11.066.
[83] N.J. Pagano, Exact Solutions for Rectangular Bidirectional Composites and Sandwich Plates, J. Compos. Mater. (1970). doi:10.1177/002199837000400102.
[84] D.H. Robbins, J.N. Reddy, Modelling of thick composites using a layerwise laminate theory, Int. J. Numer. Methods Eng. (1993). doi:10.1002/nme.1620360407.
[85] A.J.M. Ferreira, G.E. Fasshauer, R.C. Batra, J.D. Rodrigues, Static deformations and vibration analysis of composite and sandwich plates using a layerwise theory and RBF-PS discretizations with optimal shape parameter, Compos. Struct. (2008). doi:10.1016/j.compstruct.2008.07.025.
[86] L.M.S. Castro, A.J.M. Ferreira, S. Bertoluzza, R.C. Batra, J.N. Reddy, A wavelet collocation method for the static analysis of sandwich plates using a layerwise theory, Compos. Struct. (2010). doi:10.1016/j.compstruct.2010.01.021.
[87] S. Srinivas, A refined analysis of composite laminates, J. Sound Vib. (1973). doi:10.1016/S0022-460X(73)80170-1.
[88] B.N. Pandya, T. Kant, Higher-order shear deformable theories for flexure of sandwich plates-Finite element evaluations, Int. J. Solids Struct. (1988). doi:10.1016/0020-7683(88)90090-X.
[89] N. Grover, D.K. Maiti, B.N. Singh, A new inverse hyperbolic shear deformation theory for static and buckling analysis of laminated composite and sandwich plates, Compos. Struct. (2013). doi:10.1016/j.compstruct.2012.08.012.
[90] J.L. Mantari, A.S. Oktem, C. Guedes Soares, A new trigonometric shear deformation theory for isotropic, laminated composite and sandwich plates, Int. J. Solids Struct. (2012). doi:10.1016/j.ijsolstr.2011.09.008.
[91] A.J.M. Ferreira, Analysis of composite plates using a layerwise theory and multiquadrics discretization, Mech. Adv. Mater. Struct. (2005). doi:10.1080/15376490490493952.
[92] A.M.A. Neves, A.J.M. Ferreira, E. Carrera, C.M.C. Roque, M. Cinefra, R.M.N. Jorge, C.M.M. Soares, A quasi-3D sinusoidal shear deformation theory for the static and free vibration analysis of functionally graded plates, Compos. Part B Eng. (2012). doi:10.1016/j.compositesb.2011.08.009.
[93] S. Brischetto, Classical and mixed advanced models for sandwich plates embedding functionally graded cores, J. Mech. Mater. Struct. (2009). doi:10.2140/jomms.2009.4.13.
[94] S. Shojaee, E. Izadpanah, N. Valizadeh, J. Kiendl, Free vibration analysis of thin plates by using a NURBS-based isogeometric approach, Finite Elem. Anal. Des. 61 (2012) 23–34. doi:10.1016/j.finel.2012.06.005.
[95] C.H. Thai, H. Nguyen-Xuan, N. Nguyen-Thanh, T.-H. Le, T. Nguyen-Thoi, T. Rabczuk, Static, free vibration, and buckling analysis of laminated composite Reissner-Mindlin plates using NURBS-based isogeometric approach, Int. J. Numer. Methods Eng. 91 (2012) 571–603. doi:10.1002/nme.4282.
[96] L. Beirão Da Veiga, T.J.R. Hughes, J. Kiendl, C. Lovadina, J. Niiranen, a. Reali, H. Speleers, A locking-free model for Reissner–Mindlin plates: Analysis and isogeometric implementation via NURBS and triangular NURPS, Math. Model. Methods Appl. Sci. 25

(2015) 1519–1551. doi:10.1142/S0218202515500402.
[97] N. Fantuzzi, F. Tornabene, Strong Formulation Isogeometric Analysis (SFIGA) for laminated composite arbitrarily shaped plates, Compos. Part B Eng. 96 (2016) 173–203. doi:10.1016/j.compositesb.2016.04.034.
[98] F. Tornabene, N. Fantuzzi, M. Bacciocchi, A new doubly-curved shell element for the free vibrations of arbitrarily shaped laminated structures based on Weak Formulation IsoGeometric Analysis, Compos. Struct. 171 (2017) 429–461. doi:10.1016/j.compstruct.2017.03.055.
[99] D. Schillinger, E. Rank, An unfitted hp-adaptive finite element method based on hierarchical B-splines for interface problems of complex geometry, Comput. Methods Appl. Mech. Eng. 200 (2011) 3358–3380. doi:10.1016/j.cma.2011.08.002.
[100] C. Giannelli, B. Jüttler, H. Speleers, THB-splines: The truncated basis for hierarchical splines, Comput. Aided Geom. Des. 29 (2012) 485–498. doi:10.1016/j.cagd.2012.03.025.
[101] T. Dokken, T. Lyche, K.F. Pettersen, Polynomial splines over locally refined box-partitions, Comput. Aided Geom. Des. 30 (2013) 331–356. doi:10.1016/j.cagd.2012.12.005.
[102] H. Speleers, A normalized basis for quintic Powell-Sabin splines, Comput. Aided Geom. Des. 27 (2010) 438–457. doi:10.1016/j.cagd.2010.05.001.
[103] H. Speleers, P. Dierckx, S. Vandewalle, Numerical solution of partial differential equations with Powell-Sabin splines, J. Comput. Appl. Math. 189 (2006) 643–659. doi:10.1016/j.cam.2005.03.001.
[104] H. Speleers, A normalized basis for reduced Clough-Tocher splines, Comput. Aided Geom. Des. 27 (2010) 700–712. doi:10.1016/j.cagd.2010.09.003.
[105] H. Speleers, Construction of Normalized B-Splines for a Family of Smooth Spline Spaces Over Powell-Sabin Triangulations, Constr. Approx. 37 (2013) 41–72. doi:10.1007/s00365-011-9151-x.
[106] J. Grošelj, A normalized representation of super splines of arbitrary degree on Powell–Sabin triangulations, BIT Numer. Math. 56 (2016) 1257–1280. doi:10.1007/s10543-015-0600-y.
[107] N. Jaxon, X. Qian, Isogeometric analysis on triangulations, CAD Comput. Aided Des. 46 (2014) 45–47. doi:10.1016/j.cad.2013.08.017.
[108] H. Speleers, C. Manni, F. Pelosi, From NURBS to NURPS geometries, Comput. Methods Appl. Mech. Eng. 255 (2013) 238–254. doi:10.1016/j.cma.2012.11.012.
[109] S. May, J. Vignollet, R. de Borst, Powell-Sabin B-splines and unstructured standard T-splines for the solution of the Kirchhoff-Love plate theory exploiting Bézier extraction, Int. J. Numer. Methods Eng. 107 (2016) 205–233. doi:10.1002/nme.5163.
[110] S. May, R. de Borst, J. Vignollet, Powell-Sabin B-splines for smeared and discrete approaches to fracture in quasi-brittle materials, Comput. Methods Appl. Mech. Eng. 307 (2016) 193–214. doi:10.1016/j.cma.2016.04.023.
[111] L.L. Lai, Ming-Jun; Schumaker, Spline Functions on Triangulations, Cambridge University Press, 2007.
[112] D. Engwirda, Mesh2d-automatic mesh generation, Http://Www.Mathworks.Com/Matlabcentral/Fileexchange/25555-Mesh2d-Automatic-Mesh-Generation. (2009).
[113] G. Farin, Curves and Surfaces for CAGD: A Practical Guide, 2002. doi:10.1016/B978-1-55860-737-8.50030-2.

[114] M.J. Borden, M.A. Scott, J.A. Evans, T.J.R. Hughes, Isogeometric finite element data structures based on Bézier extraction of NURBS, Int. J. Numer. Methods Eng. 87 (2011) 15–47. doi:10.1002/nme.2968.
[115] M.J. Lai, P. Wenston, Bivariate splines for fluid flows, Comput. Fluids. 33 (2004) 1047–1073. doi:10.1016/j.compfluid.2003.10.003.
[116] P. Lidström, P. Olsson, On the natural vibrations of linear structures with constraints, J. Sound Vib. 301 (2007) 341–354. doi:10.1016/j.jsv.2006.10.003.
[117] Y. Rostamiyan, A. Fereidoon, M. Davoudabadi, H. Yaghoobi, D.D. Ganji, Analytical Approach to Investigation of Deflection of Circular Plate Under Uniform Load by Homotopy Perturbation Method, Math. Comput. Appl. 15 (2010) 816–821. doi:10.3390/mca15050816.
[118] T.Q. Bui, M.N. Nguyen, A moving Kriging interpolation-based meshfree method for free vibration analysis of Kirchhoff plates, Comput. Struct. 89 (2011) 380–394. doi:10.1016/j.compstruc.2010.11.006.
[119] X.Y. Cui, G.R. Liu, G.Y. Li, G.Y. Zhang, A thin plate formulation without rotation DOFs based on the radial point interpolation method and triangular cells, Int. J. Numer. Methods Eng. 85 (2011) 958–986. doi:10.1002/nme.3000.
[120] J. Lemaitre, J.-L. Chaboche, Mechanics of solid materials, Cambridge University Press, Cambridge, 1990. doi:10.1017/CBO9781139167970.
[121] W.A.M. Brekelmans, J.H.P. de Vree, Reduction of mesh sensitivity in continuum damage mechanics, Acta Mech. 110 (1995) 49–56. doi:10.1007/BF01215415.
[122] Z.P. Bažant, B.H. Oh, Crack band theory for fracture of concrete, Matériaux Constr. 16 (1983) 155–177. doi:10.1007/BF02486267.
[123] G. Pijaudier-Cabot, Z.P. Bažant, Nonlocal Damage Theory, J. Eng. Mech. 113 (1988) 1512–1533. doi:10.1061/(ASCE)0733-9399(1987)113:10(1512).
[124] L. Li, G. Zhang, K. Khandelwal, Failure resistant topology optimization of structures using nonlocal elastoplastic-damage model, Struct. Multidiscip. Optim. (2018). doi:10.1007/s00158-018-1984-5.
[125] R.H.J. Peerlings, R. de Borst, W.A.M. Brekelmans, M.G.D. Geers, Gradient-enhanced damage modelling of concrete fracture, Mech. Cohesive-Frictional Mater. 3 (1998) 323–342. doi:10.1002/(SICI)1099-1484(1998100)3:4<323::AID-CFM51>3.0.CO;2-Z.
[126] C. V. Verhoosel, M.A. Scott, T.J.R. Hughes, R. de Borst, An isogeometric analysis approach to gradient damage models, Int. J. Numer. Methods Eng. 86 (2011) 115–134. doi:10.1002/nme.3150.
[127] H. Askes, J. Pamin, R. De Borst, Dispersion analysis and element-free Galerkin solutions of second- and fourth-order gradient-enhanced damage models, Int. J. Numer. Methods Eng. 49 (2000) 811–832. doi:10.1002/1097-0207(20001030)49:6<811::AID-NME985>3.0.CO;2-9.
[128] R.J. Dorgan, G.Z. Voyiadjis, A mixed finite element implementation of a gradient-enhanced coupled damage-plasticity model, Int. J. Damage Mech. 15 (2006) 201–235. doi:10.1177/1056789506060740.
[129] R.D.E. Borst, J. Pamin, Some Novel Developments in Finite Element Procedures for Gradient-Dependent Plasticity, Int. J. 39 (1996) 2477–2505. doi:10.1002/(SICI)1097-0207(19960730)39:14<2477::AID-NME962>3.0.CO;2-E.
[130] H. Askes, L.J. Sluys, Explicit and implicit gradient series in damage mechanics, Eur. J. Mech. A/Solids. 21 (2002) 379–390. doi:10.1016/S0997-7538(02)01214-7.

[131] X. Wei, Y. Zhang, L. Liu, T.J.R. Hughes, Truncated T-splines: Fundamentals and methods, Comput. Methods Appl. Mech. Eng. (2017). doi:10.1016/j.cma.2016.07.020.
[132] L. Liu, Y.J. Zhang, X. Wei, Weighted T-splines with application in reparameterizing trimmed NURBS surfaces, Comput. Methods Appl. Mech. Eng. (2015). doi:10.1016/j.cma.2015.06.020.
[133] M.A. Scott, M.J. Borden, C. V. Verhoosel, T.W. Sederberg, T.J.R. Hughes, Isogeometric finite element data structures based on Bézier extraction of T-splines, Int. J. Numer. Methods Eng. 88 (2011) 126–156. doi:10.1002/nme.3167.
[134] T.Q. Thai, T. Rabczuk, Y. Bazilevs, G. Meschke, A higher-order stress-based gradient-enhanced damage model based on isogeometric analysis, Comput. Methods Appl. Mech. Eng. 304 (2016) 584–604. doi:10.1016/j.cma.2016.02.031.
[135] K. Karčiauskas, T. Nguyen, J. Peters, Generalizing bicubic splines for modeling and IGA with irregular layout, CAD Comput. Aided Des. 70 (2016) 23–35. doi:10.1016/j.cad.2015.07.014.
[136] M.C. Rivara, Algorithms for refining triangular grids suitable for adaptive and multigrid techniques, Int. J. Numer. Methods Eng. 20 (1984) 745–756. doi:10.1002/nme.1620200412.
[137] C. V. Verhoose, J.J.C. Remmers, M.A. Gutiérrez, A dissipation-based arc-length method for robust simulation of brittle and ductile failure, Int. J. Numer. Methods Eng. 77 (2009) 1290–1321. doi:10.1002/nme.2447.
[138] C. V. Verhoosel, M.A. Scott, M.J. Borden, T.J.R. Hughes, R. de Borst, Discretization of Higher Order Gradient Damage Models Using Isogeometric Finite Elements, in: Damage Mech. Cem. Mater. Struct., 2013: pp. 89–120. doi:10.1002/9781118562086.ch4.
[139] N. Liu, A.E. Jeffers, Rational Bézier Triangles for the Analysis of Isogeometric Higher-Order Gradient Damage Models, in: 13th World Congress on Computational Mechanics (WCCM XIII) and 2nd Pan American Congress on Computational Mechanics (PANACM II), New York City, NY, USA, July 22-27, 2018.